Non-Markovian effects in open quantum systems

Inaugural-Dissertation

zur Erlangung des Doktorgrades
der Mathematisch-Naturwissenschaftlichen Fakultät
der Heinrich-Heine-Universität Düsseldorf

vorgelegt von

Jens Eckel

aus Bonn Bad-Godesberg

Düsseldorf, Juli 2009

Aus dem Institut für Theoretische Physik IV
der Heinrich-Heine-Universität Düsseldorf

Gedruckt mit Genehmigung der
Mathematisch-Naturwissenschaftlichen Fakultät
der Heinrich-Heine-Universität Düsseldorf

Referent: PD Dr. Michael Thorwart
Koreferent: Prof. Dr. Reinhold Egger

Tag der mündlichen Prüfung: 3.7.2009

Summary

In the thesis at hand we investigate the dynamics of open quantum systems. Within the present studies the environment of the systems of interest is both bosonic or fermionic in nature. The aim of this work is to account for non-Markovian effects within the real-time dynamics and to demonstrate their relevance for a thorough understanding of the underlying dynamical processes.

After an introductory chapter which motivates the studies presented in the thesis we first give an introduction on the dynamics of open quantum systems in chapter 2. Here, the underlying formalism essential for the thesis is presented and we elucidate further the similarities of the specific chapters of this work.

In chapter 3 we investigate the real-time dynamics of a donor based charge qubit. Here, the charge qubit is coupled to a bosonic environment of phonons which constitutes a specific spectral density. We improve the numerically exact QUAPI method introduced in detail here at one important step. This well established method allows for including all non-Markovian effects and is also the method we use in chapter 4 and 5. Our results indicate that phonons are not the main source for dissipation and decoherence within the donor based charge qubit, but represent an upper limit for decoherence.

Chapter 4 is concerned with an externally driven two-level system coupled to an Ohmic environment. This is a realistic model for light-harvesting biomolecules and we concentrate on the influence of the cut-off frequency of the environment. For these biomolecular systems this frequency is of the order of characteristic system energies which renders the dissipative dynamics highly non-Markovian. We identify a resonant behavior of the amplitude of the forced oscillations in the long-time limit. It turns out that a non-Markovian environment plays a constructive role in protecting the coherent quantum dynamics over a certain period of time.

In chapter 5 we extend the model on two Förster coupled biomolecules coupled to a common Ohmic environment. Since this constitutes a bipartite system we investigate the underlying dissipative dynamics of entanglement. We show that an initially entangled state of the two biomolecules is more robust when subjected to a slow environment. Moreover it turns out that a non-Markovian environment plays a constructive role in generating entanglement in these biomolecular structures, which holds up to temperatures well beyond the excitonic gap.

Within chapter 6 we have analyzed the nonequilibrium transport properties of an Anderson quantum dot attached to metallic, i.e., fermionic, leads. Here, we present the newly developed ISPI scheme, a novel numerical scheme in order to compute the underlying real-time fermionic path integral in an ab-initio deterministic way. Similar to the QUAPI method the ISPI scheme is rooted upon the fact that time non-local correlation functions can be truncated after a certain memory time and thus non-Markovian features are fully taken into account. To check the validity of our novel scheme we compare our results with known results in different parameter regimes and find good agreement with the outcome of approximative approaches.

Zusammenfassung

In der vorliegenden Arbeit beschäftigen wir uns mit der dissipativen Dynamik offener Quantensysteme. Hierbei ist die Umgebung der im Rahmen dieser Arbeit untersuchten Systeme bosonischer oder fermionischer Natur. Das Hauptziel der vorliegenden Untersuchungen besteht darin nicht-Markovsche Effekte innerhalb der Realzeitdynamik voll zu berücksichtigen und deren Relevanz für ein tieferes Verständnis der zugrundeliegenden dynamischen Prozesse zu verdeutlichen.

Nach einem einleitenden Kapitel, welches die einzelnen Untersuchungen der Arbeit motiviert, geben wir in Kapitel 2 zunächst eine Einführung in die Dynamik offener Quantensysteme, wobei dort der für diese Arbeit essentielle Formalismus sowie die Gemeinsamkeiten der einzelnen Kapitel verdeutlicht werden.

In Kapitel 3 untersuchen wir die Realzeitdynamik eines Donor basierten Ladungsquantenbits, welches in eine aus Phononen bestehende bosonische Umgebung eingebettet ist, die eine spezifische Spektraldichte aufweist. Um nicht-Markovsche Effekte zu berücksichtigen, führen wir die etablierte QUAPI Methode ein, die in einem entscheidenden Schritt optimiert worden ist und auch in den Kapiteln 4 und 5 genutzt wird. Unsere Ergebnisse zeigen, daß Phononen nicht als Hauptursache für Dekohärenz eines Donor basierten Ladungsquantenbits angesehen werden können; gleichwohl repräsentieren sie ein oberes Limit für Dekohärenz, welches nicht überschritten werden kann.

Kapitel 4 thematisiert ein getriebenes zwei-Niveau System, welches an ein Ohmsches Bad koppelt. Dieses Modell ist realistisch für lichteinfangende Biomoleküle und wir konzentrieren uns auf den Einfluß der Grenzfrequenz der Umgebung. Innerhalb solcher biomolekularer Strukturen ist die Grenzfrequenz in der gleichen Größenordnung wie relevante Systemenergien, was zu einer hochgradig nicht-Markovschen dissipativen Dynamik führt. Wir identifizieren ein resonantes Verhalten der Amplitude der getriebenen Oszillationen im Langzeitlimit und es stellt sich heraus, daß eine nicht-Markovsche Umgebung eine konstruktive Rolle im Erhalt quantenkohärenter Dynamik spielt.

In Kapitel 5 wird dieses Modell auf zwei Förster-gekoppelte Biomoleküle erweitert, die an ein gemeinsames Ohmsches Bad koppeln. Dies ist ein zweiteiliges System und wir untersuchen die zugrundeliegende dissipative Verschränkungsdynamik. Es wird gezeigt, daß ein anfangs verschränkter Zustand der beiden Biomoleküle stabiler ist, wenn er unter dem Einfluß einer langsamen Umgebung ist. Darüberhinaus stellt sich heraus, daß eine nicht-Markovsche Umgebung einen konstruktiven Einfluß auf die Erzeugung von Verschränkung innerhalb biomolekularer Strukturen hat, bis hin zu Temperaturen weit oberhalb der exzitonischen Lücke.

Innerhalb des Kapitel 6 untersuchen wir den Nichtgleichgewichtstransport durch einen Anderson Quantenpunkt, der an metallische, d.h. fermionische, Zuleitungen koppelt. Wir führen den neu entwickelten ISPI Algorithmus ein, welcher dazu dient das zugrundeliegende fermionische Realzeit Pfadintegral in ab-initio deterministischer Weise zu berechnen. In ähnlicher Weise wie die QUAPI Methode baut ISPI darauf auf, daß zeitlich nichtlokale Korrelationen nach einer charakteristischen Gedächtniszeit trunkiert werden können und so nicht-Markovsche Effekte voll berücksichtigt werden können. Um die Verläßlichkeit des neuen Algorithmus zu verifiziern vergleichen wir unsere Resultate mit bekannten Ergebnissen in verschiedenen Parameterbereichen und finden gute Übereinstimmung mit approximativen Methoden.

The thesis is based on the following original articles:

- Chapter 3
  J. Eckel, S. Weiss and M. Thorwart,
  Phonon-induced decoherence and dissipation in donor-based charge qubits,
  Eur. Phys. J. B **53**, 91 (2006).

- Chapter 4
  J. Eckel, J. H. Reina and M. Thorwart,
  Coherent control of an effective two-level system in a non-Markovian biomolecular environment,
  accepted for publication in New. J. Phys., see also `arXiv:0903.2936`.

- Chapter 5
  M. Thorwart, J. Eckel, J. H. Reina, P. Nalbach and S. Weiss,
  Enhanced quantum entanglement in the non-Markovian dynamics of biomolecular excitons,
  submitted to Chem. Phys. Lett., see also `arXiv:0808.2906`.

- Chapter 6
  S. Weiss, J. Eckel, M. Thorwart and R. Egger,
  Iterative real-time path integral approach to nonequilibrium quantum transport,
  Phys. Rev. B **77**, 195316 (2008); *ibid* **79**, 249901(E) (2009).

Contents

Chapter 1

Introduction

Over the past three decades, systems intermediate between macroscopic and microscopic scales, where quantum coherence becomes relevant, have developed into the main focus of research in condensed-matter physics. To characterize this field the notion *mesoscopic physics* has been assigned to term this field.

When one is interested in the dynamical processes in complex many-body systems, one usually applies an external force to the system of interest. This force drives the system out of equilibrium and one then measures the time-dependent response of the system on that force. Well established experimental setups are quasielastic and inelastic scattering of photons, electrons or neutrons off a sample. Information on the system dynamics is then obtained from the line shape of the measured spectra. Other experimental methods are, e.g. spin relaxation experiments or the measurement of transport characteristics. All these experiments yield information about the behavior of the dynamical fluctuations due to the external force. The theoretical description of these phenomena is based on correlation functions. In that sense time correlation functions are within the center of interest of theoretical studies of the relaxation and transport properties of non-equilibrium systems.

A central idea for any real dissipative system is the separation of a global quantum system into a subsystem of interest and the environment which is supposed to be in thermal equilibrium. Since the system of interest is coupled to a quantum-statistical environment this results in a fluctuating force. This force acts on the system of interest and though reflects the properties of the environment. It is one central feature of the fluctuating force to cause decoherence and dissipation.

Decoherence is known as the phenomenon that the superposition of macroscopically pronounced states decays on a short time scale. Since information about quantum interferences is carried away in any physical form into the surrounding (even by means of a microscopic object or in an uncontrollable, that is thermal form, from which the phase information cannot be retrieved in a practical way), decoherence is present for any realistic system showing quantum interference effects.

From the point of view of the measurement process, which is a central point in the interpretation of quantum theory, the environment plays the role of a constant macroscopic measurement apparatus, leading to a persistent destruction of phase

correlations. A consistent theoretical description of dissipation and decoherence phenomena in open quantum systems has to take into account all time non-local correlations, since, as will become clear from chapter 2, the autocorrelation function of the environment has a certain width. These time non-local correlations are termed non-Markovian or memory effects. If these memory effects are not taken into account one has to validate carefully for which physical situation they can safely be neglected.

Besides these conceptual and fundamental issues, quantum physics nowadays plays a fundamental role in many technological areas. One of the most fascinating areas that has made great effort during the past decades is quantum information technology. On the one hand nowadays nanofabricated semiconductor based quantum dots allow for controllable single electron transport and the detailed understanding of the transport properties is challenging. On the other hand entanglement as a fundamental consequence of the quantum-mechanical superposition principle is nowadays expected to be one of the main resources for quantum information processing. Clearly all these systems and concepts suffer from decoherence and dissipation and thus a comprehensive qualitative and quantitative understanding of the underlying processes is desirable.

In the remainder of this chapter we give motivation and introductory paragraphs to the chapters 3-6 where the results of the thesis at hand are presented. Chapter 2 gives a short introduction on the concepts of open quantum systems and on the formalism relevant for this work.

Phonon-induced decoherence and dissipation in donor-based charge qubits

As a first system on which we examine the influence of time non-local correlations on the dynamics of the system we choose in chapter 3 a solid-state based charge qubit embedded in a dissipative phonon environment. The choice of such a system is motivated by the fact that during the last decade it turned out that solid-state based nano structures are promising candidates for the realization of quantum information processing devices [1]. The building blocks are quantum mechanical two-state systems (qubits) and some of the proposed designs have been realized in groundbreaking experiments, see ref. [1] for a recent review on this field. Thereby, various approaches have been undertaken, ranging from superconducting flux and charge qubit devices to devices using the spin or the charge degrees of freedom of individual electrons in confined geometries. Aiming at an extreme miniaturization of solid-state devices down to the nm-scale, it has been proposed to implant individual dopant atoms in a semiconductor crystal and to use nuclear spin states of buried phosphorus dopants to realize a spin-qubit (Kane's proposal [2]). Complementary to the Kane architecture, the charge degree of freedom of a single electron shared by two donor atoms in a host crystal can be used for the coding of the logical information, as proposed in ref. [3, 4]. Thereby, the logical states $|0\rangle$ and $|1\rangle$ are realized by the charge states of the double-donor-system with the excess electron either located on the left or on the right donor. The transition between these states

occurs via tunneling of the electron between the two dopants. The charge qubits can in principle be controlled efficiently by external electric fields, e.g., by an applied gate voltage. This property renders the proposed architecture attractive for realizing control schemes with available fabrication and read-out technologies [4]. Experimental progress for this kind of ion-implanted Si:P nanostructures has been reported recently [5].

On the other hand, all these solid-state qubits suffer from the large number of degrees of freedom due to their embedding in a complex many-particle environment. The environmental decoherence and dissipation lead to a deterioration of the performance of quantum logic operations and also strongly influence entanglement between qubits [6] necessary for quantum gate operations. Various sources of decoherence include nuclear spins, phonons, and electromagnetic fluctuations in the host crystal. To gain a detailed understanding of the various decoherence mechanisms, realistic model calculations have to be performed which then allow to sort out the different contributions. In chapter 3 we concentrate on the influence of a phonon bath on the shared electron. To be definite, we consider a charge qubit formed by two group-V donors as proposed in ref. [7]. One donor is formed by a phosphorus atom while the second donor will be one of the class {Bi, As, P, Sb}. The donor pair is assumed to be implanted in a silicon crystal host and share a common electron. We consider linear acoustic phonons coupled to the electron and determine the dynamics of the charge oscillations between the two donors. Due to the particular geometry, a tailored phonon environment is formed for the electron which depends non-monotonously on the phonon frequencies. In order to provide accurate quantitative results on the decoherence and dissipation rates, we apply the numerically exact iterative quasi-adiabatic propagator path integral (QUAPI) scheme [9,8] and introduce it in some detail here, since we will also make use of this method in the chapters 4 and 5. In particular, we have improved the widely used method by providing a recipe to completely eliminate the Trotter discretization error. This allows to obtain fully convergent exact results by extrapolation to a vanishing Trotter increment [10].

An appealing alternative to extensive numerical studies are approximate calculations which, for instance, rely on the weak coupling between the qubit and the environment. The most familiar Born-Markov or weak-coupling approximation (WCA) [11], which basic assumptions will be outlined in chapter 2, yields to simple closed expression for the decoherence and relaxation rates. However, they apply for typical situations when the bath has a smooth frequency distribution [11]. In our case, the environment is particularly shaped by the geometry leading to a non-monotonous bath spectral density. Hence, it is not *a priori* clear whether the widely used WCA is appropriate and a careful check is desirable. By comparing the exact numerical QUAPI results with the approximate WCA results below, we will show that for realistic parameters, the WCA typically yields the correct order of magnitude for the decoherence and relaxation rates. However, differences are noticeable when a quantitative comparison is made. We furthermore note that the calculated phonon decoherence and relaxation rates comprise a fundamental upper

limit for the coherence properties of this architecture which can hardly be overcome.

Coherent control of an effective two-level system in a non-Markovian biomolecular environment

It is a natural question if and to what extend the time scale on which quantum coherent dynamics is relevant as, e.g. studied in chapter 3, can be enlarged by an external driving force applied to the system of interest. This is the main purpose of chapter 4 and indeed, the theoretical description of driven quantum systems has discerned novel effects related to the control of quantum tunneling (see, e.g., [12] for a comprehensive review). Classical examples of the achieved degree of quantum control are the manipulation of trapped atoms in quantum optics [13] and the control of chemical reactions by external laser fields [12]. In quantum optics, it has been experimentally demonstrated that the time evolution of a two-level atom can be significantly modified by means of a frequency modulated excitation of the atom by use of a microwave field [14]. Moreover, it has been shown that tunneling of an initially localized state in a double well potential can be almost completely suppressed by a properly tailored external driving force [15]. In addition, the experimental demonstration of a quantum coherent dynamics in a superconducting flux qubit coupled to a superconducting quantum interference device (SQUID) has been reported [16].

To gain a deeper understanding of the quantum dissipative dynamics, a quantitative model including the effects of time-dependent driving, decoherence and dissipation is required. One generic model to investigate these effects is the time-dependent spin-boson model [12, 11] (described in detail in chapter 2), where the tunnel-splitting of the coherent two-level system (TLS) is usually denoted by Δ. The environment is commonly described via the spectral density $J(\omega)$ [11]. In many cases, an Ohmic spectral density, where $J(\omega) \propto \omega$, occurs, as in the case of an unstructured electromagnetic environment, where all transitions within the system are damped equally [11].

To take into account the fact that the environmental frequencies are in principle limited, a high-frequency cut-off ω_c has to be introduced. This frequency scale is related to the time scale on which the environmental degrees of freedom evolve [11]. In many cases, ω_c is chosen to be the largest frequency scale in the problem ($\omega_c \gg \Delta$), which corresponds to the fact that the environmental fluctuations evolve on the shortest possible time scale, and hence the bath is 'fast'. This describes, e.g., electromagnetic fluctuations in a crystal host [11,17] or in a superconductor [11]. Under this condition, a Markov assumption can be made yielding an effective time-local dissipative dynamics. This is also the regime in which Bloch-Redfield type master equations (see chapter 2) are commonly used [18], typically in connection with the additional assumption of weak system-bath coupling. The opposite case, when $\omega_c \ll \Delta$ describes an effective adiabatic bath which can be treated in a rather simplified manner [11]. There are, however, relevant situations when the bath fluctuations occur on a similar time scale on which the system evolves, i.e., $\omega_c \simeq \Delta$. This, for

instance, typically occurs in the quantum coherent dynamics at the initial stage of photosynthesis in complex biomolecular structures [18, 21, 20, 19, 22]. It has only recently been experimentally hinted that the efficiency of the energy transfer from the light harvesting antenna complex to the chemical reaction center is promoted by the appearance of a quantum coherent dynamics [23, 24]. This hypothesis is further underpinned in [23, 24], where it has been evidenced that the collective long-range electrostatic response of the biomolecular protein environment to the electronic excitations should be responsible for the measured long-lived quantum coherences. In the experiment reported in [23], a quantum coherent excitonic dynamics in the energy transfer among bacteriochlorophyll (BChl) complexes over a time of around 660 fs has been measured at a temperature of 77 K. Such a dynamics is highly non-Markovian and more elaborate techniques have to be applied in order to provide an appropriate theoretical description.

In chapter 4, we consider an externally driven TLS subjected to an Ohmic environment with an exponential cut-off. Here, the focus is on the non-Markovian influence of a finite ω_c on the quantum coherent dynamics. The appropriate numerically exact tool to investigate non-Markovian dynamics is again the QUAPI method. We are able to investigate the entire parameter regime of weak as well as strong system-bath coupling situation beyond the often used scaling limit $\Delta \ll \omega_c$. We compare the weak coupling approximation based on a Born-Markov approach against the QUAPI method and show that the inclusion of non-Markovian effects is indeed necessary to obtain the correct result in the regime $\omega_c \simeq \Delta$.

The investigation of the parameter regime $\omega_c \simeq \Delta$ is motivated by the fact that a slow environment is indeed of physical relevance to light-harvesting biomolecular complexes which are embedded in a polar solvent [22]. Here, we consider a model for an effective TLS constructed from two interacting chromophores coupled to a protein-polar solvent reservoir. Furthermore, we drive the effective biomolecular TLS with an external laser and show that the Hamiltonian for the full system can be described in terms of the driven spin-boson model. The driven dissipative dynamics is investigated with the objective of understanding basic quantum interference phenomena which could be realized as proof-of-principle quantum coherent control experiments in light harvesting (LH) photosynthetic complexes such as LH II [18] or in artificially designed TLS nanostructures with specific bath properties. Indeed, there are promising proposals for experiments leading in this specific direction [25, 26]. Moreover we recall the detailed derivation of the spectral density for biomolecular complexes which indeed shows that the choice of an Ohmic spectral density is based on microscopic details of the environment.

We apply an external time-dependent driving field at frequency ω_l to the TLS and show in section 4.2.3 for moderate and strong driving that the amplitude of the forced oscillations in the stationary limit strongly depends on ω_l and, moreover, on ω_c. Most interestingly, it turns out that a slow environment together with a slow drive ω_l optimizes the forced oscillations in the stationary limit. Finally, in section 4.2.4, the effect of a slow dissipative environment on the coherent destruction of tunneling in the TLS is investigated. We find that the bath influence is indeed

strongest in the scenario $\omega_c \simeq \Delta$.

Enhanced quantum entanglement in the non-Markovian dynamics of biomolecular excitons

Since the results in chapter 4 provide evidence for the fact that a slow environment being non-Markovian in nature plays a constructive role for quantum effects we extend the previous model in chapter 5. Here, we investigate the quantum dynamics of two coupled TLS subjected to a common Ohmic environment. The observable of interested is the entanglement between the two TLS. Nowadays, entanglement is known to provide an important resource within quantum information technologies to perform certain tasks faster and in a more secure way [29, 28, 27]. Entanglement of a bipartite system can be successfully determined by means of the Peres-Horodecki criterion [30, 31] in a mathematically rigorous way. As mentioned above quantum coherent dynamics at the initial stages of photosynthesis in complex biomolecular structures seems to promote the efficiency of energy transfer from the light-harvesting antenna complexes to the chemical reaction centers [23, 24, 19, 20]. In that sense the two coupled TLS under investigation in chapter 5 are meant to be two pairs of Förster coupled excitons. Furthermore, the obtained time scales [24] for the short-time dynamics of the nuclear modes coupled to the excitonic states of two chromophores are almost identical. This points to the special and constructive role of the quantum environment for the photo-excitations. The often assumed coupling of the chromophores to fast and independent quantum baths does not hold in this case. In fact, the two chromophores are embedded in the *same* protein-solvent environment. These results corroborate experimental studies [19] which show that energy transport sensitively depends on the spatial properties of the delocalized excited-state wave functions of the *whole* pigment-protein complex. In addition, there are reports of coherently controlled wave packet quantum dynamics artificially generated by laser pulses in the light-harvesting antenna of the bacteria *Rhodopseudomonas acidophila* [20].

In performing a deterministic evaluation of real-time path integrals by means of the QUAPI method [8, 9], described in detail in chapter 3, we provide numerically exact results for the quantum coherent dynamics of photo-excitations in coupled chromophores in chapter 5. Similar to the driven TLS in chapter 4, the time evolution of the protein-solvent bath happens on time scales comparable to the exciton dynamics. We show that the non-Markovian effects help to sustain quantum coherence over rather long times. Furthermore, quantum entanglement [32] of two chromophore pairs is shown to be more stable under the influence of a non-Markovian bath. Even at high temperatures, a slow bath can generate a considerable degree of entanglement, a feature absent in the Markovian case. In passing, we mention that recently, quantum entanglement of two optical two-level systems coupled to a common localized environmental mode has been studied beyond the Markov approximation at zero temperature [33].

Iterative real-time path integral approach to nonequilibrium quantum transport

The systems under consideration in chapter 3-5 are coupled to an environment being bosonic in nature. If one is interested in the transport properties of quantum systems one is in many cases concerned with systems which are coupled to an environment which is *fermionic* in nature. Although there are conceptual similarities, like for instance the evidence of time non-local, i.e., non-Markovian correlations, the description of the real-time dynamics is of fundamental difference, which is addressed in chapter 6.

Quantum transport has attracted theoretical and experimental research since it offers the possibility to investigate quantum many-body properties at as well as out of thermodynamic equilibrium [34]. The ongoing improvement in miniaturization down to the nanometer scale allows to study electron transport in ultra-small devices, e.g., in single molecules or artificially designed quantum dots [35,36,37,38,39, 40]. There is a broad variety of interesting physical effects, due to interactions or the nonequilibrium conditions arising when a bias voltage is applied to the source and drain electrodes [41,42,43]. These range from Coulomb blockade via coherent (e.g., resonant tunneling) transport to the Kondo effect, to name but a few. While on the experimental side, progress stems from an increased control of fabrication processes, many theoretical works deal with refined approximation schemes applicable in different parameter regimes. However, *exact* theoretical results — either analytical or numerical — for nonequilibrium quantum transport systems are rare, mainly because of the lack of adequate methods allowing to tackle such questions. There clearly is a considerable need for numerically exact methods to describe nonequilibrium quantum transport, both to check analytical (and usually approximate) approaches and to connect theory to experiment. Here, we mean by nonequilibrium transport specifically those phenomena which go beyond the standard approach of linear response to the applied bias voltage.

In chapter 6, we propose a novel numerical scheme denoted as *iterative summation of real-time path integrals* (ISPI), in order to address quantum transport problems out of equilibrium. Many-body systems driven out of equilibrium are known [44,45,46] to acquire a steady state that may be quite different in character from their ground-state properties. Details of the steady state may depend on the nature of the correlations, as well as on the way in which the system is driven out of equilibrium. While there are a variety of nonperturbative techniques in place to study equilibrium systems, many of these methods cannot be extended to nonequilibrium systems in a straightforward way.

Different approximations have been pursued previously in order to tackle nonequilibrium situations. For instance, transport through an Anderson dot in the Kondo regime has been described theoretically along several different lines, e.g., for the asymptotic low-energy regime by Fermi liquid theory [47], via interpolative schemes [48], using integrability concepts [49], or by the perturbative renormalization group [45,50]. Transport features of the Anderson model have also been discussed by per-

turbation theory in the interaction strength [51, 52]. Sophisticated nonperturbative methods have been developed in order to extract exact results out of equilibrium for special models, where integrability is available. For instance, the interacting resonant level model presently enjoys much interest [53, 54, 55, 56, 57, 58, 59]. Universal aspects of nonequilibrium currents in a quantum dot have been discussed in ref. [54]. In various perturbative regimes, this model has been addressed by field theory methods [56,57,58,59]. However, the underlying theoretical concepts are still under much debate, and partially conflicting results were reported in the literature, cf. refs. [56, 57, 58].

The above discussion shows that precise numerical simulation tools are in great demand in this field. Let us briefly review the existing numerical methods available for nonequilibrium transport. Much effort has been directed to the application of renormalization group (RG) techniques to this problem. For instance, a perturbative real-time RG analysis of nonequilibrium transport has been performed [60], and steps towards the appropriate generalization of the density matrix renormalization group technique have appeared [61, 62]. In addition, the functional RG approach has been generalized to nonequilibrium recently [63]. It forms a systematic and fast perturbative expansion scheme, yielding reliable results for small interaction strengths, where the infinite hierarchy of equations for the self-energy can be cut after the first few steps. Moreover, a possible extension of Wilson's numerical RG approach to nonequilibrium has been discussed [64, 65]. Another line of attack considered numerically exact real-time quantum Monte Carlo (QMC) simulations (for the corresponding equilibrium case, see refs. [66,67]). Due to the sign problem, however, these calculations become increasingly difficult at low temperatures. Refined multi-level blocking techniques [68,69] allow to achieve further progress, but numerical simulations remain hard within this approach. (For recent progress, however, see ref. [70, 71, 72, 73].) Let us also mention the flow equation method, which has been applied to study the nonequilibrium Kondo effect [74]. Finally, a very recent development considers non-standard ensembles to describe steady state transport, but involves a numerically troublesome analytic continuation [75].

Our ISPI approach, described in detail in chapter 6, provides a novel alternative, and in principle numerically exact, method to tackle out-of-equilibrium transport through correlated quantum dots. The method is deterministic and, hence, there is no sign problem. It is based on the evaluation of the full nonequilibrium Keldysh generating function, including suitable source terms to generate the observables of interest. It builds on the fact that the fermionic leads induce self-energies that are non-local in time, but which decay exponentially in the long-time limit at any finite temperature. Thus, a memory time exists such that within this time span, the correlations are exactly taken into account, while for larger times, the correlations can be dropped. This allows to construct an iterative scheme to evaluate the generating function. An appropriate extrapolation procedure allows then to eliminate both the Trotter time discretization error (the Hubbard-Stratonovich (HS) transformation below requires to discretize time), and the finite memory-time error, yielding finally the desired numerically exact value for the observables of interest. The extrapola-

tion procedure is convergent for not too low temperatures, since then memory effects are exponentially small for long times. If the extrapolation converges, we thereby obtain numerically exact results for nonequilibrium quantum transport properties of interacting systems.

The ISPI scheme is implemented here for the example of the well-known single-level Anderson impurity model [76, 77, 78, 79, 80], but appropriately modified, it can be applied to other quantum dot models as well. The nonequilibrium current is calculated from a generating function, represented as a real-time path integral in the Keldysh formalism. After a Hubbard-Stratonovich transformation employing an auxiliary Ising spin field, all fermionic degrees of freedom (of the dot and the leads) can be integrated out exactly, however, at the price of introducing time-nonlocal self-energies for the leads and a path summation over all Ising spin configurations. For this, an iterative summation scheme is constructed, exploiting that the time-nonlocal correlations in the lead self-energy effectively decay exponentially at finite temperature T or bias voltage V, thereby setting the characteristic memory time. For larger times, the correlations are exponentially small and will be neglected. The full time-discretized Keldysh Green's function (GF) of the dot then assumes a band matrix structure, where the determinant can be calculated iteratively using its Schur form. The scheme is constructed such that within the range set by the memory time, the path integral is evaluated exactly. The remaining systematic errors are the Trotter time discretization and the finite-memory error. Both, however, can be eliminated in a systematic way based on a Hirsch-Fye type extrapolation procedure. Based on the above construction principle, our approach cannot be applied at very low energies ($T, V \to 0$), where, fortunately, other methods are available. For finite temperatures, the requirement of not too long memory times can be met, and the spin path summation remains tractable.

The common features to all the parts of the present thesis are time non-local, i.e., non-Markovian correlations and their relevance for the real-time dynamics of open quantum systems. Since it is challenging and for certain system parameters even impossible to take into account these features for bosonic as well as for fermionic systems analytically we make use of extensive numerical methods. For the bosonic systems under investigation in the chapters 3-5 we use the well established QUAPI scheme and develop a new scheme, the ISPI scheme, to tackle open quantum system being fermionic in nature in chapter 6. Both methods are related in the sense that they fully take into account the non-Markovian features, i.e., memory-effects of the environment which decay for bosonic as well as for fermionic environments exponentially in time for finite temperatures. By comparison with approximate analytical results we provide evidence for the fact that certain properties, as e.g. the entanglement generation of two biomolecular TLS coupled to a common environment in chapter 5, are rooted on purely non-Markovian features of the environment which though cannot be neglected.

Chapter 2

Open Quantum Systems

In condensed phases we are often concerned with rather complex physical situations that can adequately be described by a global model system consisting only of one or a few dynamical variables. This model system is contact with a huge environment of which the number of degrees of freedom is large or even infinity. When one is interested in the physical properties of the small system only this system has to be handled as an open quantum system [11]. In this chapter we give a brief introduction to the theory of open quantum system which is the underlying concept for the present thesis as a whole. Hereby we follow the presentation of [11, 81, 82].

2.1 Classical Langevin equation

Conveniently the dynamics of a classical open system is described in terms of a Langevin equation in which all the effects of the environment are encapsulated in a friction force and a fluctuating force. For an open system with a single degree of freedom $q(t)$ and *linear*, i.e., state-independent dissipation, the frictional force is a linear functional of the history of the velocity $\dot{q}(t)$. The stochastic force $\xi(t)$ succeeds Gaussian statistics and is consequently fully characterized by the ensemble averages [11]

$$\langle \xi(t) \rangle = 0, \qquad \langle \xi(t)\xi(t') \rangle \equiv \chi(t-t') \,. \tag{2.1}$$

In contrast to a white noise source where the stochastic force is δ-correlated, for many situations of practical interest, the heat reservoir is a source of noise with a finite memory time. For colored noise, the dynamics is described in terms of the generalized Langevin equation (including a mass term)

$$M\ddot{q}(t) + M \int_{-\infty}^{t} dt' \, \gamma(t-t') + V'(q) = \xi(t) \,. \tag{2.2}$$

Eq. (2.2) describes e.g. a particle with mass M moving in an environment that obeys colored noise, driven by a systematic force $-V'(q)$, where $V(q)$ is an externally applied potential. The mean effect of the environment on the particle is contained

in the memory friction force which is expressed in terms of the causal damping kernel $\gamma(t) = 0$ for $t < 0$. Thus, on average the fluctuating force $\xi(t)$ vanishes and the stochastic nature of $\xi(t)$ is again described by its autocorrelation function $\langle \xi(t)\xi(t') \rangle$.

2.2 System-bath model

Within the traditional system-reservoir model we consider a system with one or a few degrees of freedom coupled to a huge reservoir of harmonic excitations above a stable ground state. The central system of interest can be imagined to be a quantum system, e.g. a damped quantum mechanical harmonic oscillator. For a geometrically *macroscopic* environment the coupling to an individual bath mode (i.e. the harmonic excitations) is weak, since the interaction of the system with each individual degree of freedom of the reservoir is inversely proportional to its volume. Therefore it is physically reasonable to assume that the coupling between system and environment is linear in the reservoir coordinates. As it will turn out in the sequel this is a nice property since it allows for eliminating the bath exactly. Note that nevertheless the coupling of the individual bath mode to the system is weak, the dissipative influence of the reservoir can be strong since the number of bath modes can even go to infinity.

The most general Hamiltonian with these properties is

$$H = H_S + H_B + H_{SB} \,. \tag{2.3}$$

Here,

$$H_S = \frac{P^2}{2M} + V(q) \tag{2.4}$$

is the Hamiltonian of the system, e.g. a particle with mass M moving in a potential $V(q)$, where P is the momentum conjugate to the position q of the particle.

$$H_B = \sum_{\alpha=1}^{N} \frac{p_\alpha^2}{2m_\alpha} + \frac{1}{2} m_\alpha \omega_\alpha^2 x_\alpha^2 \tag{2.5}$$

describes the environment consisting of N harmonic oscillators with frequency ω_α, a mass m_α and the coordinate x_α. The interaction between system and environment reads

$$H_{SB} = -\sum_{\alpha=1}^{N} F_\alpha(q) x_\alpha + \Delta V(q) \,. \tag{2.6}$$

$\Delta V(q)$ is a counter-term which depends on the parameters ω_α, m_α and on $F_\alpha(q)$, but not on the dynamical variables x_α of the reservoir. This term serves to cancel a renormalization of the potential and if it is omitted, e.g. a free particle would turn into harmonically bound one, due to a renormalization of the potential [82]. For the case that we require strictly linear dissipation $F_\alpha(q)$ is constraint by $F_\alpha(q) = c_\alpha q$

and the total Hamiltonian reads

$$H = \frac{P^2}{2M} + V(q) + \frac{1}{2}\sum_{\alpha=1}^{N} \frac{p_\alpha^2}{m_\alpha} + m_\alpha \omega_\alpha^2 \left(x_\alpha - \frac{c_\alpha}{m_\alpha \omega_\alpha^2} q \right)^2 \tag{2.7}$$

which is often referred to as the Caldeira-Leggett model [83].

2.3 Quantum Langevin equation

In order to prove that the Hamiltonian (2.7) describes dissipation if one is interested in the system degrees of freedom solely we start with the Heisenberg equation of motion which will be solved for the reservoir degrees of freedom. This will lead to an effective operator valued equation of motion which then can be compared with its analogous counterpart from section 2.1. The Heisenberg equation

$$\dot{A} = \frac{i}{\hbar}[H, A]\,, \tag{2.8}$$

with A denoting the momentum operator of the system $P = M\dot{q}$ and the reservoir $p_\alpha = m_\alpha \dot{x}$ respectively, gives the equations of motion

$$M\ddot{q} + \frac{dV}{dq} + q\sum_{\alpha=1}^{N} \frac{c_\alpha^2}{m_\alpha \omega_\alpha^2} = \sum_{\alpha=1}^{N} c_\alpha x_\alpha \tag{2.9}$$

for the system and

$$m_\alpha \ddot{x}_\alpha + \omega_\alpha^2 x_\alpha = c_\alpha q \tag{2.10}$$

for the bath degrees of freedom, where x_α is the position operator of the individual bath oscillator. Considering the position operator of the system $q(t)$ as given the inhomogeneous second order differential eq. (2.10) is formally solved by [11, 82]

$$x_\alpha(t) = x_\alpha(t_0)\cos\,\omega_\alpha(t-t_0) + \frac{p_\alpha(t_0)}{m_\alpha\omega_\alpha}\,\sin\,\omega_\alpha(t-t_0) + \int_{t_0}^{t} ds\,\frac{c_\alpha}{m_\alpha\omega_\alpha}\,\sin\left[\omega_\alpha(t-s)\right] q(s)\,, \tag{2.11}$$

with $p_\alpha(t_0)$, $x_\alpha(t_0)$ denoting the initial condition of the reservoir oscillators. The bath degrees of freedom are now eliminated by inserting this solution into the inhomogeneity of eq. (2.9). By partial integration one then obtains the quantum Langevin equation

$$M\ddot{q} + M\int_{t_0}^{t} ds\,\gamma(t-s)\,\dot{q}(s) + \frac{dV}{dq} = \zeta(t)\,. \tag{2.12}$$

For clarity we have dropped a transient initial slip term steming from the potential renormalization in eq. (2.6), for details, see e.g. [11]. $\gamma(t)$ represents the damping kernel

$$\gamma(t) = \frac{1}{M}\sum_{\alpha=1}^{N} \frac{c_\alpha^2}{m_\alpha\omega_\alpha^2}\cos\,\omega_\alpha t \tag{2.13}$$

and

$$\zeta(t) = \sum_{\alpha=1}^{N} c_\alpha \left[\left(x_\alpha(t_0) - \frac{c_\alpha}{m_\alpha \omega_\alpha^2} \right) \cos\, \omega_\alpha (t - t_0) + \frac{p_\alpha(t_0)}{m_\alpha \omega_\alpha} \sin\, \omega_\alpha (t - t_0) \right] \tag{2.14}$$

is a time dependent operator valued fluctuating force that depends on the initial conditions of both the system and the reservoir which at finite temperature are stochastically distributed. The mean value of $\zeta(t)$ satisfies

$$\langle \zeta(t) \rangle_B = 0\,, \tag{2.15}$$

where $\langle \cdot \rangle_B = \mathrm{tr}(\rho_B^0 \cdot)$ is the canonical distribution for the reservoir Hamiltonian (2.5) at temperature $T = (k_B \beta)^{-1}$ (k_B Boltzmann constant). To elucidate further that the quantum Langevin equation is depending on a memory-friction force one can derive the autocorrelation function of $\zeta(t)$ by taking the equilibrium expectation values for the correlations of the single harmonic oscillators of the reservoir. For $t > s$ the autocorrelation function then reads

$$\begin{aligned} \langle \zeta(t)\zeta(s) \rangle_B &= \langle \zeta(t - s + t_0)\zeta(t_0) \rangle_B \qquad (2.16) \\ &= \hbar \sum_{\alpha=1}^{N} \frac{c_\alpha^2}{2 m_\alpha \omega_\alpha} \left[\coth\, \frac{\hbar \omega_\alpha \beta}{2} \cos\, \omega_\alpha (t - s) - i \sin\, \omega_\alpha (t - s) \right]. \end{aligned}$$

Usually the reservoir is fully described via its spectral density

$$J(\omega) = \frac{\pi}{2} \sum_{\alpha=1}^{N} \frac{c_\alpha^2}{m_\alpha \omega_\alpha}\, \delta(\omega - \omega_\alpha)\,, \tag{2.17}$$

which includes all the relevant information about the reservoir oscillators and their coupling to the system of interest. Choosing a normal mode representation one can show that the system will reach its initial state after a characteristic time, the Poincaré recurrence time [84]. This characteristic time stems from the Poincaré recurrence theorem which applies for any energy conserving (Hamiltonian) system. The theorem is based on the two facts that the trajectories in phase space do not intersect and that the volume of the phase space space is conserved under dynamics. Note that nothing prevents the system from returning to its starting point before all the phase volume is exhausted. A trivial example of this is the harmonic oscillator. Systems that do cover all available phase volume are called ergodic. For a correct description of dissipation it is required that the Poincaré recurrence time is much longer than any time scale within the system. This is clearly the case for a continuous distribution of bath modes, i.e. $N \to \infty$. Indeed, for typical condensed phase application we are interested in in the following, $J(\omega)$ effectively becomes a continuous function in ω, i.e. $N \to \infty$ is fulfilled.

The autocorrelation function is then rewritten as $\langle \zeta(t)\zeta(s) \rangle_B = \hbar L(t - s)$ with

$$\begin{aligned} L(t) &= L_R(t) + L_I(t) \\ &= \frac{1}{\pi} \int_0^\infty d\omega\, J(\omega) \left[\coth\, \frac{\hbar \omega \beta}{2} \cos\, \omega t - i \sin\, \omega t \right]. \end{aligned} \tag{2.18}$$

Here, the expression in the square brackets is the autocorrelation function of a single bath oscillator weighted by the spectral density of the environment to obtain the full bath autocorrelation function. In the continuous limit the quantum Langevin equation is of the form (2.12) and the damping kernel is now related to the spectral density via

$$\gamma(t) = \frac{1}{M}\frac{2}{\pi}\int_0^\infty d\omega\, \frac{J(\omega)}{\omega}\, \cos\,\omega t\,. \tag{2.19}$$

The inversion of the the Fourier integral (2.19) reads

$$\widetilde{\gamma}(\omega) = \int_0^\infty dt\, \gamma(t)\, \cos\,\omega t = J(\omega)/M\omega\,. \tag{2.20}$$

Note that the quantum mechanical quantity $J(\omega)$ is fully determined by quantities that already appear in the classical phenomenological equation of motion [11], which remains valid in the case of linear, i.e., state-independent dissipation. In the classical limit $\hbar\omega \ll k_B T$ the autocorrelation function of the stochastic force is of the form $\langle \zeta(t)\zeta(s)\rangle_B = M k_B T \gamma(t-s)$ and the quantum Langevin equation becomes equivalent to the classical Langevin equation (2.2).

2.3.1 Special case: Ohmic damping

For the case of strict Ohmic damping, the damping kernel (2.20) is frequency independent, i.e. $\widetilde{\gamma}(\omega) = \gamma$ and the spectral density is of the form

$$J(\omega) = \eta\omega = M\gamma\omega \tag{2.21}$$

for all frequencies ω. This specific form of the spectral density implies memory-less friction (Markovian limit) $\gamma(t) = 2\gamma\delta(t)$, i.e. the bath autocorrelation function is replaced by a δ-function. For a realistic system any spectral density falls off in the limit $\omega \to \infty$, otherwise certain physical quantities, e.g. the momentum dispersion, would diverge (for a detailed discussion in the context of quantum Brownian motion see ref. [11]). There is always a microscopic memory time setting the time scale for inertia effects in the environment. To account for this property, a frequency cut-off is introduced with a cut-off frequency ω_c. It suppresses the bath modes with $\omega \gtrsim \omega_c$ and in this work has a smooth exponential form with which the spectral density reads

$$J(\omega) = \eta_s \omega_{ph}^{1-s} \omega^s\, e^{-\omega/\omega_c}\,. \tag{2.22}$$

Here, we have introduced for $s \neq 1$ a reference frequency ω_{ph} so that the coupling constant η_s has the dimension viscosity for all s. The case $s > 1$ is called the super-Ohmic case and is, e.g. relevant for donor based charge qubit examined in detail in chapter 3.

The cut-off frequency ω_c sets the time scale ω_c^{-1} below which the friction kernel has a certain width and the system has a finite memory. In the often used scaling

limit, where ω_c is the largest frequency of the system, the memory time is short and a Markovian approximation provides at least a qualitatively reliable description of the system dynamics. However, the situation turns out to be completely different when ω_c is of the same order as relevant system energies which is, e.g. the case for the biomolecular system considered in chapter 4 and 5. Since the the time scale ω_c^{-1} on which the damping kernel is widened is large, the dynamics is highly non-Markovian in nature. Our results provide evidence for a constructive role of the non-Markovian environment in creating entanglement in biomolecular complexes, see chapter 5.

2.4 The spin-boson model

A generalized coordinate with which an effective potential with two separate minima at nearly the same energy is associated with provides a useful description for a wide variety of physical and chemical systems. When the thermal energies are small compared with the level spacing of the low-lying states only the ground states of the two energy minima are involved. Consequently the essential dynamics is restricted to a two dimensional Hilbert space. The TLS is the simplest model showing quantum interference effects, e.g. for a high barrier where the two spatially well separated states are localized in the left or right well, respectively, coupled via tunnel matrix element $\hbar\Delta$, see fig. 2.1. Consequently, this implies oscillation of the occupation of both wells. For condensed phase situation we are interested in here, the TLS is in contact with an environment which is often bosonic in nature. Since the TLS can be described within the pseudo-spin notation the model is known as spin-boson model.

A well-known example for an effective TLS is the ammonia molecule NH_3 [12]: Since the nitrogen atom is much heavier than its partners, it is motionless. The hydrogen atoms form a rigid equilateral triangle whose axis passes through the nitrogen atom. Consequently, the potential energy is a function of the distance q between the nitrogen atom and the plane defined by the hydrogen atoms. Thus the potential energy has two equivalent configurations of a stable equilibrium, which are symmetric with respect to the $q = 0$ plane. Quantum mechanically the hydrogens can tunnel back and forth between the two potential minima [85].

The Hamiltonian of the TLS reads

$$H_{TLS} = -\frac{\hbar}{2}\left(\Delta\sigma_x + \epsilon\sigma_z\right) , \tag{2.23}$$

where ϵ is a bias leading to detunig of the TLS and σ_i being the Pauli pseudo-spin matrices. In general ϵ can be time dependent, e.g. an externally applied laser field driving the TLS with periodic driving frequency. This will be of interest in chapter 4.

The basis of the TLS is formed by the localized states of the right $|R\rangle$ and the left $|L\rangle$ well which are eigenstates of σ_z with ± 1, respectively. The position operator is $q = \frac{1}{2}q_0\sigma_z$ and its eigenvalues $\pm\frac{1}{2}q_0$ are the positions of the localized states. The environment is modeled as a bosonic bath of harmonic oscillators with

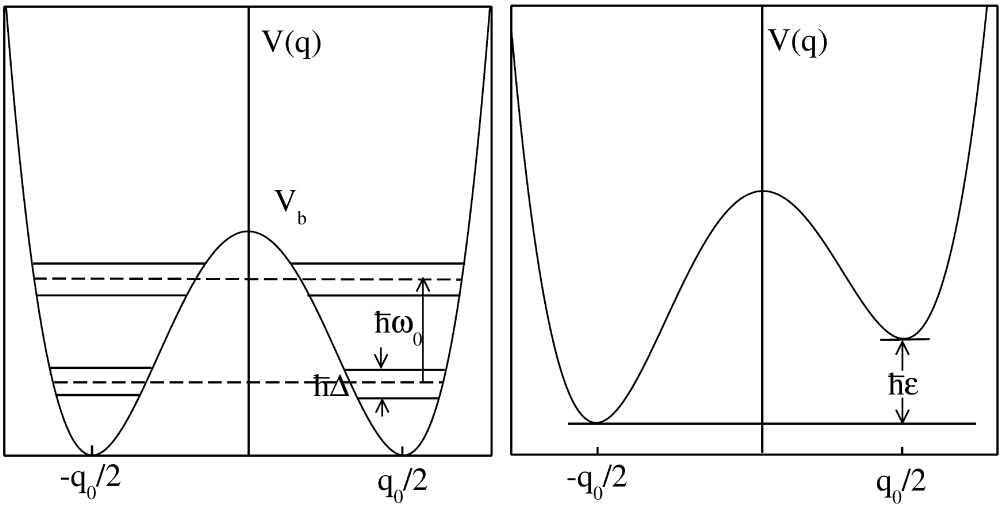

Figure 2.1: Symmetric double well potential (left) of the TSS with barrier height V_b and spacing $\hbar\omega_0$ between the first excited state and the ground state. The tunnel matrix element is $\hbar\Delta$. On the right the biased double well with a bias $\hbar\epsilon$ is presented.

the Hamiltonian (2.5) already given above. Assuming linear interaction between the TLS and its environment with the Hamiltonian

$$H_I = -\sigma_z \frac{q_0}{2} \sum_{\alpha=1}^{N} c_\alpha x_\alpha(t)\,, \tag{2.24}$$

the full spin-boson Hamiltonian is in its generic form

$$H = H_{TSS} - \frac{1}{2}\sigma_z \sum_{\alpha=1}^{N} \hbar\lambda_\alpha \left(b_\alpha + b_\alpha^\dagger\right) + \sum_{\alpha=1}^{N} \hbar\omega_\alpha b_\alpha^\dagger b_\alpha\,, \tag{2.25}$$

where the irrelevant zero-point energy has been neglected.

Here the interaction Hamiltonian and the Hamiltonian of the reservoir are expressed in terms of bosonic annihilation and creation operators b_α and $b_\alpha^\dagger$ with $x_\alpha = \sqrt{\hbar/(2m_\alpha\omega_\alpha)}\,[b_\alpha + b_\alpha^\dagger]$ and $p_\alpha = i\sqrt{(\hbar m_\alpha\omega_\alpha)/2}\,[b_\alpha^\dagger - b_\alpha]$. Again all environmental effects are included in the spectral density

$$G(\omega) = \sum_\alpha \lambda_\alpha^2 \delta(\omega - \omega_\alpha)\,, \tag{2.26}$$

where the coupling constant λ_α is related to c_α via [11]

$$\lambda_\alpha^2 = \frac{q_0^2 c_\alpha^2}{2\hbar m_\alpha \omega_\alpha}\,. \tag{2.27}$$

The spin-boson spectral density eq. (2.26) finally is related to the spectral density of the continuous model defined in eq. (2.17) via

$$G(\omega) = \frac{q_0^2}{\pi\hbar}\, J(\omega)\,. \tag{2.28}$$

2.5 Real-time dynamics

In this section we give a brief introduction on the description of the dynamics of open quantum systems in terms of real time path integrals. This formalism has been successfully used in the past decades for many problems in quantum dissipative systems. Moreover the formulation of the problem in terms of Feynman path integrals is useful since the quantum Langevin equation introduced in section 2.3 is not solvable in general. This is due to the Heisenberg-operator character of the stochastic noise $\zeta(t)$ for practical physical purpose. Such operators lead to huge stochastic matrices which make the problem even numerically unsolvable. In what follows, the dynamics is formulated in terms of the functional integral description, a technique introduced by Feynman and Vernon in 1963 [86]. They derive the general result that the effect of the bosonic environment is included in functionals of the system coordinates only.

Due to the linear coupling between system and environment it is possible to derive a closed expression for the influence functional. In what follows the underlying global system is governed by the Hamiltonian (2.7) and the quantity of interest is the reduced density matrix (for a detailed derivation see, e.g. [11]) which reads in coordinate representation

$$\begin{aligned}\rho(q_f, q_f', t) &\equiv \int d\boldsymbol{x}_f\, \left\langle q_f, \boldsymbol{x}_f \right| W(t) \left| q_f', \boldsymbol{x}_f' \right\rangle \\ &= \int dq_i\, dq_i'\, d\boldsymbol{x}_i\, d\boldsymbol{x}_i'\, d\boldsymbol{x}_f\; K(q_f, \boldsymbol{x}_f, t; q_i, \boldsymbol{x}_i, t_0) \\ &\quad \times \left\langle q_i, \boldsymbol{x}_i \right| W(t_0) \left| q_i', \boldsymbol{x}_i' \right\rangle K^*(q_f', \boldsymbol{x}_f', t; q_i', \boldsymbol{x}_i', t_0)\,. \end{aligned} \tag{2.29}$$

The reduced density matrix describes the system's dynamics under the reservoir's influence. Here the time evolution operator

$$K(q_f, \boldsymbol{x}_f, t; q_i, \boldsymbol{x}_i, 0) = \left\langle q_f, \boldsymbol{x}_f \right| \exp(-iHt/\hbar) \left| q_i, \boldsymbol{x}_i \right\rangle \tag{2.30}$$

describes the evolution of the global system from a state $|q_i, \boldsymbol{x}_i\rangle$ at time $t_0 = 0$ to a state $\langle q_f, \boldsymbol{x}_f|$ at time t (the expression for K^* is analogous). It may be represented in the usual form of a path integral [1]

$$K(q_f, \boldsymbol{x}_f, t; q_i, \boldsymbol{x}_i, 0) = \int \mathcal{D}q\mathcal{D}\boldsymbol{x} \exp\left(\frac{i}{\hbar} S[q, \boldsymbol{x}]\right)\,. \tag{2.31}$$

[1] for a thorough introduction on the formalism of path integrals we refer to the book of Negele/Orland [87].

Here, the functional integration extends over paths with endpoints

$$q(0) = q_i; \qquad q(t) = q_f; \qquad q'(0) = q'_i; \qquad q'(t) = q'_f \tag{2.32}$$

and accordingly for the $\boldsymbol{x}$ which is the N-component vector $\{x_\alpha\}, \alpha = 1, \cdots, N$ for the bath oscillator coordinates and q denotes the system coordinates.

2.5.1 Feynman-Vernon influence functional

In all what follows in this work we assume the density operator at initial time $t = 0$ to be in product form which is achieved by assuming that the system and the reservoir are initially decoupled and the unperturbed reservoir itself is in equilibrium. We then have

$$W(t_0) = \rho_s(t_0) \otimes \rho_B^0 = \rho_s(t_0) \otimes Z_B^{-1} \exp(-\beta H_B^0)\,, \tag{2.33}$$

where $\rho_s(t_0)$ is the density operator of the system at t_0, and $Z_B = \exp(-\beta H_B)$ and H_B is the Hamiltonian (2.5) of the bath decoupled from the system. This initial state is completely uncorrelated pertaining to the system-reservoir coupling. Now we assume that the coupling is suddenly switched on at $t = 0^+$ and consider the dynamics for $t \geq 0$. Substitution of (2.29) into the initial state (2.33) and use of the propagator (2.31) yields [11]

$$\rho(q_f, q'_f, t) = \int dq_i\, dq'_i\; J_{\mathrm{FV}}(q_f, q'_f, t; q_i, q'_i, 0)\rho(q_i, q'_i, 0)\,, \tag{2.34}$$

where J_{FV} is a propagating function describing the time evolution of the reduced density matrix. It reads in path integral form

$$J_{\mathrm{FV}}(q_f, q'_f, t; q_i, q'_i, t_0) = \int \mathcal{D}q \int \mathcal{D}q'\, \exp\left\{\frac{i}{\hbar}\left(S_S[q] - S_S[q']\right)\right\} \mathcal{F}_{FV}[q, q']\,, \tag{2.35}$$

with S_S being the corresponding action to the system Hamiltonian (2.4). The remaining dynamics is included in the Feynman-Vernon influence functional [11, 86]

$$\mathcal{F}_{FV}[q, q'] = \exp\left[-\frac{1}{\hbar}\phi_{FV}[q, q']\right] \tag{2.36}$$

containing the entire influence of the bath on the system, with the influence phase [2]

$$\begin{aligned}
\phi_{FV}[q, q'] \;&=\; \int_{t_0}^{t} dt' \int_{t'_0}^{t'} dt''\, \{q(t') - q'(t')\}\, \{L(t' - t'')q(t'') - L^*(t' - t'')q'(t'')\} \\
&\quad + i\frac{\mu}{2} \int_{t_0}^{t} dt'\, \left\{q^2(t') - q'^2(t')\right\} \qquad (2.37) \\
&=\; \int_{t_0}^{t} dt' \int_{t'_0}^{t'} dt''\, \{q(t') - q'(t')\}\, \{\eta(t' - t'')q(t'') - \eta^*(t' - t'')q'(t'')\}\,.
\end{aligned}$$

[2] for details of the derivation we refer to [86, 88] and do not reiterate it again here.

The quantity $\mu = \sum_\alpha \frac{c_\alpha^2}{m_\alpha \omega_\alpha^2}$ is related to the spectral density (2.17) via

$$\mu = \frac{2}{\pi} \int \frac{J(\omega)}{\omega} \tag{2.38}$$

and the kernel L reads like in the continuous model in section 2.3

$$L(t) \equiv L'(t) + iL''(t) = \frac{1}{\pi} \int_0^\infty d\omega \, J(\omega) \left[\coth \frac{\hbar\omega\beta}{2} \cos \omega t - i \sin \omega t \right] . \tag{2.39}$$

Note that the imaginary part $L''(t)$ is related to the damping kernel (2.13) via

$$L''(t) = \frac{M}{2} \frac{d\gamma(t)}{dt} . \tag{2.40}$$

To elucidate further the role of the diagrams contributing to the influence phase $\phi_{FV}[q, q']$ it is convenient to simplify its imaginary part by substituting eq. (2.40) into eq. (2.37) and extract a local boundary condition (for details, see [11]). Moreover it is then useful to define symmetric and antisymmetric coordinates according to

$$r(t) = \frac{1}{2} \left(q(t) + q'(t) \right) ; \qquad y(t) = q(t) - q'(t) . \tag{2.41}$$

Together with this the influence phase is written in its usual form

$$\begin{aligned} \phi_{FV}[q, q'] &= \phi^{(N)}[y] + i\phi^{(F)}[r, y], \\ \phi^{(N)}[y] &= \int_{t_0}^{t} dt' \int_{t_0'}^{t'} dt'' \, y(t') L_R(t' - t'') y(t''), \\ \phi^{(F)}[r, y] &= M \int_{t_0}^{t} dt' \int_{t_0'}^{t'} dt'' \, y(t') \gamma(t' - t'') \dot{r}(t'') + M r(t_0) \int_{t_0}^{t} dt' \, \gamma(t') y(t') . \end{aligned} \tag{2.42}$$

The path $r(t)$ measures propagation along the diagonal of the density matrix, therefore termed quasiclassical path. The quantum fluctuations of the system are described within the path $y(t)$, since it is book-keeping the system's off-diagonal excursions while propagating [11]. The graphs representing $\phi^{(N)}[y]$ and $\phi^{(F)}[r, y]$ are depicted in figure 2.2. By exponentiation one obtains graphs containing any number of exchange lines represented by the two fundamental types.

2.5.2 Decoherence and friction

Following [11] we now comment on the physical meaning of the manifestation of the system-reservoir coupling and the effects caused by the influence functional. On the one hand a friction term $\int_0^t dt' \gamma(t - t') \dot{r}(t')$ is introduced into the equation of motion of the quasiclassical path $r(t)$, thus the action $\phi^{(F)}[r, y]$ introduces damping into the

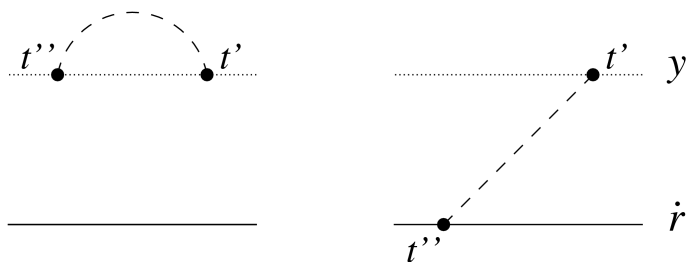

Figure 2.2: Graphical representation of the two contributions of $\phi_{\rm FV}[q,q']$. The left is the self-interaction of the off-diagonal path $y(t)$ and stands for $\phi^{(\rm N)}[y]$, where the exchanged line is the interaction $)L_{\rm R}(t'-t'')$. The right shows the correlations between $y(t)$ and $\dot{r}(t)$ in $\phi^{(\rm F)}[r,y]$, where the exchanged line represents the friction kernel $\gamma(t'-t'')$.

system and is depicted by the right diagram of figure 2.2. On the other hand the term $\phi^{(N)}[y]$ is the noise action that may pump energy back in a random way while the system is off-diagonal. This is directly related to the phenomenon of quantum coherence, which means that two different paths contributing to the propagation of a system may accumulate a phase difference φ. Then the probability interference term is multiplied by a phase factor $e^{-i\varphi}$. In the presence of system-reservoir coupling this leads to fluctuations of φ and the relevant quantity is now the statistical average $\langle e^{-i\varphi}\rangle$, the decoherence factor (for more details we refer to [89,90]). The noise action $\phi^{(N)}[y]$ determines the extinction of quantum interferences between the paths $q(t)$ and $q'(t)$ with the decoherence factor

$$\langle e^{-i\varphi}\rangle = e^{-\phi^{(N)}[y]}\,, \tag{2.43}$$

being independent of the quasiclassical path $r(t)$. In that sense the noise functional acts as a Gaussian filter which quenches the off-diagonal quantum fluctuations. Physically the reservoir continuously, in the time sense, measures the position of the system. Therefore it suppresses quantum interferences between the eigenstates of the system and thus drives the system into a more classical state, i.e. the off-diagonal excursions within the density matrix die out. Diagrammatically $\phi^{(N)}[y]$ is represented by the left diagram in fig. 2.2. The important role of the noise action is further illustrated in [11] by considering the Ohmic case $J(\omega)=\eta\omega$ in the white noise limit, i.e. at high temperatures. In this limit, one has $L'(t)=(2\eta/\hbar\beta)\delta(t)$ following from eq. (2.18). Thus for the decoherence factor of two localized states with spatial separation q_0 one finds

$$\left\langle e^{i\varphi}\right\rangle = e^{-\gamma_{\rm decoh}t}, \qquad \text{where} \qquad \gamma_{\rm decoh}=\eta\frac{q_0^2 k_B T}{\hbar^2}\,, \tag{2.44}$$

and the rate $\gamma_{\rm decoh}$ is the inverse time scale for the decoherence of these two states. The effect of the friction is included in the damping rate

$$\gamma_{\rm damp}=\frac{\eta}{M} \tag{2.45}$$

and the ratio of the two rates

$$\frac{\gamma_{\text{decoh}}}{\gamma_{\text{damp}}} = \frac{q_0^2 M k_B T}{\hbar^2} = \frac{q_0^2}{\lambda_{\text{th}}^2}\,, \tag{2.46}$$

relates the thermal de Broglie wavelength $\lambda_{\text{th}} = \hbar/\sqrt{M k_B T}$ to the range of coherence. Given a typical macroscopic situation [11], $M = 1$ g, $T = 300$ K, $q_0 = 1$ mm, the ratio $\gamma_{\text{decoh}}/\gamma_{\text{damp}}$ results in 10^{38}. As expected, for nearly all macroscopic objects friction is negligible on time scales where quantum coherences die out, which stays valid if the temperature is large and consequently $\gamma_{\text{decoh}}/\gamma_{\text{damp}} \gg 1$. However, for most realistic quantum systems this is not the case and one can calculate, e.g. the ratio for a quantum particle of mass M moving in a bistable potential with the oscillation frequency ω_0 at the well minima. With the characteristic energy $E_S = \hbar\omega_0$ of the system, the ratio is then $\gamma_{\text{decoh}}/\gamma_{\text{damp}} = (\beta E_S)^{-1}$. Such a rough estimate is feasible for typical experimental situations, such as SQUIDs, quantum dots or nano magnets. For the light harvesting biomolecular complexes under investigation in chapter 4 and 5 the typical energy scale is $E_s = 8$meV and $T = 77$K, leading to a ratio $\gamma_{\text{decoh}}/\gamma_{\text{damp}} = 8.7 \times 10^{-1}$. Thus for all these systems, quantum dissipation plays a fundamental role in understanding the underlying dynamical processes.

2.6 The Born-Markov approximation

Here, we give a brief introduction on the Born-Markov master equation formalism since this is frequently used in the description of quantum dissipative systems. We follow the statements of [91]. Moreover, in proceeding like this we aim for pointing out the nature of a non-Markovian environment which will be investigated by means of the QUAPI method in the sequel. The Born-Markov master equation allow one to treat many decoherence problems in a mathematically simple, and often closed, form. Comparison between models based on this equations and experimental data provide evidence that the Born-Markov assumptions yields reasonable results in many cases. However, for low-temperature solid-state systems and for the excitonic dynamics in biomolecular complexes, the dynamics is often non-Markovian in nature and/or we are concerned with a strong coupling situation and the Born-Markov approximation yields quantitative and even qualitative incorrect results. As an example, a non-Markovian environment plays a constructive role in the entanglement generation between two light-harvesting biomolecules, see chapter 5. This phenomenon is by no means covered within the Born-Markov approximation and more advanced techniques, as for instance the QUAPI scheme, are in demand.

The Born-Markov approximation consists of two parts:

1. *The Born-approximation*
   The system environment coupling is sufficiently weak and the environment is large compared to the system of interest so that changes of the environment's

density operator are negligible. This constitutes that the density matrix remains approximately in a product state at all times, i.e.

$$\rho(t) \approx \rho_s(t) \otimes \rho_B \tag{2.47}$$

where ρ_B is constant in time.

2. *The Markov-approximation*
   Memory effects of the environment are negligible, in the sense that any environmental self-correlations created via the system-bath coupling decay rapidly compared to the relevant time-scale on which the system of interest changes significantly its state.

The physical intuition behind the Born-approximation is that the interaction between system and environment is sufficiently weak (weak-coupling limit), and that the environment is large in comparison with the size of the system. It turns out that the Born-approximation is reasonable in many physical situations of interest. In many cases the system is coupled to a macroscopic large environment which, viewed as a whole, undergoes only negligible small changes in the course of the system-bath interaction compared to the change of the state of the system. In this case the back-action of the system on the environment can be ignored. Note that (2.47) allows for arbitrarily large changes of the density matrix of the system and environmental excitations induced by the interaction with the system are not excluded.

The Markov-approximation is motivated by the fact that it turns out that in many physical situations of interest, it is well-founded to assume that the environment tends to quickly "forget" any internal self-correlations that have been established by interaction with the system, described by the autocorrelation function (2.18). This assumption becomes valid if, e.g. for an Ohmic environment with an exponential cut-off frequency ω_c, eq. (2.22), the time-scale of the environment determined by ω_c is much faster than the relevant times-scale of the system. If the time-scales of the system and its environment coincide as for instance in the systems we investigate in chapter 4 and 5 this assumption fails even quantitatively.
In other words, within the Markov-approximation, the environment does not "keep track of its history". As a consequence any dynamically established quantum correlation between parts of the environment are destroyed on a timescale τ_{mem} much shorter than the timescale on which the density operator of the system changes noticeably. This assumption constitutes the Markov-approximation and it is appropriate, if the environment is only weakly coupled to the system, and if the environment is at a sufficiently high temperature. Markovian processes are also known from classical probability theory. Here, a stochastic process is Markovian if the probability of a particular event is independent of the previous events, the system retains no memory of its past and the steps are completely uncorrelated. For the real-time dynamics described in the previous section the Markov-approximation implies that the autocorrelation function of the environment (2.18) is effectively replaced by a δ-function.

2.7 Connection to a fermionic environment

Since we will deal with a fermionic environment in chapter 6 we shortly introduce the relation of the dissipative TLS with an Ohmic environment to the Kondo problem [92]. In what follows we only want to shed light on the qualitative analogies and do not go into the details of the derivation. For a thorough discussion we refer to [83, 11].

In its simplest form the Kondo problem is concerned with a single magnetic impurity of spin 1/2 exchanging via an exchange scattering potential with a band of free electrons. This can be described in terms of the Kondo Hamiltonian

$$H_K = \sum_{\vec{k},\sigma} \epsilon(\vec{k}) c^\dagger_{\vec{k},\sigma} c_{\vec{k},\sigma} + J\vec{S}\cdot\vec{s}(0)\,. \tag{2.48}$$

The operators $c^\dagger_{\vec{k},\sigma}$ create conduction electrons with wave vector $\vec{k}$ and spin index $\sigma = \pm 1$. The impurity spin is denoted by $\vec{S}$, whereas $\vec{s}(0)$ denotes the effective spin stemming from the conduction electrons at the impurity site $\vec{r} = 0$. Here, J is the exchange constant. The main difference to the dissipative TLS, namely the spin-boson model, introduced before is that in the Kondo problem a spin 1/2 interacts with a fermionic bath which introduces dissipation. The basic idea behind the relation is that the low-lying excitations of the electron gas in the Kondo Hamiltonian may be approximately described by bosons [83]. Consequently, it will turn out that the oscillators of the Ohmic environment within the dissipative TLS correspond to the spin-density excitations in H_K.

For pointlike interaction the problem is effectively reduced to a one-dimensional problem. Moreover for the low-temperature and long-time behavior the dominant excitations are the ones in the vicinity of the Fermi surface. The dispersion relation $\epsilon(\vec{k})$ may then be linearized around the Fermi energy ϵ_F in the form

$$\epsilon(\vec{k}) = \epsilon_F + \hbar v_F(|\vec{k}| - k_F)\,. \tag{2.49}$$

Measuring momentum from its reference value k_F, the free Fermion Hamiltonian reads

$$H_0^F = \hbar v_F \sum_{p\sigma} p c^\dagger_{p\sigma} c_{p\sigma}\,, \tag{2.50}$$

where $c^\dagger_{p\sigma}$ creates an electron with spin σ and momentum $|\vec{k}| = p + k_F$. Since p can never be smaller than $-k_F$ this Hamiltonian has to be supplemented with a high energy cutoff of the order of the bandwith. Generalizing furthermore the isotropic coupling in the original model to a different exchange constant $J_{||}$ for $S_z s_z$ and $J_\perp$ for $S_x s_x + S_y s_y$ one ends up with anisotropic Kondo Hamiltonian

$$H_K = \hbar v_F \sum_{p\sigma} p c^\dagger_{p\sigma} c_{p\sigma} + \frac{J_{||}}{4}\sigma_z \sum_\sigma \sigma c^\dagger_\sigma c_\sigma + \frac{J_\perp}{2}(\sigma_+ c^\dagger_\downarrow c_\uparrow + \sigma_- c^\dagger_\uparrow c_\downarrow) \tag{2.51}$$

with $\sigma_\pm = \frac{1}{2}(\sigma_x \pm i\sigma_y)$. Here, localized Wannier operators $c_\sigma^\dagger = L^{-1/2}\sum_p c_{p\sigma}^\dagger$ for an electron with spin σ at the origin have been introduced (L is the length of a normalization box such that the wave vectors $\vec{p}$ have integer values). Note that the constants $J_{||}$ and $J_\perp$ have the dimension energy times length. Therefore the relevant dimensionless coupling parameters are $\rho J_{||}$ and $\rho J_\perp$ with $\rho = (2\pi\hbar v_F)^{-1}$ being the single spin density of states at the Fermi surface. The anisotropic Kondo-Hamiltonian (2.51) only makes sense if there is a high-energy cutoff that sets the scale. The Kondo problem usually is considered as the large Coulomb interaction limit of the more general Anderson model, introduced in eq. (6.1). Indeed, the Anderson Hamiltonian (6.1) can be transformed via the Schrieffer-Wolff transformation into the Kondo Hamiltonian (2.48), for details see e.g. [77]. More generally speaking, the Coulomb interaction in the localized level may be viewed as an effective bandwith, which is often assumed to be of the order of the Fermi energy ϵ_F. A cutoff in frequency space around ω_c cuts off the momenta k around k_c with

$$k_c^{-1} = a = \frac{v_F}{\omega_c}\,. \tag{2.52}$$

a is an atomic length and ω_c^{-1} should be imagined to be the time an electron takes to pass the local spin. As low-energy limit of the Anderson model, the anisotropic Kondo Hamiltonian makes sense only for $J_{||} = J_\perp$ and small coupling $\rho J \ll 1$.

To finally derive the equivalence between the Kondo Hamiltonian and the spin-boson model, a bosonized version of (2.51) is in need. Here, only the important steps of the derivation are sketched, for details, see [83]. To proceed, charge- and spin-density operators for the Fermions are introduced

$$\rho(k) = \sum_{p\sigma} c_{p+k,\sigma}^\dagger c_\sigma \qquad \sigma(k) = \sum_{p\sigma} \sigma c_{p+k,\sigma}^\dagger c_\sigma \tag{2.53}$$

with $\rho(-k) = \rho^\dagger(k)$; $\sigma(-k) = \sigma^\dagger(k)$ and $k > 0$. For a semi-infinite band with all states $p < 0$ the operators

$$b_k = \sqrt{\frac{\pi}{kL}}\rho(-k) \qquad \text{and} \qquad a_k = \sqrt{\frac{\pi}{kL}}\sigma(-k) \tag{2.54}$$

obey Bose commutation rules $[a_k, a_{k'}] = [b_k, b_{k'}] = \delta_{kk'}$, if acting on the ground state of a filled Fermi sea below $p = 0$. The dynamics of these excitations follows from the commutation rules of the Hamiltonian (2.50) with $\rho(k)$ and $\sigma(k)$ and a bosonized form

$$H_0^B = \hbar v_F \sum_{k>0} k(a_k^\dagger a_k + b_k^\dagger b_k) \tag{2.55}$$

for the free Hamiltonian yields the same dynamics as (2.50). Thus, the non-interacting electron gas has been replaced by its Bose-like charge- and spin-density excitations around the Fermi surface. Moreover the coupling term $J_{||}\sigma_z$ and the mixed products $c_\downarrow^\dagger c_\uparrow$ and $c_\uparrow^\dagger c_\downarrow$ that occur in the spin-flip scattering term of the

anisotropic Hamiltonian (2.51) are related to appropriately chosen bosonic operators, see [83] for details. Then the anisotropic Kondo Hamiltonian (2.51) becomes equivalent to a bosonic Hamiltonian

$$H_K^B = \hbar v_F \sum_{k>0} k a_k^\dagger a_k + \frac{J_{||}}{4}\sigma_z \sum_{k>0} e^{-ak/2}\sqrt{\frac{k}{\pi L}}(a_k + a_k^\dagger) + \frac{J_\perp}{4\pi a}(\sigma_+ e^{\xi} + \sigma_- e^{-\xi})\,, \quad (2.56)$$

with

$$\xi = \sum_{k>0} e^{-ak/2}\sqrt{\frac{4\pi}{kL}}(a_k - a_k^\dagger)\,. \quad (2.57)$$

The essential argument why the behavior of the spin degree of freedom in the Kondo Hamiltonian (2.51) and its bosonized form are the same at low temperatures in the long-time limit $t \gg \omega_c^{-1}$ is based on the following [83, 93]: The dynamics of the Bose operators that multiply the spin variables in eq. (2.56) generated by $H_0^B = \hbar v_F \sum_{k>0} k a_k^\dagger a_k$ is the same as that of the Fermi operators generated by the Hamiltonian (2.50), provided everything is computed in their respective non-interacting groundstates and the long-time limit $t \gg \omega_c^{-1}$ of the bath autocorrelation functions is used. Consequently the equivalence holds at $T = 0$ and in the so-called Fermi-liquid regime of the Kondo problem, where only the low lying excitations above the groundstate are relevant.

The Hamiltonian (2.56) may now be mapped exactly on the Hamiltonian of an Ohmic TLS. The canonical transformation $S^{-1}H_K^B S$ with $S = \exp(\frac{1}{2}\sigma_z \xi)$ yields

$$S^{-1}H_K^B S = \frac{J_\perp}{4\pi a}\sigma_x + \left(\frac{J_{||}}{4} - \hbar v_F\right)\sigma_z \sum_{k>0} e^{-ak/2}\sqrt{\frac{k}{\pi L}}(a_k + a_k^\dagger) + \hbar v_F \sum_{k>0} k a_k^\dagger a_k\,. \quad (2.58)$$

Identifying

$$-\frac{1}{2}\hbar\Delta = \frac{J_\perp}{4\pi a} \qquad \text{and} \qquad -\sqrt{\alpha} = \frac{J_{||}}{4\pi\hbar v_F} - 1 \quad (2.59)$$

the Hamiltonian (2.58) is identical to the spin-boson Hamiltonian (2.25), with

$$J(\omega) = \frac{2\pi\hbar\alpha}{q_0^2}\omega e^{-\omega/\omega_c} \qquad \text{for} \qquad \sum_\alpha \to \sum_{k>0}\,. \quad (2.60)$$

Moreover, $\omega_k = v_F k$ and for the coupling constants and oscillator masses one has the particular choice [83]

$$\frac{c_\alpha}{\sqrt{m_\alpha}} = -\sqrt{\alpha}\frac{2}{q_0}\sqrt{\frac{2\pi\hbar v_F}{L}}\omega_\alpha e^{-\omega/2\omega_c}\,. \quad (2.61)$$

Since the sign of $J_\perp$ is irrelevant the equivalence between the Hamiltonians may be expressed in dimensionless quantities by

$$\frac{\Delta}{\omega_c} = \rho J_\perp \qquad \text{and} \qquad \alpha = (1 - \frac{1}{2}\rho J_{||})^2\,. \quad (2.62)$$

Thus, one has arrived at an equivalence between the Kondo problem and the Ohmic TLS, where the oscillators of the spin-boson model play the role of the spin excitations within the Kondo problem. The dimensionless tunneling amplitude Δ/ω_c corresponds directly to the spin-flip exchange constant $\rho J_\perp$, which is assumed to be small compared to one in both models. However, the coupling constant α related to $\rho J_{||}$ may take arbitrary values, whereas in a proper isotropic Kondo model $\rho J_\perp$ and $\rho J_{||}$ have to be equal and small which implies α near one.

Chapter 3

Phonon-induced decoherence and dissipation in donor-based charge qubits

3.1 Introduction

We investigate the phonon-induced decoherence and dissipation in a donor-based charge quantum bit realized by the orbital states of an electron shared by two dopant ions which are implanted in a silicon host crystal. The dopant ions are taken from the group-V elements Bi, As, P, Sb. The excess electron is coupled to deformation potential acoustic phonons which dominate in the Si host. The particular geometry tailors a non-monotonous frequency distribution of the phonon modes. We determine the exact qubit dynamics under the influence of the phonons by employing the numerically exact quasi-adiabatic propagator path integral scheme thereby taking into account all bath-induced correlations. In particular, we have improved the scheme by completely eliminating the Trotter discretization error by a Hirsch-Fye extrapolation. By comparing the exact results to those of a Born-Markov approximation we find that the latter yields appropriate estimates for the decoherence and relaxation rates. However, noticeable quantitative corrections due to non-Markovian contributions appear.

The presented set-up is related to a double-quantum dot charge qubit realized in a GaAs semiconductor [17], where the geometrical constraints induce charge qubit oscillations with noticeable non-Markovian corrections due to the particularly shaped phonon environment. While piezoelectric phonons dominate in GaAs, we have to consider here the dominating deformation potential electron-phonon coupling since the Si crystal displays inversion symmetry. This chapter is also part of the PhD thesis [94], however, the author of the thesis at hand gave the main contributions.

3.2 The model

To study the influence of the phonons on decoherence and dissipation, we assume that the charge qubit is isolated from any leads. It is formed by a pair of donor atoms embedded in a silicon substrate, which share a single excess electron [3,4]. To be specific, we consider the situation of one donor being a phosphorus atom while the second one is an individual donor atom X chosen from the group $X \in \{$Bi, As, P, Sb$\}$ [7]. Then, the two logic states $|0\rangle, |1\rangle$ of the charge qubit are defined by the electron residing either at donor 1 or 2, respectively. The total Hamiltonian is given in terms of the standard spin-boson model [11, 83] (see section 2.4 for details)

$$H = H_S + H_B + H_{SB}\,, \tag{3.1}$$

where H_S is the two-state Hamiltonian for the charge qubit, H_B models the phonon bath and H_{SB} includes the electron-phonon coupling.

3.2.1 Model for the charge qubit

We represent the Hamiltonian of the charge qubit in the basis of the two localized electronic states denoted as $|L\rangle \equiv |0\rangle$ and $|R\rangle \equiv |1\rangle$, each being the $1s$ orbital of the left/right donor atom, the latter being placed at the origin and at the position $d\mathbf{e}_y$, see fig. 3.1 for a sketch of the geometry. The localized orbital belonging to the right (left) donor is fully described by the position vector of the electron, i.e., $\mathbf{r}_L = \mathbf{r}$ and $\mathbf{r}_R = \mathbf{r} + d\mathbf{e}_y$, respectively. In addition, we allow for an external constant energy bias ϵ which for instance could be due to a nearby capacitive gate. In terms of the Pauli spin matrices σ_i, the two-state Hamiltonian then reads

$$H_S = \hbar\Delta\sigma_x + \hbar\epsilon\sigma_z\,. \tag{3.2}$$

The two lowest lying energy eigenstates $|E^{\pm}\rangle$ at $\epsilon = 0$ are given as an (anti-)symmetric superposition of the localized states $|L\rangle$ and $|R\rangle$ such that $|E^{\pm}\rangle = (|L\rangle \pm |R\rangle)/\sqrt{2}$ with energies $E_{\pm} = \mp\Delta/2$. The tunneling amplitude then follows as $\Delta = E_+ - E_-$ and is a function of the donor distance d.

In order to determine the tunneling amplitude Δ, we have to calculate approximate eigenvalues of the lowest symmetric and antisymmetric energy-eigenstate. In principle, rather highly elaborated methods are available for their calculation, including the anisotropic conduction band dispersion of silicon, the valley orbit interaction and valley interference effects [7, 95]. The latter leads to an oscillatory behavior of the tunneling amplitude Δ for increasing the donor distance d. Noticeably, the oscillations are weak if the two donors are placed in the [100]-plane of the Si host [7]. However, we aim for a detailed and quantitative understanding of the electron-phonon decoherence mechanism and thus resort to the simplest straightforward procedure to determine the tunneling amplitude which is the well established linear combination of atomic orbitals (LCAO) [3, 96]. This tight-binding method is very successful for determining the molecular orbitals for the H_2^+-molecule but

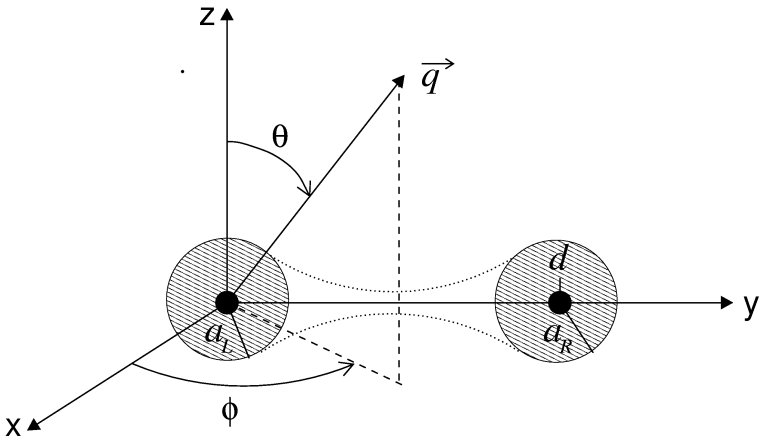

Figure 3.1: Sketch of the geometry of a donor-based charge qubit formed two donor atoms at a distance d and the various angles of the phonon propagation.

can easily be generalized to our model by introducing an effective Bohr radius [97]. When we neglect the conduction-band anisotropy, we can assume that the localized states $|\xi\rangle$ ($\xi = L, R$) are represented by the $1s$ orbital of each donor. They read

$$\langle \vec{r}|\xi\rangle = \sqrt{\frac{1}{\pi a_\xi^3}} e^{-r_\xi/a_\xi} \tag{3.3}$$

where a_ξ is the effective Bohr-radius of the donor ξ [97] and $r_\xi = |\mathbf{r}_\xi|$. In the following, the left donor is assumed to be the phosphorus atom, whereas the right donor is taken from the group-V donors {Bi, As, P, Sb}. Hence, we introduce the ratio p such that $a_R = pa_L$.

To calculate the energy levels an ansatz for the wave function for the (anti-)symmetric ($\mp$) part is made and the overlap between the two wave functions is calculated, yielding the energies for the (anti-)symmetric state. If energies are scaled in atomic units, they read [96]

$$E_\pm = E_1^{(\pm)}(d) + E_2^{(\pm)}(d)\,. \tag{3.4}$$

Here, $E_1^{(\pm)}(d)$ is the kinetic energy and $E_2^{(\pm)}(d)$ is the potential energy, both being functions of the (dimensionless) donor distance d. They read

$$\begin{aligned} E_1^{(\pm)}(d) &= \frac{1 \pm e^{-d}(1 + d - d^2/3)}{1 \pm e^{-d}(1 + d + d^2/3)} \\ E_2^{(\pm)}(d) &= -2\frac{1 \pm 2\,e^{-d}(1+d) + (1/d) - (1/d+1)\,e^{-2d}}{1 \pm e^{-d}(1 + d + d^2/3)}\,. \end{aligned} \tag{3.5}$$

Due to the fixed positions of the donors, there is no need to minimize the energy with respect to the donor distance, in contrast to analogous calculations for the H_2^+-molecule. According to the LCAO calculations typical tunneling amplitudes for a distance of $d = 7.06$ nm (which corresponds to a separation of the two dopants by $n = 13$ lattice sites) follow as $\Delta \approx 16$ meV. This is qualitatively consistent with the results obtained from a more refined approach taking into account interference effects in the Si band structure [7].

3.2.2 Coupling to linear acoustic phonons

The phonon bath is due to the silicon host crystal and is modeled as usual in terms of the bosonic operators $b_{\mathbf{q}}$ as

$$H_B = \hbar \sum_{\mathbf{q}} \omega_{\mathbf{q}} b_{\mathbf{q}}^\dagger b_{\mathbf{q}} \,, \tag{3.6}$$

with the phonon dispersion relation $\omega_{\mathbf{q}}$. The electron-phonon interaction reads [98, 99]

$$H_{SB} = \hbar \sum_{\mathbf{q}} (\alpha_{\mathbf{q}}^L N_L + \alpha_{\mathbf{q}}^R N_R)(b_{\mathbf{q}}^\dagger + b_{-\mathbf{q}}) \,. \tag{3.7}$$

Here, $N_\xi = 0, 1$ is the number of the excess electrons on the donor ξ, respectively, and $\alpha_{\mathbf{q}}^\xi = \lambda_{\mathbf{q}} e^{-i\mathbf{q}\cdot\mathbf{r}_\xi} F_\xi(\mathbf{q})$. The coupling constant $\lambda_{\mathbf{q}}$ depending on the wave vector $\mathbf{q}$ is specified below. Note that the phonons can propagate in all three dimensions, and the electron-phonon coupling is not isotropic in general [100]. To take care of the charge distribution in each donor we define a form factor according to

$$F_\xi(\mathbf{q}) = \int d^3r \, n_\xi(\mathbf{r}) e^{-i\mathbf{q}\cdot\mathbf{r}} \,, \tag{3.8}$$

where $n_\xi(\mathbf{r})$ is the charge density of the donor ξ. The coupling Hamiltonian is rewritten in the form [99]

$$H_{SB} = \frac{\hbar}{2} \sigma_z \sum_{\mathbf{q}} g_{\mathbf{q}} (b_{\mathbf{q}}^\dagger + b_{-\mathbf{q}}) \,, \tag{3.9}$$

with $g_{\mathbf{q}} = [\lambda_{\mathbf{q}}(F_L(\mathbf{q}) - F_R(\mathbf{q}))]$. The charge density distribution then follows directly from eq. (3.3) as $n_\xi(\mathbf{r}) = |\langle \mathbf{r}|\xi\rangle|^2$, which leads to the form factors $F_L(\mathbf{q}) = f_L(\mathbf{q})$ and $F_R(\mathbf{q}) = f_R(\mathbf{q}) e^{-i\mathbf{q}\cdot d\mathbf{e}_y}$ with $f_\xi(\mathbf{q}) = 16/[4 + (qa_\xi)^2]^2$.

In this work we focus on linear acoustic phonons with linear dispersion relation $\omega_{\mathbf{q}} = s|\mathbf{q}|$, s being the sound velocity for silicon ($s \approx 9 \times 10^3\,\mathrm{m/s}$) [101]. Since the silicon crystal has an inversion center there is no piezoelectric coupling between electrons and phonons, wherefore the dominating coupling is due to the deformation potential. Thus, the coupling constant reads

$$\lambda_{\mathbf{q}} = \frac{D}{\hbar} q \sqrt{\frac{\hbar}{2\rho_m V \omega_{\mathbf{q}}}} \,, \tag{3.10}$$

where D is the deformation constant for silicon ($D \approx 8.6\,\mathrm{eV}$, see Ref. [102]), ρ_m is the mass density of silicon ($\rho_m \approx 2.33 \times 10^3\,\mathrm{kg\ m^{-3}}$, see Ref. [101]) and V is the volume of the unit cell.

All the properties of the phonon bath can be captured in the spectral density defined as

$$G(\omega) = \sum_{\mathbf{q}} |g_{\mathbf{q}}|^2 \delta(\omega - \omega_{\mathbf{q}})\,. \tag{3.11}$$

Using eq. (3.10) and the definition of the form factors and taking into account the geometry, the sum over $\mathbf{q}$ can be transformed into a continuous integral which can readily be carried out. One then obtains the spectral density

$$\begin{aligned} G(\omega) &= \frac{64D^2}{\pi^2\rho_m\hbar s^5}\omega^3 \left[\left(4+\left(\frac{\omega}{s}a_L\right)^2\right)^{-4} + \left(4+\left(\frac{\omega}{s}pa_L\right)^2\right)^{-4}\right. \\ &\quad \left. -2\left(4+\left(\frac{\omega}{s}a_L\right)^2\right)^{-2}\left(4+\left(\frac{\omega}{s}pa_L\right)^2\right)^{-2} j_0\left(\frac{\omega}{s}d\right)\right]. \end{aligned} \tag{3.12}$$

where j_0 is the spherical Bessel function. The spectral density is sketched in the inset of fig. 3.2. The low-frequency behavior is superohmic according to $G(\omega \to 0) \propto \omega^3$, while in the high-frequency limit, it decays algebraically as $G(\omega \to \infty) \propto \omega^{-5}$. The crossover between these two limits occurs on a frequency scale $\omega_c = s/a_P \equiv \tau_c^{-1}$, where a_P is the radius of the phosphorus donor ($a_P = 1.22\,\mathrm{nm}$, see [97]), yielding $\omega_c = 2.46\,\mathrm{THz}$, which corresponds to an energy of $10.17\,\mathrm{meV}$. As we will see below, typical tunneling amplitudes Δ are comparable to this energy scale. Thus, the frequency distribution of the bath is no longer monotonous in the range of the relevant system energies. As common approximate analytical treatments [3, 11] of phonon-induced decoherence typically involve a smooth frequency distribution, it is not *a priori* clear whether their results are applicable to this situation. Moreover, the used Born-Markovian approximation which neglects bath-induced correlations might not describe properly the dynamics. This can be seen from the autocorrelation function [11] of the bath, eq. (2.18) which is shown in fig. 3.2. The typical width of the correlation function is comparable to the time scale $\Delta^{-1} \approx \omega_c^{-1}$ of the system dynamics.

The Born-Markov approximation corresponds to replacing the strongly peaked real part $L_R(t)$ by a δ-function with the corresponding weight while the imaginary part $L_I(t)$ is often neglected. However, since the geometry tailors a specific structured phonon environment for the charge qubit, it is not clear from the very beginning that the Markovian assumption is valid. It is the main purpose of the present chapter to investigate this issue and compare exact real-time path integral simulations with approximate weak-coupling (Born-Markov) results.

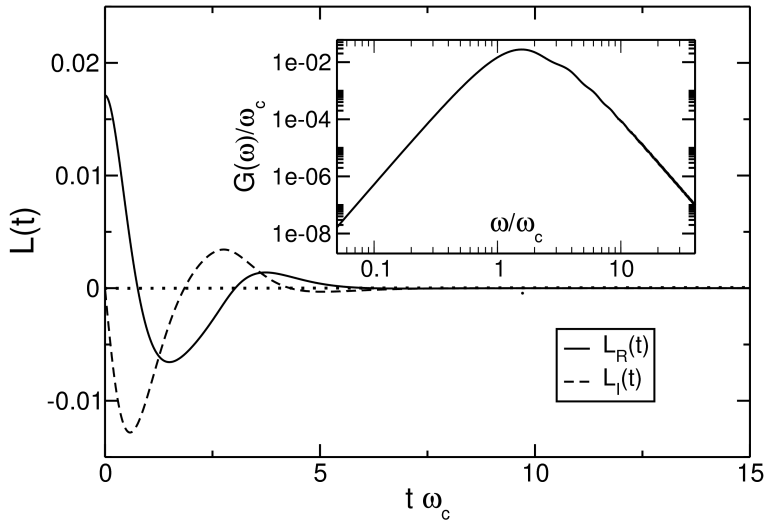

Figure 3.2: The bath autocorrelation function (response function) $L(t) = L_R(t) + iL_I(t)$ for the spectral density $G(\omega)$ (inset) of the phonon bath for the case of two P donors in a Si host ($p = 1$, deformation potential phonons), with $s = 9 \times 10^3$ m/s, an effective Bohr radius of $a_P = 1.22$ nm, and inter-donor distance $d = 10.32$ nm. The temperature is $T = 50$ mK.

3.3 The QUAPI scheme

In order to investigate the dynamics of the system, we use the quasi-adiabatic propagator path integral (QUAPI) scheme [8] being a numerically exact iteration scheme which has been successfully adopted to many problems of open quantum systems [9, 17]. Since we will also make use of this method in the chapters 4 and 5 we introduce it here in quite some detail.

The dynamics of the system of interest is described in terms of the time evolution of the reduced density matrix $\rho(t)$, introduced in eq. (2.29), which is obtained after tracing out the bath degrees of freedom, hence

$$\begin{aligned} \rho(t) &= \mathrm{tr}_B K(t,0) W(0) K^{-1}(t,0)\,, \\ K(t,0) &= \mathcal{T} \exp\left\{ -\frac{i}{\hbar} \int_0^t dt' H \right\}\,. \end{aligned} \tag{3.13}$$

$K(t,0)$ denotes the propagator of the full system plus bath, $\mathcal{T}$ is the time ordering operator and H is the Hamiltonian, eq. (3.1). The full density operator $W(0)$ at initial time $t = 0$ is as usual assumed factorizing, see section 2.5.1. The staring point for developing the algorithm is to discretize the path integral in eq. (3.13) into N steps of length Δt. Next, the full propagator over a single time step is broken into a part belonging to the system and a part depending on the environmental degrees of freedom and the coupling between system and environment. Here, one makes use

of the symmetric Trotter formula [103] which leads to

$$\begin{aligned} K(t_{k+1},t_k) &\approx \exp(-iH_{SB}\Delta t/2\hbar)K_S(t_{k+1},t_k)\exp(-iH_{SB}\Delta t/2\hbar) \\ K_S(t_{k+1},t_k) &= \mathcal{T}\exp\left\{-\frac{i}{\hbar}\int_{t_k}^{t_{k+1}} dt'\, H_S(t')\right\}, \end{aligned} \tag{3.14}$$

where $\mathcal{T}$ denotes the chronological operator. Since both parts of the Hamiltonian do not commute, as $H_{SB} \sim q$ and $H_S \sim p$, the splitting in eq. (3.14) induces an error proportional to $[H_{SB},[H_S,H_{SB}]]\,\Delta t^3$ [10]. The short time propagator of the bare system $K_S(t_{k+1},t_k)$ is calculated by means of the Schrödinger equation which is solved numerically within a fourth-order Runge-Kutta scheme with adaptive stepsize control. We may express the short time propagator in coordinate representation as

$$\begin{aligned} &\langle q\Pi_\alpha x_\alpha|K(t_{k+1},t_k)|q'\Pi_\alpha x'_\alpha\rangle \approx \\ &\langle q|K_{\rm s}(t_{k+1},t_k)|q'\rangle \prod_{\alpha=1}^{N}\langle x_\alpha|\exp(-iH_\alpha(q)\Delta t/2\hbar)\exp(-iH_\alpha(q')\Delta t/2\hbar)|x'_\alpha\rangle\,, \end{aligned} \tag{3.15}$$

where H_α is the Hamiltonian of the single bath oscillator, eq. (3.6). Eq. (3.15) constitutes the quasi-adiabatic propagator, since the position operator q of the bath part of the Trotter splitting in eq. (3.14) is treated as a parameter which yields the factorizing total short time propagator (3.15). The equilibrium positions of the bath oscillators are adiabatically displaced along the system coordinate q and the potential along this adiabatic path $x_\alpha = \frac{c_\alpha}{m_\alpha\omega_\alpha^2}q$ is comprised in the system Hamiltonian (3.2). Along this path the full system has minimal potential energy for a fixed coordinate q and the single bath oscillators are centered at the point of minimal potential energy. Including this assumption we again recover the reduced density matrix (2.29) with a discretized version of the Feynman-Vernon influence functional

$$\begin{aligned} \rho(q_f,q'_f;t) &= \int dq_0\ldots dq_N\int dq'_0\ldots dq'_N\delta(q'_f-q'_N)\delta(q_f-q_N) \\ &\quad\times\langle q_f|K_{\rm s}(t,t-\Delta t)|q_{N-1}\rangle\,\ldots\langle q_1|K_{\rm s}(t_0+\Delta t,t_0)|q_0\rangle\,\langle q_0|\rho_{\rm s}(t_0)|q'_0\rangle \\ &\quad\times\langle q'_0|K_S(t_0+\Delta t,t_0)|q'_1\rangle\cdots\langle q'_{N-1}|K_S(t,t-\Delta t)|q'_N\rangle \\ &\quad\times\mathcal{F}_{FV}^{(N)}(q_0,q'_0,\ldots,q_N,q'_N)\,. \end{aligned} \tag{3.16}$$

Here the paths $q(t')$ and $q'(t')$ are composed of equidistant segments q_k and q'_k respectively within each time interval $t_k-\frac{\Delta t}{2} < t_k < t_k+\frac{\Delta t}{2}$. These composed paths allow for rewriting the influence functional as

$$\mathcal{F}_{FV}^{(N)}(q_0,q'_0,\cdots,q_f,q'_f) = \exp\left\{-\frac{1}{\hbar}\sum_{k=0}^{N}\sum_{k'=0}^{k}[q_k-q'_k]\,[\eta_{kk'}q_{k'}-\eta^*_{kk'}q'_{k'}]\right\}. \tag{3.17}$$

and the coefficients $\eta_{kk'} \equiv \eta(t_k-t'_k)$ are related to their continuous counterpart and are calculated exactly [104]. Eq. (3.16) has been successfully adopted to describe the short time dynamics of relevant systems [8].

To describe the long time dynamics we are interested in, too many quadrature points would be needed to evaluate the underlying path integral directly. A way out is to compute the reduced density matrix in an iterative way. Therefore, the discretized influence kernel $\mathcal{F}_{FV}^{(N)}(q_0, q_0', \cdots, q_f, q_f')$ is broken into smaller pieces on each time slice

$$\begin{aligned}\mathcal{F}(q_0, q_0', \cdots, q_f, q_f') &= \prod_{k=0}^{N} \mathcal{F}_0(q_k^{\pm}) \ldots \prod_{k=0}^{N-1} \mathcal{F}_1(q_k^{\pm}, q_{k+1}^{\pm}) \ldots \prod_{k=0}^{N-\Delta k} \mathcal{F}_{\Delta k}(q_k^{\pm}, q_{k+\Delta k}^{\pm}) \\ &\ldots \times \prod_{k=0}^{N-K} \mathcal{F}_K(q_k^{\pm}, q_{k+K}^{\pm}), \qquad q = q^+, q' = q^- \end{aligned} \tag{3.18}$$

where we have introduced q^+ and q^- for notational convenience and for later purpose. The parts contributing to the influence functional in eq. (3.18) are depicted in fig. 3.3. The self-interaction reads

$$\mathcal{F}_0(q_k^{\pm}) = \exp\left\{-\frac{1}{\hbar}\left[q_k^+ - q_k^-\right]\left[\eta_{kk} q_k^+ - \eta_{kk}^* q_k^-\right]\right\} \tag{3.19}$$

and the interaction between different path segments is of the form

$$\mathcal{F}_{\Delta k}(q_k^{\pm}, q_{k+\Delta k}^{\pm}) = \exp\left\{-\frac{1}{\hbar}\left[q_{k+\Delta k}^+ - q_{k+\Delta k}^-\right]\left[\eta_{k,k+\Delta k} q_k^+ - \eta_{k,k+\Delta k}^* q_k^-\right]\right\}. \tag{3.20}$$

The $\mathcal{F}_{\Delta k}$ are the memory slices that are taken into account within the method, since the bath-induced correlations being non-local in time are included in the numerical scheme over a finite memory time $\tau_{mem} = K\Delta t$. This corresponds roughly to the time range over which the bath autocorrelation function $L(t)$ given in eq. (2.18) is significantly different from zero. For any finite temperature $L(t)$ decays exponentially at long times [11] justifying this approach. Note that this is completely analogous to what is done within the newly developed ISPI approach for a system within a fermionic environment, see chapter 6. For the influence functional this implies that the memory function $\eta(t)$ is truncated after after K time steps, thus $\eta_{kk'}$ is neglected if $k' > k + K$. Then the influence functional is rewritten in compact form as

$$\mathcal{F}_{FV}^{(N)}(q_0, q_0', \cdots, q_f, q_f') = \prod_{k=0}^{N} \prod_{k'=0}^{\min\{N,K\}} \exp\left\{-\frac{1}{\hbar}\left[q_k^+ - q_k^-\right]\left[\eta_{kk'} q_{k'}^+ - \eta_{kk'}^* q_{k'}^-\right]\right\}. \tag{3.21}$$

Eq. (3.21) illustrates nicely that the path in q is equivalent to the Keldysh contour used in chapter 6 to describe non-equilibrium transport to an Anderson impurity. For details of the Keldysh technique, see section 6.1.1. The q^+ and q^- reside on the upper and lower contour, respectively, see fig. 3.4. This demonstrates the strong connection between the QUAPI scheme and the ISPI method, although there are conceptual differences, discussed in detail in chapter 6.

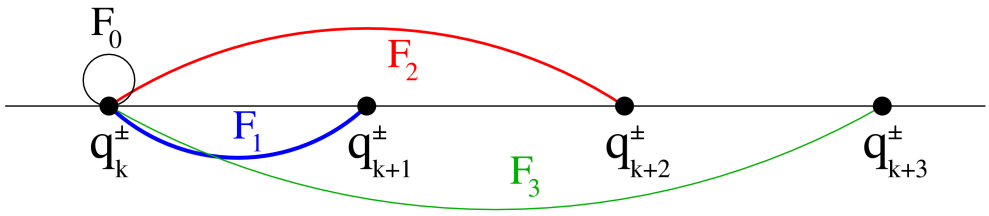

Figure 3.3: Illustration of the parts contributing to the broken influence functional on a single time slice. $\mathcal{F}_0$ is the self-interaction, and the $\mathcal{F}_{\Delta k}$ constitute the interaction between different path segments.

Inserting the truncated influence functional into the reduced density matrix (3.16) yields

$$\rho(q_f, q_f'; t) = A_N(q_f, q_f', \hat{q}, \ldots, \hat{q}) \exp\left\{-\frac{1}{\hbar}\left[q_f^+ - q_f^-\right]\left[\eta_{NN} q_f^+ - \eta_{NN}^* q_f^-\right]\right\} \tag{3.22}$$

and since the bath oscillators are adiabatically displaced along q, $\widehat{q}$ is arbitrary but fixed. A_k is the reduced density tensor that depends on the $2K$ arguments $q_k^+, q_k^-, \cdots, q_{k+K-1}^+, q_{k+K-1}^-$ and follows from the recursion relation

$$A_{k+1}(q_{k+1}^\pm, \ldots, q_{k+K}^\pm) = \int dq_k^+\, dq_k^-\, \Lambda_k(q_k^\pm, \ldots, q_{k+K}^\pm) A_k(q_k^\pm, \ldots, q_{k+K-1}^\pm)\,. \tag{3.23}$$

Here,

$$\begin{aligned} \Lambda_k(q_k^\pm, \ldots, q_{k+K}^\pm) &= \left\langle q_{k+1}^+ | K_S(t_{k+1}, t_k) | q_k^+ \right\rangle \left\langle q_k^- \left| K_S^{-1}(t_{k+1}, t_k) \right| q_{k+1}^- \right\rangle \\ &\times \prod_{k'=0}^{K} \exp\left\{-\frac{1}{\hbar}\left[q_k^+ - q_k^-\right]\left[\eta_{kk'} q_{k'}^+ - \eta_{kk'}^* q_{k'}^-\right]\right\} \end{aligned} \tag{3.24}$$

is the propagator tensor with the initial condition

$$A_0(q_0^\pm, \ldots, q_{K-1}^\pm) = \left\langle q_0^+ | \rho_S(t_0) | q_0^- \right\rangle\,. \tag{3.25}$$

Eq. (3.23) together with eq. (3.25) constitutes the name *iterative tensor multiplication scheme* for the method and the notion tensor is used here to emphasize that one is concerned with multi-dimensional arrays, but does not refer to the algebraic properties of a tensor in the mathematical sense.

Up to now the reduced density matrix (3.17) was treated in a spatial continuous way which makes the evaluation of the recursion relation (3.23) intractable for relevant systems. To evade this problem a transformation into the energy eigenstates of the bare system Hamiltonian is performed. For a thermal bath the occupation of higher energy states is negligible for low temperatures (see also section 2.4). The dynamics is then projected to a Hilbert subspace spanned by the eigenstates $|m\rangle, m = 1, \cdots M$ which corresponds to an approximate decomposition of

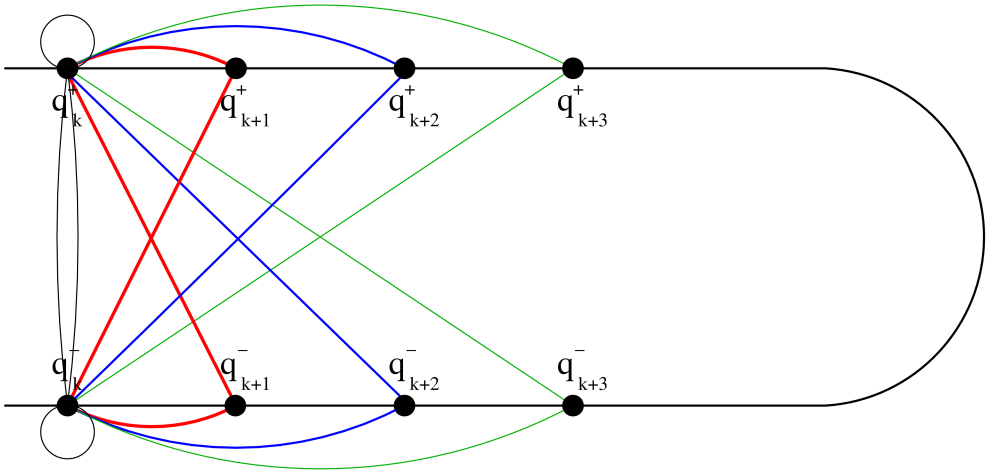

Figure 3.4: Same as fig. 3.3 but now q^+ and q^- are explicitly shown on the upper and lower part of the contour. This depicts the connection to the Keldysh approach, see sec. 6.1.1.

the identity operator $\mathbb{1} \approx \sum_{m=1}^{M} |m\rangle\langle m|$. To obtain the final recursion relation the position operator is unitarily transformed such that it becomes diagonal in the M-dimensional Hilbert subspace. This is the so-called discrete variable representation (DVR) which follows from

$$|u_m\rangle = \sum_{m'=1}^{M} R_{m,m'} \, |m'\rangle \,, \quad \langle u_m|q|u_{m'}\rangle = q_m^{DVR}\delta_{mm'}, \quad m, m' = 1, \ldots, M \quad . \tag{3.26}$$

The states $|u_m\rangle$ are localized in position space at the eigenvalues q_m^{DVR} of the position operator and $R_{m,n'}$ denotes the diagonalization of the position operator. The truncated reduced density matrix (3.22) and the eqs. (3.23-3.23) are then modified according to the DVR transformation and since the integrals within the reduced density tensor (3.23) are changed into finite sums the iterative summation of the path histories is now numerically tractable.

However, we have improved the method at one important step and we will describe this in greater detail next. As mentioned above the QUAPI algorithm is based on a symmetric Trotter splitting of the short-time propagator $K(t_{k+1}, t_k)$ of the full system into a part depending on H_S and $H_B + H_{SB}$ describing the time evolution on a time slice Δt. This is exact in the limit $\Delta t \to 0$ but introduces a finite Trotter error to the propagation which has to be eliminated by choosing Δt small enough that convergence has been achieved. On the other side, the bath-induced correlations being non-local in time are included in the numerical scheme over a finite memory time $\tau_{mem} = K\Delta t$ which roughly corresponds to the time range over which the bath autocorrelation function $L(t)$ given in eq. (2.18) is significantly different from zero. Note that for any finite temperature $L(t)$ decays exponentially at long times [11] justifying this approach.

To obtain convergence with respect to the memory time, K has to be increased until converged results have been found. However, the numerical effort grows exponentially with the memory length K and for the present two-level system, the memory length is restricted to typical values of $K = 12$ on a standard processor with 2 GB RAM for practical reasons.

Thus, the two strategies to achieve convergence are countercurrent. To solve this, the principle of least dependence has been invoked [9] to find an optimal time increment in between the two limits. We will make use of this in the chapters 4 and 5. However, here we show that the algorithm can be improved by applying a different strategy.

We first choose some small enough time increment Δt. Then, one has to increase the memory time τ_{mem} by increasing K until convergence has been achieved. Typical results of this memory convergence check are shown in fig. 3.5. Shown is the decoherence rate γ for increasing memory time for different donor distances ($p = 1$) for the symmetric qubit $\epsilon = 0$. Note that the decay rate has been obtained by fitting the results for the population difference $P(t) = \langle \sigma_z \rangle_t$ to an exponentially decaying cosine. The remaining error is the Trotter error. However, following [10], for any Hermitian observable, this symmetric Trotter error vanishes quadratically in the limit $\Delta t \to 0$. This opens the possibility to extrapolate the results to $\Delta t \to 0$, thereby completely eliminating the Trotter error. This is done by decreasing Δt from the initial value and then by finding the extrapolated exact result (of course, convergence has to be verified again for the smaller values of Δt). Typical results of this extrapolation procedure are shown in fig. 3.6, indicating that the numerical values follow a line for decreasing step sizes. Note that we consider $P(t_{fix})$ at an arbitrary time $t_{fix} = 34.1/\omega_c$ in this example. Indeed, we find the predicted behavior for the Trotter error to vanish and perform a linear regression to $\Delta t \to 0$, also shown in fig. 3.6. The y-axis intersection gives the numerical exact value for the observable of interest, in this case afflicted with a tiny error bar coming from the linear regression. In general, the convergence properties of an observable strongly depend on the involved parameters, similar to path-integral quantum Monte-Carlo simulations [105]. Different observables show different behaviors with decreasing Trotter step size Δt, as for instance the particle density in contrast to the energy of the system in [105].

3.4 The dynamics of the charge qubit

Equipped with the numerically exact improved QUAPI scheme, we can now study the dynamics of the charge qubit in detail. To extract the decoherence rate γ, the relaxation rate γ_r, the equilibrium population difference P_∞ and the oscillation frequency Ω, we fit a combination of exponentially decaying cosine and sine functions [11] to the numerically exact data, from which the Trotter error has been eliminated. We can then investigate the dependence of the above quantities on the experimentally relevant parameters. We emphasize again that realistic assumptions

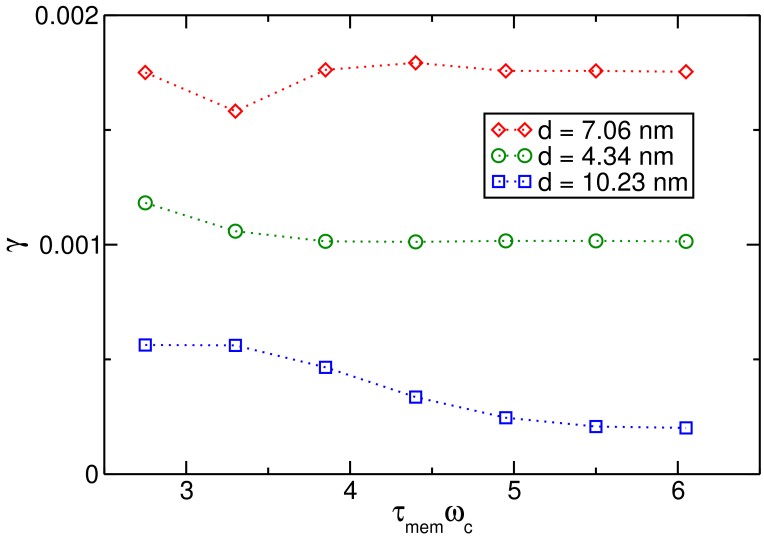

Figure 3.5: Check of convergence with respect to the memory time $\tau_{mem} = K\Delta t$ for the decoherence rate γ (symmetric qubit $\epsilon = 0$) and for the donor distances $d = 4.34\,\mathrm{nm}$, $d = 7.06\,\mathrm{nm}$ and $d = 10.32\,\mathrm{nm}$ and the corresponding tunnel matrix elements obtained from the LCAO. The Trotter time increment is fixed to $\Delta t = 0.55\omega_c$.

on the geometry of the system enter the spectral density eq. (3.12) and thus allow to calculate quantitative realistic results.

One of the major goals of this work is to verify the Born-Markov (weak-coupling) approximation, since the later results in very simple and compact formulas for parameters governing the dynamics. For details of the Born-Markov approximation, see section 2.6. Hence, we compare the exact QUAPI results with results obtained within a WCA which are known as [11]

$$\gamma = \frac{\gamma_r}{2} + \frac{2\pi\epsilon^2}{\Delta_b^2} S(0)\,, \tag{3.27}$$

$$\gamma_r = \frac{\pi\Delta_{\mathrm{eff}}^2}{2\Delta_b^2} S(\Delta_b)\,, \tag{3.28}$$

$$\Omega^2 = 4\Delta_{\mathrm{eff}}^2[1 - 2\,\mathrm{Re}\,u(2i\Delta_b)] + 4\epsilon^2\,, \tag{3.29}$$

$$P_\infty = -\frac{\epsilon}{\Delta_b}\tanh\left(\frac{\hbar\Delta_b\beta}{2}\right)\,. \tag{3.30}$$

The spectral function $S(\omega)$, related to the phonon spectral density, eq. (3.12), via $S(\omega) = G(\omega)\coth(\hbar\omega/(2k_BT))$, represents emission and absorption of a single phonon and $\Delta_b = 2\sqrt{\Delta_{\mathrm{eff}}^2 + \epsilon^2}$ is twice the effective qubit frequency. Δ_{eff} is the effective tunnel matrix element at $T = 0$ [11], which includes the renormalization by a Franck-Condon factor stemming from the high-frequency modes of the reservoir [11]. In the present case, one easily finds that $\Delta_{\mathrm{eff}} \approx \Delta$ with a deviation of less

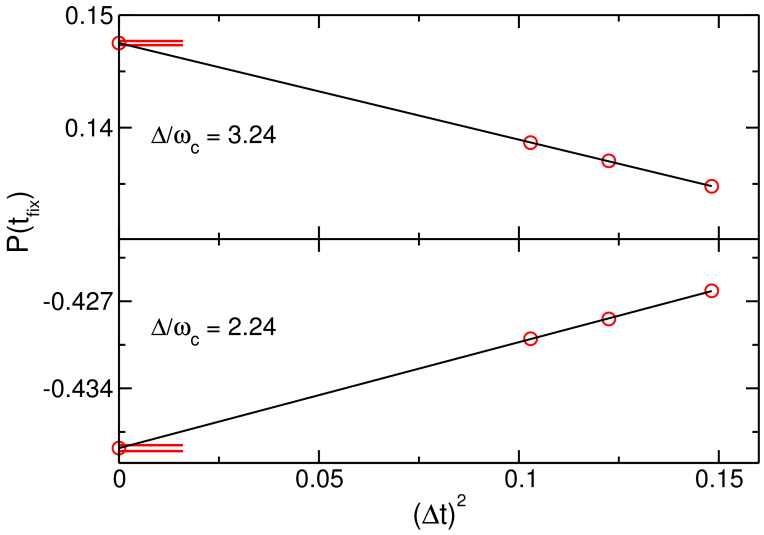

Figure 3.6: Example of the Trotter convergence for the the population difference of the qubit, $P(t_{fix})$, from which the quantities of interest are extracted. In the lower sketch the tunnel amplitude was chosen as $\Delta/\omega_c = 2.24$ and $t_{fix} = 34.1/\omega_c$, and in the upper sketch $\Delta/\omega_c = 3.24$ and $t_{fix} = 18.2/\omega_c$. The memory-time is fixed to $\tau_{mem} = 3.85/\omega_c$ and three values of $K = 10, 11, 12$ have been chosen. At $\tau_{mem}^2/K^2 \to 0$ the value $P(t_{fix})$ is shown as a result of the extrapolation $\Delta t \to 0$, with the error of the linear regression (horizontal bars).

than 1%. The function $u(z)$ is defined in terms of the frequency integral

$$u(z) = \frac{1}{2}\int_0^\infty d\omega \, \frac{G(\omega)}{\omega^2 + z^2}\left(\coth\left(\frac{\hbar\omega}{2k_BT}\right) - 1\right) . \tag{3.31}$$

3.4.1 Coherent charge oscillations for the symmetric qubit $\epsilon = 0$

For the symmetric qubit with zero bias (i.e., only decoherence, no dissipation), we have calculated the time evolution of $P(t)$ and have observed coherent charge oscillations. In order to quantify them, we define the quality factor $Q = \Omega/(\pi\gamma)$ where the frequency Ω and the decoherence rate γ have been been obtained from the fit as described above. We have performed extensive simulations for three different donor distances d for various combinations of donor atom species and show the results as a function of the tunneling amplitude Δ in figs. 3.7, 3.8, and 3.9, each for a fixed donor distance d. A variation of Δ for a fixed donor distance can, for instance, be achieved by a small additional gate voltage which slightly distorts the $1s$ orbitals leading to an increased overlap of the wave functions.

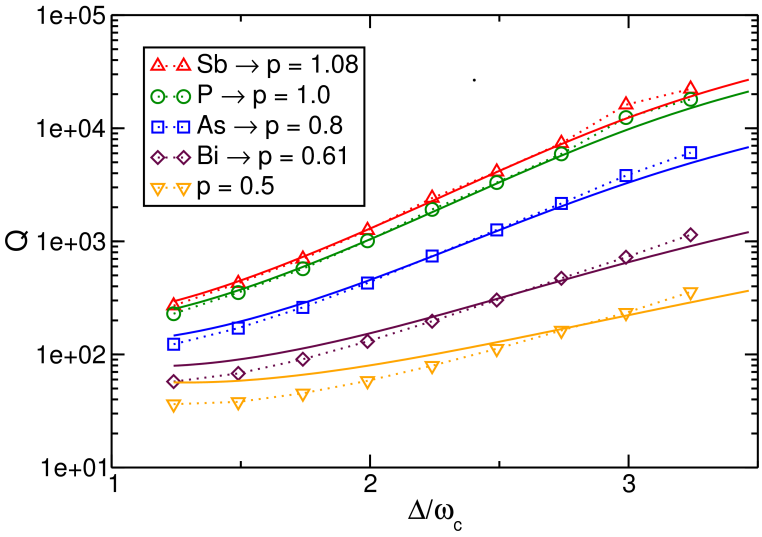

Figure 3.7: Quality factor as a function of the tunneling amplitude Δ for different donor combinations and a small donor distance $d = 4.34\,\mathrm{nm}$. The symbols depict the exact QUAPI results while the solid lines mark the results of the WCA. Temperature is fixed at $T = 50$ mK.

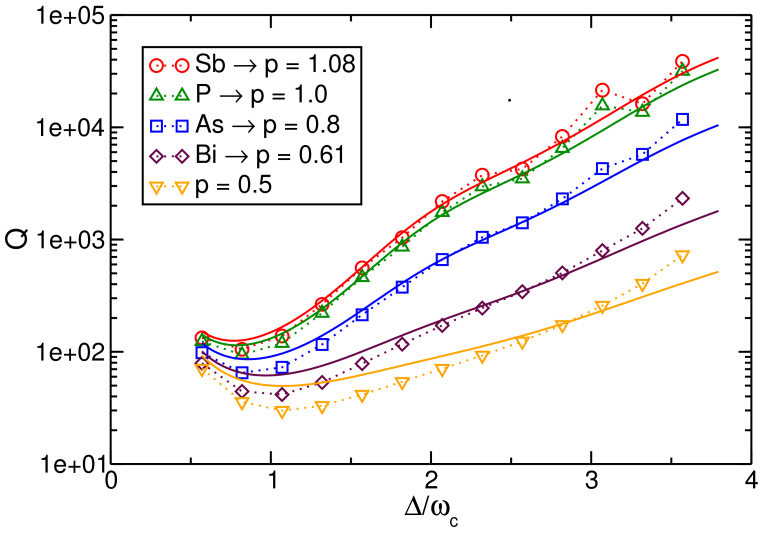

Figure 3.8: Same as fig. 3.7, but for an intermediate donor distance $d = 7.06$ nm.

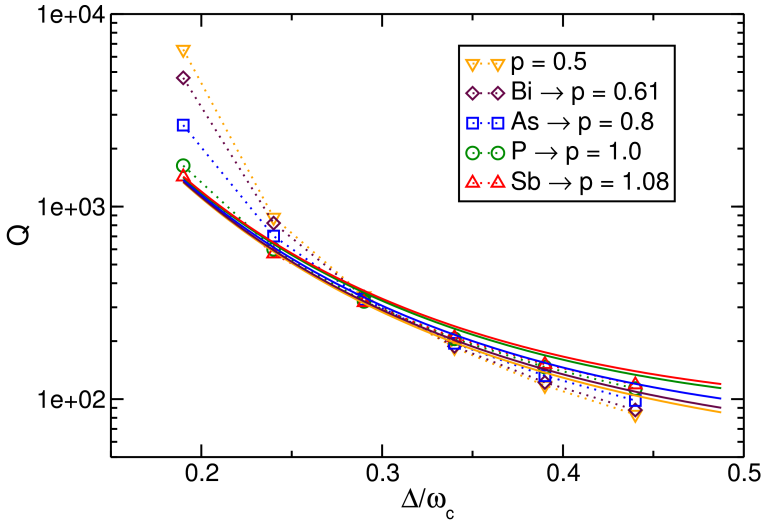

Figure 3.9: Same as fig. 3.7, but for a large donor distance $d = 10.32$ nm.

For the smallest donor distance $d = 4.34$ nm, we observe in fig. 3.7 that Q increases monotonously for increasing Δ. Thereby, the results for Q vary over two orders of magnitude for the different donor species at large Δ. Moreover, the combination of two P donors or of one P and one (very similar) Sb donor displays the best decoherence properties. The dashed lines in fig. 3.7 display the results of the WCA given in eqs. (3.27) and (3.29). A reasonable agreement is found in this case.

For intermediate donor distance $d = 7.06$ nm, see fig. 3.8, Q first decreases but then increases again with increasing Δ. This can be understood by the fact that d determines the shape of the spectral density and, in particular, the location of the frequency of the cross-over, relative to the qubit frequency Δ. For the overall performance, the similar observation as for the smaller distance (see above) apply. Also in this case, the WCA seems to be appropriate although small deviations for all Δ can be observed which can be attributed to small non-Markovian corrections stemming from the specifically tailored phonon environment.

In the case of large donor distance $d = 10.32$ nm, see fig. 3.9 the differences between the various donor species almost vanish and are only noticeable at small Δ. Also the WCA agrees well at large Δ and also yields the correct order of magnitude for small Δ although differences become noticeable in this regime. Note that in this case, Q decreases for increasing Δ, in contrast to the case of small and intermediate distances.

Noticeably, we find that the Q-factor is independent of temperature for all relevant parameter combinations (not shown here). This is due to the fact that realistic temperatures correspond to frequencies of $T = 6.5 \times 10^9$ Hz and hence all system frequencies are much larger. This behavior is in contrast to what we have recently reported in GaAs DQD systems [17].

Note that the oscillatory behavior of Δ for increasing d [7] is not included in this

simple LCAO approximation. However, when considering the $Q-$factor in figs. 3.7, 3.8, and 3.9, the oscillatory behavior of Δ for growing donor distances d does not affect Q substantially. This can be rationalized by considering the weak-coupling results eqs. (3.27)-(3.29) for $\epsilon = 0$. Then, it becomes clear that the only part where $\Delta(d)$ appears is in the high-frequency part of $G(\omega)$ (assuming low temperature such the the coth approaches one and being interested in $\Delta \approx \omega_c$). The prefactors, which in principle contain $\Delta(d)$, drop out when the ratio is calculated.

3.4.2 Dynamics of the biased charge qubit $\epsilon \neq 0$

When a finite bias $\epsilon \neq 0$ is present, in addition to decoherence also relaxation occurs to a non-zero asymptotic value $P_\infty \neq 0$. The corresponding decoherence and relaxation rates are also influenced by the presence of a bias in the sense that the effective qubit frequency Δ_b grows with increasing ϵ. Then, the behavior of the environmental frequency distribution is essential: if it grows with increasing frequency, decoherence and dissipation will become more effective and if it decreases the environmental effects will diminish. This is what we observe from the results shown in fig. 3.10. For comparison, we also show the corresponding WCA results, which yield the qualitatively correct behavior while differences in the quantitative results occur.

3.5 Conclusion

To summarize, we have investigated the phonon-induced decoherence and dissipation in donor-based charge qubits formed by a pair of donor atoms placed in a Si crystal host. The donor pair is formed by one P donor and one donor of the group Bi, As, P, Sb. We have employed the numerically exact quasi-adiabatic path-integral propagator in its iterative version. The major achievements of our work is twofold: (i) We have first improved the QUAPI scheme in the sense that the Trotter discretization error can now be completely eliminated by extrapolating the results to vanishing Trotter increment, as it is known that the error vanishes quadratically. (ii) Beyond these methodical aspects, we have obtained numerically exact results for the real-time dynamics of charge qubits under the influence of acoustic deformation potential phonons. Realistic assumptions on the tunneling amplitude enters via LCAO calculations of the wave functions and the qubit energies in our model. Moreover, we have included the particular phonon environment tailored by the particular geometry of the set-up via geometrical form factors and materials characteristics. No fitting parameters of any sort were utilized.

In the absence of a static bias we have investigated the Q-factor of the charge oscillations as a function of the donor distance and as well as a function of the tunneling amplitude. We have compared our results with those obtained from a WCA within an analytical approach in terms of real-time path-integrals and found that only small non-Markovian corrections appear. This can be attributed to the

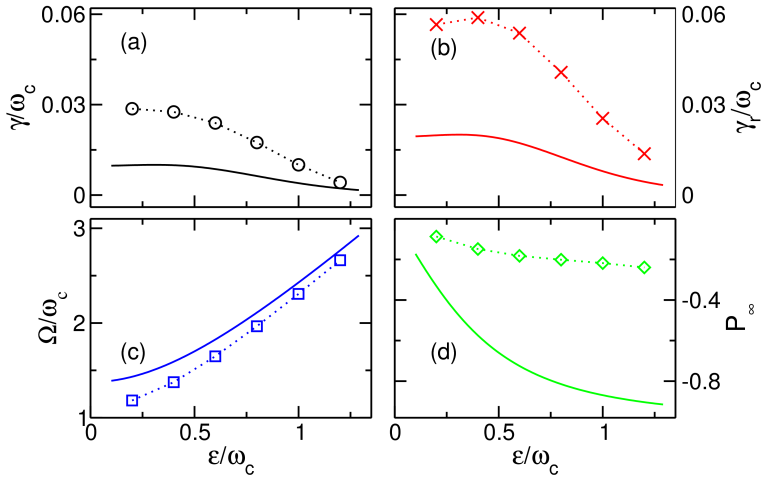

Figure 3.10: Upper panel: Relaxation (γ_r) and decoherence (γ) rate for increasing bias ϵ. Symbols are the exact QUAPI results while the solid lines are the corresponding WCA results. Lower panel: Oscillation frequency Ω and asymptotic value P_∞. The remaining parameters are $d = 7.06$ nm, $\Delta = 0.57\omega_c$, and $T = 50$ mK.

dominating super-Ohmic properties of the phonon environment at small frequencies. Furthermore we have investigated the dynamics in the case of a static bias and have found that the qualitative behavior of the decoherence and damping rates follows the form of the environmental frequency distribution. Non-Markovian corrections are also found in this case.

At present, no experimental realizations of this setup is yet reported. Nevertheless, we emphasize that our results on the decoherence and dissipation induced by the electron-phonon coupling represent a fundamental upper limit to the coherence of such donor based charge qubits which can hardly be negotiated due to its intrinsic nature. This has to be seen in view of the DiVincenzo criteria [106] and also for the future realization of quantum information processes. However, the dominating source of decoherence in this kind of qubit realization has to be investigated in realistic devices.

Chapter 4

Coherent control of an effective two-level system in a non-Markovian biomolecular environment

Within the present chapter we address the question if and to what extent the time period over which quantum coherent dynamics occurs, studied in the preceding chapter, can be extended by an externally applied driving field. In contrast to chapter 3 the model of interest is more general since we focus on an Ohmic environment which is a proper choice for a variety of nanoscale systems. To be specific, we investigate the quantum coherent dynamics of an externally driven effective two-level system subjected to a slow Ohmic environment characteristic of biomolecular protein-solvent reservoirs in photosynthetic light harvesting complexes. By means of the QUAPI method we show the dependence of the quantum coherence on the characteristic bath cut-off frequency ω_c as well as on the driving frequency ω_l and the field amplitude A. Our calculations extend from the weak coupling regime to the incoherent strong coupling regime. In the latter case, we find evidence for a resonant behavior, beyond the expected behavior, when the reorganization energy E_r coincides with the driving frequency. Moreover, we investigate how the coherent destruction of tunneling within the two-level system is influenced by the non-Markovian environment.

We compare our results for the undriven TLS with the outcome of real-time Monte Carlo simulations [69] and show that the QUAPI approach gives reliable results in the non-Markovian strong coupling case (section 4.2.2). In addition, we include an external time-dependent drive at frequency ω_l and show in section 4.2.3, for moderate and strong driving, that the amplitude of the forced oscillations in the stationary limit strongly depends on ω_l and, moreover, on ω_c. Most interestingly, it turns out that a slow environment together with a slow drive ω_l optimizes the forced oscillations in the stationary limit. Finally, in section 4.2.4, the effect of a slow dissipative environment on the coherent destruction of tunneling in the TLS

is investigated. We find that the bath influence is indeed strongest in the scenario $\omega_c \simeq \Delta$.

4.1 Model and method

4.1.1 Model for the dissipative TLS

The driven two-level system (TLS) bilinearly coupled to a bosonic heat bath is described by the generic spin-boson Hamiltonian (3.1), see section 2.4 for details. In contrast to the previous chapter, the system Hamiltonian $H_S(t)$ is now time-dependent. It is chosen to be in the basis of the two states $|0\rangle$ and $|1\rangle$, each being, for example, the localized charge state of a charge qubit, or the ground state and the excited state of a two-level atom. The TLS, with the tunnel splitting Δ, is driven by a time-dependent external driving field of the form $\varepsilon(t) = A\cos(\omega_l t)$ with amplitude A and driving-frequency ω_l yielding

$$H_S(t) = \frac{\hbar}{2}\left(\Delta\sigma_x + \varepsilon(t)\sigma_z\right) , \tag{4.1}$$

with $\sigma_{i=x,z}$ being the Pauli pseudo-spin matrices. The environment to which the TLS is bilinearly coupled is modeled as a bath of harmonic oscillators with bosonic creation and annihilation operators $b^\dagger, b$ and oscillator frequency ω_α, hence $H_B = \sum_\alpha \hbar\omega_\alpha b_\alpha^\dagger b_\alpha$. The coupling between the TLS and the environment is taken into account by the interaction Hamiltonian

$$H_{SB} = \frac{\hbar}{2}\sigma_z \sum_\alpha g_\alpha \left(b_\alpha^\dagger + b_\alpha\right) , \tag{4.2}$$

with g_α being the coupling constants.

4.1.2 Model for the dissipative photosynthetic light-harvesting effective TLS

Complex photosynthetic biomolecular structures have recently been shown to exhibit quantum interference properties [23, 24]. In particular, energy transfer among the excitons within chlorophyll complexes of the sulfur [23] and the purple [24] bacteria have provided evidence for long-lived (picosecond time scale) quantum coherent excitonic dynamics, a fact that has only recently become associated to the efficiency of the energy transfer from the LH antenna complexes to the chemical reaction centers in such large biomolecules [23, 24].

In this work, we are interested in the dissipative dynamics of the minimal, basic unit of a photosynthetic LH complex which would allow us to model and control quantum interference mechanisms taking place in such nanostructures. This is done by modeling the specific case of an interacting pair of chromophores in a LH II ring [18]. The effective single TLS is built up from two chromophores which are

coupled by the Förster resonant energy transfer Δ, as sketched in fig. 4.1(a), where $\hbar\omega_j$ is the transition energy for chromophore j. Since the fluorescence lifetime of the single chromophore is much larger than the other time scales of the system [22], no radiative decay of the excitations is taken into account, and we can write the Hamiltonian for the two-chromophore system in the basis $\mathcal{B}_2 \equiv \{|g_1\rangle \otimes |g_2\rangle, |g_1\rangle \otimes |e_2\rangle, |e_1\rangle \otimes |g_2\rangle, |e_1\rangle \otimes |e_2\rangle\}$, where g_j (e_j) corresponds to the ground (excited) state of chromophore j. The Δ–Förster coupling between the two chromophores (fig. 4.1(a)) comprises a dipole-dipole interaction which produces a non-radiative transfer of an excitation between the chromophores. Such an interaction can be written as [107] $H_{int} = \frac{\hbar\Delta}{2}(\sigma_x^1\sigma_x^2 + \sigma_y^1\sigma_y^2)$, and the Hamiltonian of the bare system becomes

$$H_S = H_1 \otimes \sigma_0^2 + \sigma_0^1 \otimes H_2 + H_{int}\,, \tag{4.3}$$

where σ_0^i is the identity matrix in the space of chromophore i.

The correlations due to the bath enter through the coupling to a surrounding protein environment and to a polar solvent, which, in general, exhibits a frequency dependent dielectric constant [108]. For the details of such a mechanism and their possible geometric configurations, we refer to [108]. Formally, this process can be modeled by means of a quantized reaction field operator $R^i \equiv \sum_\alpha D_\alpha^i(b_{i,\alpha} + b_{i,\alpha}^\dagger)$, where D_α^i couples the chromophores i to the surrounding environment. This, in turn, is modeled as a bath of harmonic oscillators which comprise the energy stored in the polar solvent. Such modes are represented via the bosonic operators b_α, and, as in the previous section, the bath Hamiltonian reads $H_B = \sum_\alpha \hbar\omega_\alpha b_\alpha^\dagger b_\alpha$. If $\delta\mu_i$ denotes the change in the dipole moment of molecule i during the transition[1], the two chromophores are coupled to their environment via the interaction Hamiltonian

$$H_{SB} = \frac{\hbar}{2}\left[\left(\delta\mu_1\sigma_z^1\sum_\alpha D_\alpha^1(b_\alpha + b_\alpha^\dagger)\right)\otimes\sigma_0^2 + \sigma_0^1\otimes\left(\delta\mu_2\sigma_z^2\sum_\alpha D_\alpha^2(b_\alpha + b_\alpha^\dagger)\right)\right]$$

The total Hamiltonian for the two-chromophores is then written in the basis $\mathcal{B}_2$ as

$$\begin{aligned} H &= H_S + H_B + H_{SB} = \\ &= \sum_\alpha \hbar\omega_\alpha b_\alpha^\dagger b_\alpha + \frac{\hbar}{2}\begin{pmatrix} -(\Omega_+ + V_+) & 0 & 0 & 0 \\ 0 & -(\Omega_- + V_-) & 2\Delta & 0 \\ 0 & 2\Delta & \Omega_- + V_- & 0 \\ 0 & 0 & 0 & \Omega_+ + V_+ \end{pmatrix} \end{aligned} \tag{4.4}$$

where $\Omega_\pm \equiv \omega_1 \pm \omega_2$, and $V_\pm \equiv \delta\mu_1 R^1 \pm \delta\mu_2 R^2$. Given the biophysical nanostructure composition of the LH II rings [18], we assume that the states of the single chromophores couple to the same surrounding protein bath. Consequently we set $D \equiv D^1 = D^2$, and drop any subscripts that may differentiate the bath modes associated to chromophores 1 and 2 in H_B[2].

[1] $\mu_i = \langle e|\hat{\mu}|g\rangle_i$ is the transition dipole moment of chromophore i.

[2] A coupling of the two chromophores to two uncorrelated baths can easily be included within the QUAPI method, but is not within the aim of the present work.

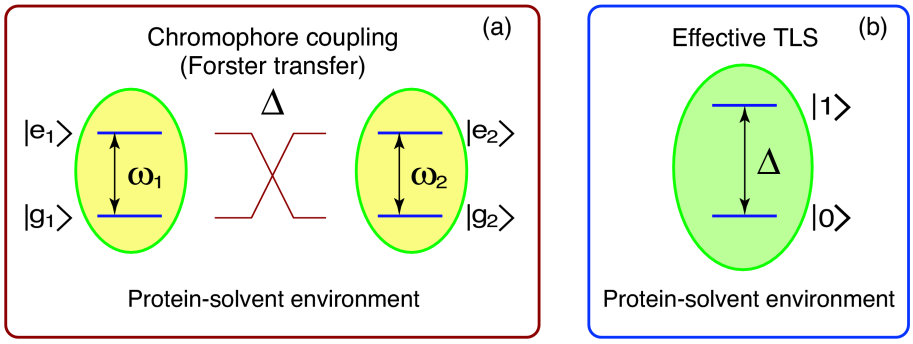

Figure 4.1: Sketch of the effective light harvesting biomolecular TLS formed from a pair of $\Delta-$Förster interacting chromophores.

If only singly excited states are taken into account, from the Hamiltonian eq. (4.4) we identify the active environment coupled 2D-subspace $\{|e_1\rangle\otimes|g_2\rangle, |g_1\rangle\otimes|e_2\rangle\}$. In this central subspace of eq. (4.4), the effective interacting biomolecular TLS Hamiltonian reads

$$H = \left(\frac{\hbar\Omega}{2}\sigma_z + \hbar\Delta\sigma_x\right) + \frac{\hbar}{2}\sigma_z\sum_\alpha g_\alpha\left(b_\alpha + b_\alpha^\dagger\right) + \sum_\alpha \hbar\omega_\alpha b_\alpha^\dagger b_\alpha \ , \tag{4.5}$$

with $g_\alpha \equiv D_\alpha(\delta\mu_1 - \delta\mu_2)$ being the bath coupling constants, and $\Omega \equiv \Omega_-$. Now the defined effective biomolecular TLS has tunneling splitting Δ; if, as before, such a TLS is driven by a time-dependent external driving field $\varepsilon(t) = A\cos(\omega_l t)$, and we consider that both chromophores have equal transition energies ($\omega_1 = \omega_2$), the Hamiltonian eq. (4.5) becomes equal to the total Hamiltonian $H(t)$ eq. (3.1), and hence we have effectively mapped the interacting, environment correlated chromophore system Hamiltonian to that of a generic effective spin-boson Hamiltonian. This is schematically illustrated in fig. 4.1(b), where Δ is the associated "tunneling energy", between the new basis states $|0\rangle$ and $|1\rangle$ for the effective biomolecular TLS (formerly the $\mathcal{B}_2$–basis states $|ge\rangle$ and $|eg\rangle$, respectively).

To gain information on the full dynamics of the system, the initial conditions at $t = 0$ have to be specified. Again we make use of the factorizing initial conditions, specified in eq. (2.33).

The environment is fully characterized by the spectral density $J(\omega) = \sum_\alpha g_\alpha^2\delta(\omega-\omega_\alpha)$, being a quasi-continuous function for typical condensed phase applications. It determines all bath-correlations that are relevant for the system via the bath auto-correlation function [11, 83], eq. (2.18)

For what is reported in the following, we use an Ohmic spectral density with an exponential cut-off, i.e.,

$$J(\omega) = 2\pi\alpha\omega\exp(-\omega/\omega_c), \tag{4.6}$$

where the dimensionless parameter α describes the damping strength and ω_c is the cut-off frequency. An Ohmic spectral density is a proper choice for, e.g. electron

transfer dynamics [69, 109] or biomolecular complexes [18, 22], as well as in the case of Josephson junction qubits [110]. In the case of charge qubits subjected to a phonon bath, a different spectral density, with a super-Ohmic low-frequency behavior, results better suited [17] and e.g. chapter 3.

To complete the model we have to specify the environmental coupling, i.e. it will be shown that the spectral density associated to the bacteriochlorophylls in the LH II complexes considered in this chapter being Ohmic in nature is based on a microscopic derivation [111, 108]. The biomolecule modeled as a TLS is coupled to a solvent bath and has a permanent dipole moment μ. In the simplest picture the solvation process can be described in terms of the Onsager model [112, 113] which is a continuous model that has been widely used in studies of solvation processes, e.g. in refs. [114, 115]. Here, the solute is treated as a point dipole which is surrounded by a spherical cage of polar solvent molecules with Onsager radius a, which typically exhibits the size of the solute molecule [111, 112, 113], for a sketch see fig. 4.2.

The central cavity has a dielectric constant $\varepsilon_r = 1$ since it is assumed to be in vacuum. The central dipole now polarizes the cage, which in turn produces an electric field inside the cavity, named the reaction field $R(t)$. In case of a uniform spherical cavity the reaction field is constant everywhere inside [116]. The field then acts back on the dipole with interaction energy $E = -\vec{\mu}(t) \cdot \vec{R}(t)$ and typically lowers the total energy and hence forms a stable structure. To quantize $R(t)$, it is expressed in the Heisenberg picture within its Fourier modes as [111]

$$R(t) = \sum_\alpha e_\alpha \left(a_\alpha e^{-i\omega_\alpha t} + a_\alpha^\dagger e^{i\omega_\alpha t} \right) . \tag{4.7}$$

The coefficients are quantized such that a_α and $a_\alpha^\dagger$ obey bosonic commutation relations. Therefore the environment is modeled as a bath of harmonic oscillators.
Next, the spectral density is specified following [111]. Noting that with no solute-solvent interaction $\langle R(t) \rangle = 0$, the reaction field correlation function

$$S(t) = i \langle R(t) R(0) \rangle \Theta(t) \equiv i \langle 0 | e^{iHt} R e^{-iHt} R | 0 \rangle \Theta(t) \tag{4.8}$$

is examined. Here, $|0\rangle$ is the ground state of the harmonic oscillators of the environment and H is the Hamiltonian of the environment, e.g. eq. (2.5). It turns out that the imaginary part of the Fourier transform of $S(t)$, denoted as $\mathcal{E}(\omega)$ is relevant. It can be written as a sum over energy eigenstates [111, 117]

$$\mathrm{Im}\mathcal{E}(\omega) = \sum_n \delta(\omega - E_n) |\langle 0 | R | n \rangle|^2 . \tag{4.9}$$

Expanding $R(t)$ again in its normal modes, one finds that all terms $\langle 0|R|n\rangle$ vanish except for when a single bath oscillator is singly occupied [111]. These states have energy $E_n = \omega_\alpha$ and $\langle 0|R|n\rangle = e_\alpha$. With this eq. (4.9) turns into

$$\mathrm{Im}\mathcal{E}(\omega) = \sum_n e_\alpha^2 \delta(\omega - \omega_\alpha) \tag{4.10}$$

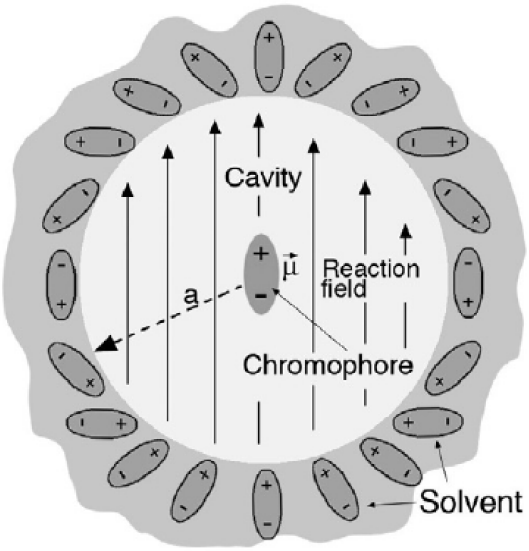

Figure 4.2: Onsager model of solvation. The chromophore is treated as a point dipole μ inside an empty cavity of radius a, which is surrounded by a polar solvent. The dipole polarizes the solvent which in turn creates an electric field which acts back on the dipole, stabilizing the solvated system. Figure taken from [111].

and together with the definition of the spectral density (2.26) one ends up with

$$J(\omega) = (\Delta\mu)^2 \mathrm{Im}\mathcal{E}(\omega)\,. \tag{4.11}$$

For calculating the reaction field fluctuations one has to note that in the Onsager model [112] $R(t)$ and the central dipole $\mu(t)$ are related via a response function $\chi(t-t')$ [118], such that in Fourier space $R(\omega) = \chi(\omega)\mu(\omega)$. In the static limit, where the solvent cage adjusts instantaneously, one has $R(t) = \chi_s\mu(t)$ [112, 116]. For realistic systems, the solvent cage will lag behind changes of the dipole due to the electric friction and $\chi(\omega)$ is then given by [119]

$$\chi(\omega) = \frac{1}{4\pi\varepsilon_0 a^3}\frac{2(\varepsilon(\omega)-1)}{2\varepsilon(\omega)+1} \tag{4.12}$$

where $\varepsilon(\omega)$ is the frequency dependent dielectric constant of the solvent which reads according to the Debye formula [120]

$$\varepsilon(\omega) = \varepsilon_\infty + \frac{\varepsilon_s - \varepsilon_\infty}{1 - i\omega\tau_D}\,. \tag{4.13}$$

Here, ε_∞ and ε_s are the high and low frequency limits, respectively. τ_D is the Debye relaxation time, which is the bulk reorientational relaxation time of the solvent

dipole [111]. Applying now the fluctuation-dissipation theorem yields with use of eqs. (4.11) and (4.13)

$$J(\omega) = \frac{(\Delta\mu)^2}{2\pi\varepsilon_0 a^3} \frac{6(\varepsilon_s - \varepsilon_\infty)}{(2\varepsilon_s + 1)(2\varepsilon_\infty + 1)} \frac{\omega\tau_E}{\omega^2\tau_E^2 + 1} \tag{4.14}$$

for the spectral density [111], with $\tau_E = \frac{2\varepsilon_\infty+1}{2\varepsilon_S+1}\tau_D$. This specific form of $J(\omega)$ is an interesting result since it is based on a specific microscopic basis, similar to the spirit of the spectral density for donor based charge qubits in chapter 3. Note that $J(\omega)$ has an implicit high frequency cut-off at $\omega_c = \frac{1}{\tau_E}$ related to the finite relaxation time of the solvent dipole. Below the cut-off, $J(\omega) = \eta\omega$, where

$$\eta = \frac{(\Delta\mu)^2}{4\pi\varepsilon_0 a^3} \frac{6(\varepsilon_s - \varepsilon_\infty)}{(2\varepsilon_s + 1)^2} \tau_D \tag{4.15}$$

corresponding to the classical friction coefficient η, introduced in chapter 2.

In addition, different forms of a Debye dielectric solvent have been considered [111, 108]. In general, they lead to the Ohmic type of spectral density given by eq. 4.6. The dimensionless damping constant α of the protein-solvent is directly related to the parameters of the dielectric model [108], and has been estimated to be in the range $\alpha \sim 0.01 - 1$ [22, 108].

The exponential decay of the high-frequency cut-off ω_c sets the bath characteristic time-scale. If $\Delta \ll \omega_c$, the bath is very fast compared to the effective TLS and loses its memory quickly. Here, a Markovian approximation is appropriate and the standard Bloch-Redfield description [18] applies. However, for the considered biomolecular environment, $\hbar\omega_c$ is typically of the order of $\sim 2 - 8$ meV, while the Förster coupling strengths $\hbar\Delta \sim 0.2 - 100$ meV [22, 108]. Hence, the bath responds slower than the dynamics of the excitons evolve and non-Markovian effects become dominant, a regime which is accessible only by rather advanced techniques.

Below, we report results in the scaling limit $\Delta, T \ll \omega_c$ and vary ω_c such that the system reaches the crossover to the adiabatic limit, i.e., $\omega_c \sim \Delta$. Both regimes, and the associated crossover, have been studied by real-time Quantum Monte Carlo simulations for electron transfer dynamics within the undriven TLS for selected parameter combinations [69]. In this chapter, we go beyond this by including an external laser driving and, furthermore, by covering the entire parameter space. Concerning the coupling between the TLS and its environment, we study the whole parameter window from the weak coupling limit $\alpha \ll \Delta$ to the strong coupling limit $\alpha \sim \Delta$.

4.2 Dynamics of the driven TLS

The dynamics of the TLS introduced in the previous section is described in terms of the time evolution of the reduced density matrix $\rho(t)$ which is obtained by tracing over the bath degrees of freedom. The TLS dynamics always evolves from the initial state $\rho_S(0) = |1\rangle\langle 1|$.

In order to investigate the dynamics of the system, we use the QUAPI scheme [21], introduced in detail in sec. 3.3. As the environmental fluctuations live on a time scale $\sim 1/\omega_c$, it is particularly important to include the full memory when $\omega_c \simeq \Delta$. Note that for any finite temperature, $L(t)$, eq. (2.18) decays exponentially at long times [11], thus justifying this approach. Moreover, K has to be increased, until convergence with respect to the memory time has been found. Typical values, for which convergence can be achieved for our spin-boson system, are $K \leq 12$ and $\delta t \sim (0.1 - 0.2)/\Delta$.

With the time evolution of the reduced density matrix $\rho(t)$ at hand we can now study the dynamics of the driven TLS in terms of the population difference $P(t) = \langle \rho(t)\sigma_z \rangle$ of the two states, with the initial condition $P(0) = 1$.

4.2.1 Markovian vs non-Markovian dynamics

Before addressing the effect of driving, we convince ourselves that the dynamics is indeed non-Markovian when $\omega_c \simeq \Delta$. For this, we compare the numerical exact QUAPI with a Bloch-Redfield approach. To be specific, we compare the QUAPI data with the outcome of the weak coupling approximation, see (21.171) and (21.172) in [11], which results from a first order approximation in α. In [121], it has been shown that the outcome of the weak coupling approach is equivalent to a Bloch-Redfield treatment.

In fig. 4.3 (a) the result for $\alpha = 0.001$ and $\omega_c = 100\Delta$ is shown. As expected, the agreement between both results is perfect since the system is deep in the Markovian (weak coupling) regime. For fig. 4.3 (b) the coupling is increased to $\alpha = 0.01$ and since the bath is still in the scaling limit there is acceptable agreement. In contrast, for a cut-off frequency $\omega_c = \Delta$, see fig. 4.3 (c), strong deviations between the Bloch-Redfield approach and the QUAPI approach arise, indicating that the environment is non-Markovian in nature here. When the damping is furthermore increased to $\alpha = 0.1$ the disagreement between the numerical exact QUAPI and the weak coupling approximation is enhanced, see figs. 4.4 (a) and (b). This indicates that the choice of ω_c away from the scaling limit induces a non-Markovian behavior of the dissipative TLS dynamics which is further underpinned by fig. 4.4 (c), where the relaxation rate γ_r is shown. We obtain this from a fit of a decaying cosine function with a single exponential to $P(t)$. In the scaling limit $\Delta \ll \omega_c$ both approaches yield the same γ_r, whereas strong deviations occur for smaller ω_c. Note that ω_c enters (21.171) in [11] via the renormalized tunneling amplitude Δ_{eff} which is included here in the weak-coupling approximation.

4.2.2 Undriven case: comparison with Quantum Monte Carlo results

Next, in order to validate our results in the highly non-Markovian crossover regime $\omega_c \sim \Delta$, we compare our results with the outcome of real-time Quantum Monte Carlo (QMC) simulations [109]. In fig. 4.5 (main), the results for the high temperature

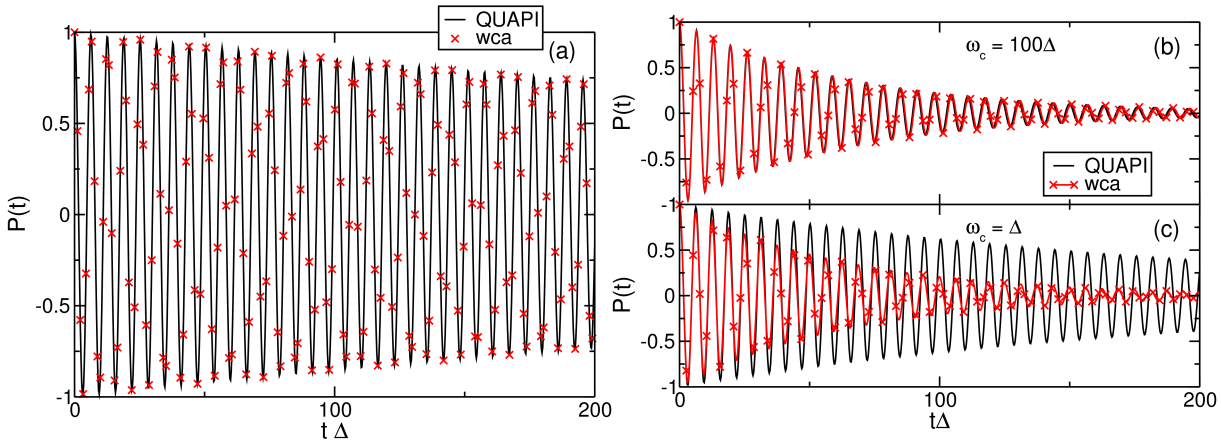

Figure 4.3: Population difference $P(t)$ (solid line: weak coupling approach, symbols: QUAPI). (a) $\alpha = 0.001$ and $\omega_c = 100\Delta$ (Markovian regime), (b) $\alpha = 0.01$ and $\omega_c = 100\Delta$ and (c) $\alpha = 0.01$ and $\omega_c = \Delta$. The temperature is always $T = 10\Delta$.

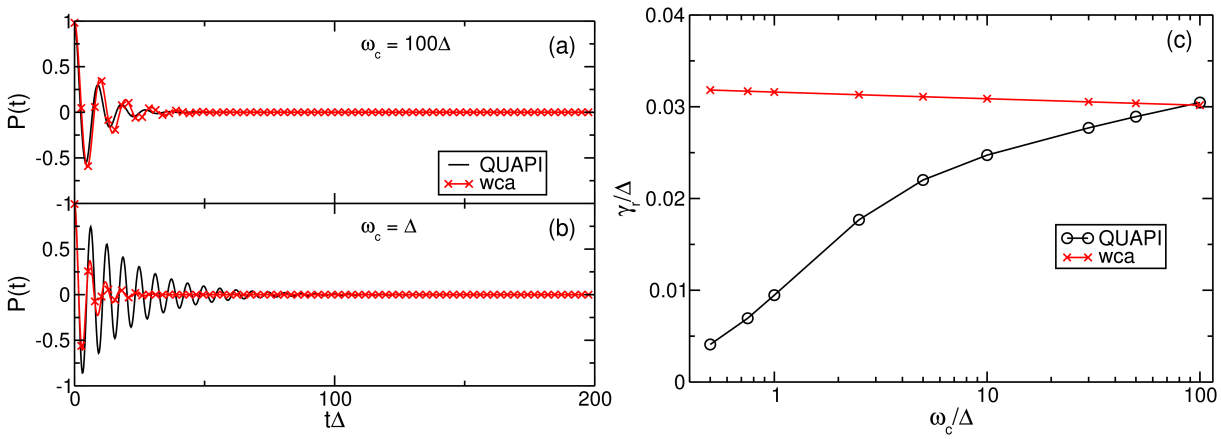

Figure 4.4: Same as 4.3, but for a strong coupling $\alpha = 0.1$. (c) shows the relaxation rate γ_r as a function of ω_c.

regime are shown, where the parameters are $T = 4\omega_c$ and $\alpha = 2$ (strong coupling). In perfect (also quantitative) agreement with [109], $P(t)$ decreases faster for $\Delta/\omega_c = 2.4$ than for $\Delta/\omega_c = 1.6$. The cut-off frequency is also related to the reorganization energy of the environment [11], which has the form $E_r = \int_0^\infty d\omega \frac{J(\omega)}{\pi\omega} = 2\alpha\hbar\omega_c$ for an Ohmic environment. Hence, our results are consistent with the physical expectation, since the dynamics of the environment is slower for the smaller ratio Δ/ω_c for the same α. For the low temperature regime $T = 0.4\omega_c$, shown in the inset of fig. 4.5, we also observe agreement of the QUAPI results with the outcome of [109]. To show the full dependence of the population difference on the cut-off frequency ω_c, we show in fig. 4.6 results for $\alpha = 0.1$. $P(t)$ decays with time in an oscillatory way.

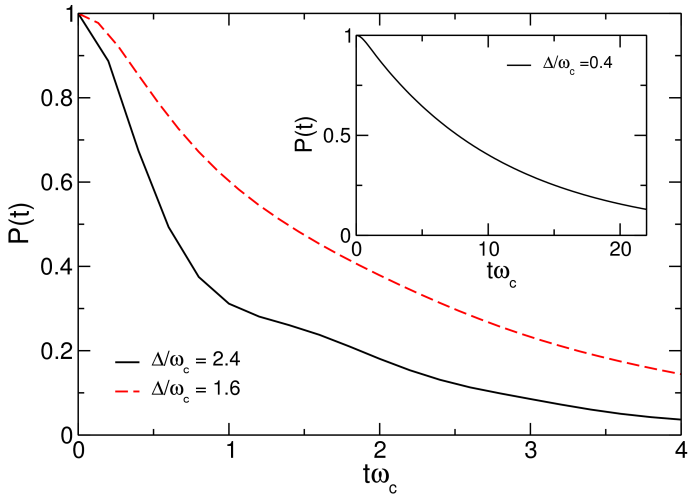

Figure 4.5: Population difference $P(t)$ for the TLS for different cut-off frequencies ω_c and a damping parameter $\alpha = 2$. The temperature is $T = 4\omega_c$ (main) and $T = 0.4\omega_c$ (inset).

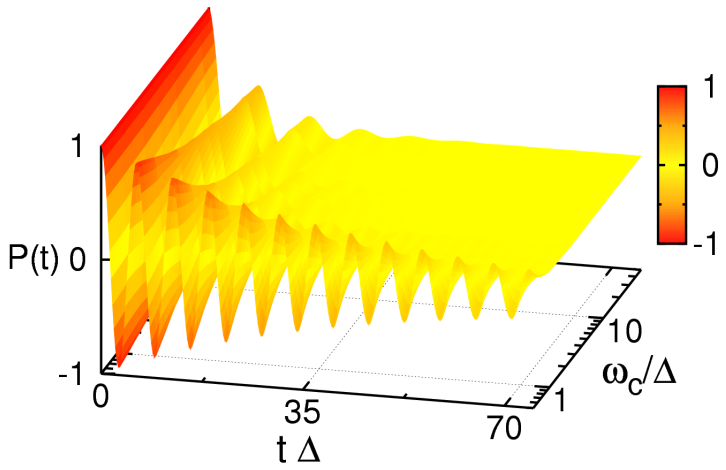

Figure 4.6: Population difference $P(t)$ for a single chromophore pair and full cross-over from a Markovian to a non-Markovian responding bath. The time scale and the bath cut-off frequencies ω_c are in units of the pair Förster coupling Δ. The dynamics is calculated for $k_BT = 0.1\hbar\Delta$, and $\alpha = 0.1$.

The decay occurs faster for large ω_c while for small ω_c, the sluggish bath sustains more coherent oscillations which persist even on the ps time scale in dimensionful units. In general, for smaller ω_c the spectral weight of the bath modes around the system frequency Δ is suppressed and the decohering influence is reduced, yielding prolonged coherence. This can be understood again in terms of the reorganization energy.

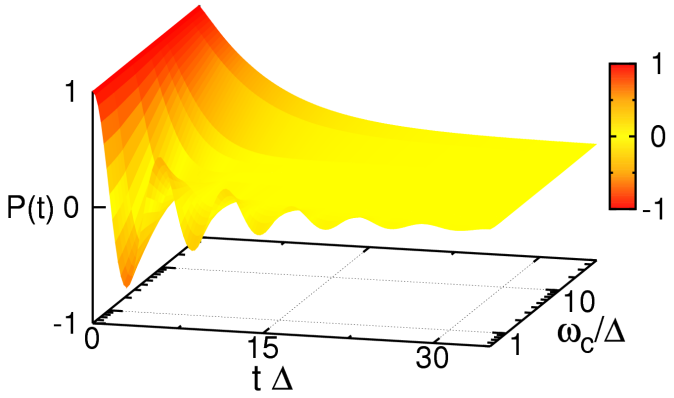

Figure 4.7: Population difference $P(t)$ for the undriven TLS system in dependence on the cut-off frequency ω_c. The temperature is $T = 0.1\Delta$ and the damping parameter is $\alpha = 0.6$.

Furthermore, we address the case of strong coupling between the TLS and its environment. For the scaling limit $\Delta \ll \omega_c$ it is known that there is a transition at $\alpha = 0.5$ from a coherent decay of $P(t)$ for $\alpha < 0.5$ to an incoherent decay for $\alpha > 0.5$ [11, 122]. To be specific, we choose $\alpha = 0.6$ at a low temperature $T = 0.1\Delta$, as shown in fig. 4.7. Again, this behavior can be understood in terms of the reorganization energy E_r, since decreasing ω_c here has a similar effect as lowering the damping parameter α. By means of our numerical exact method, fig. 4.7 quantifies how the transition between coherent and incoherent behavior depends on ω_c for a given α.

We next put our results in the context of the modeled effective biomolecular TLS. For excitations in the LH-II ring of the bacteria chlorophyll molecule (BChls in LH-II complexes), the Förster coupling strength $\hbar\Delta \sim 46 - 100$ meV, and $\hbar\omega_c \sim 2 - 8$ meV [22, 108], and hence the ratio $\frac{\omega_c}{\Delta} \sim 0.1$. For these complexes, α is of the order of $0.1 - 1$ [108], evidencing a strong coupling between the chromophores and the solvent dielectric. If we make $\alpha = 0.1$, $\hbar\Delta = 100$ meV, and plot a graph such as the one of fig. 4.7 for $T = 0.1\Delta$ (~ 116 K), long-lived coherent oscillations are sustained for a time of around 530 fs ($t\Delta \sim 80$). Such oscillations can be visualized at fixed $\omega_c = 0.1\Delta$. This rough estimation is in agreement with the time scale of the coherent oscillations recently measured in [23] for the antenna complex from a green sulfur bacteria that has seven BChls per protein subunit. If, on the other hand, we set $\alpha = 0.6$, $\omega_c = 0.1\Delta$ (as shown in fig. 4.7), coherent oscillations are also found but, due to the stronger coupling to the bath, they decay quicker than for the case $\alpha = 0.1$. We thus observe that for the rather simple effective biomolecular TLS model introduced here, which is aimed as a guide to the possible realization of further proof-of-principle experiments, we are able to demonstrate that the non-Markovian features of the protein-solvent environment help to sustain the quantum coherence mechanisms exhibited by the coupled chromophores in a LH-II ring. Since

our results are of a general character, in principle derived from a generic TLS, we also expect them to be valid in artificially designed nanostructures with the specific bath properties described here.

4.2.3 Driven case $A \neq 0$

We now address the influence of a finite periodic external driving field. The results for $A = \Delta$ and $\omega_l = 0.05\Delta$ are shown in fig. 4.8. Similarly to the undriven case, the overall decay of $P(t)$ is faster for larger ω_c: compare, for example, fig. 4.8 (a) for $\omega_c = 1.5\Delta$ and fig. 4.8 (b) for $\omega_c = 30\Delta$, both in the weak-coupling situation $\alpha = 0.01$. In turn, for the case $\omega_c \sim \Delta$, the superimposed oscillations due to coherent tunneling survive longer than in the scaling-limit $\Delta \ll \omega_c$ (fig. 4.8(b)), before the system reaches its stationary state. There, only the stationary oscillations due to the external driving field survive. For a stronger system-bath coupling α the decay of $P(t)$ is faster, as expected, and the stationary state is reached faster. As in the undriven case, the described behavior is qualitatively understandable in terms of the reorganization energy E_r.

For increasing driving strength to $A = 10\Delta$, the dependence of the TLS dynamics on ω_c and α is similar. However, the form of the stationary oscillations turns out to be qualitatively different from the case of a small drive amplitude A. Here, stable stationary plateaus emerge, as shown in fig. 4.9. In [14], this has been observed experimentally for frequency-modulated excitations of a two-level atom, using a microwave field to drive transitions between two Rydberg-Stark states of potassium. In the presence of a slow frequency modulation, square wave oscillations of the population difference have been detected. They can be understood to mean that the large driving amplitude leads to an extreme biasing of the TLS dynamics. The center of the observed plateaus correspond to the extrema of the applied cosine driving field. At the position of these maxima, the TLS is maximally biased and since the time-scale of the driving field is much smaller than the time-scale of the (unbiased) TLS dynamics due to Δ, the situation of an extreme quasistatic bias results, forming an intermediate self-trapping around the maxima of the cosine-like driving field. Indeed, this intermediate self-trapping becomes shorter lived, and increasingly washed out, when the $\omega_l \sim \Delta$ (not shown here).

In a next step, it is interesting to consider the amplitude A_∞ of the forced oscillations in the stationary limit. In fig. 4.10, we show the results for the nonlinear response for the case $\alpha = 0.1$ and a driving field amplitude $A = \Delta$. We observe a rather weak dependence when $\omega_l \lesssim \Delta$, but the response becomes rather weak in the regime of strong detuning. We are able to identify an optimal driving frequency $\omega_l \sim \Delta/2$, where the amplitude of the forced oscillations has a maximum. Note that this rather weak resonance is due to the sizeable damping $\alpha = 0.1$. The behavior depicted in fig. 4.10 is, essentially, not influenced by the cut-off frequency ω_c and is thus independent of the time scale of the environment.

A natural question is whether to expect an enhancement of the response when all frequencies are comparable, i.e., $\omega_l \sim \omega_c \sim \Delta$. This situation is addressed in

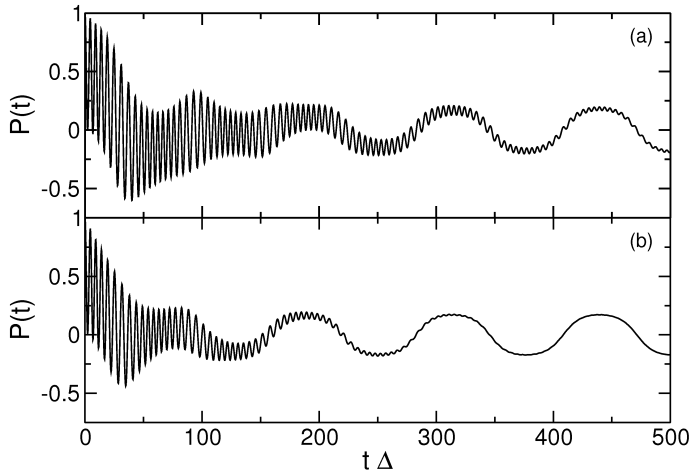

Figure 4.8: Population difference $P(t)$ for the driven TLS. The amplitude of the driving-field is $A = \Delta$ and the driving-frequency is $\omega_l = 0.05\Delta$. The temperature is $T = 0.1\Delta$ and the damping parameter is $\alpha = 0.01$. The cut-off frequency is (a) $\omega_c = 1.5\Delta$ and (b) $\omega_c = 30\Delta$

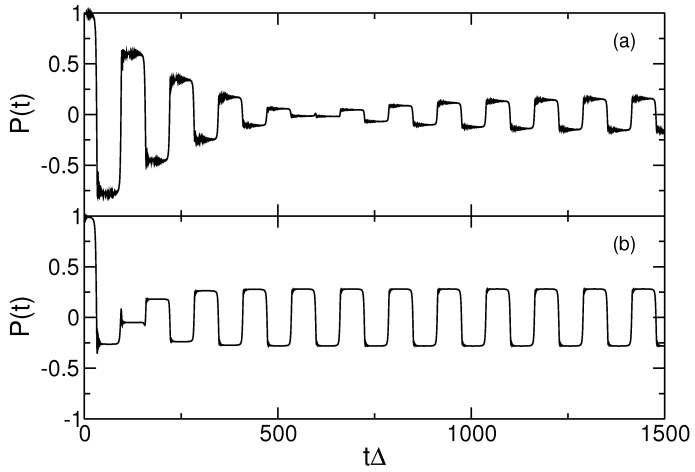

Figure 4.9: Population difference $P(t)$ for the driven single qubit system. The amplitude of the driving-field is $A = 10\Delta$, the driving-frequency is $\omega_l = 0.05\Delta$, the cut-off frequency is $\omega_c = 0.5\Delta$ and temperature is $T = 0.1\Delta$. The damping parameter is (a) $\alpha = 0.1$ and (b) $\alpha = 0.6$.

fig. 4.11, where we have chosen $\omega_l = 0.5\Delta$. We find that for weak to intermediate driving, no pronounced resonance appears, as shown in fig. 4.11 (a) for the case $A = \Delta$. In contrast, strong driving can induce a resonant nonlinear response which, however, requires non-Markovian dynamics, i.e., $\omega_c \sim \Delta$. This is illustrated in fig. 4.11 (b) for $A = 10\Delta$. A slow non-Markovian bath with $\omega_c \lesssim \Delta$ is thus much more efficient in maximizing forced oscillations in the stationary limit. This feature occurs for the weak coupling ($\alpha = 0.01$) as well as for the strong coupling case $\alpha = 0.6$.

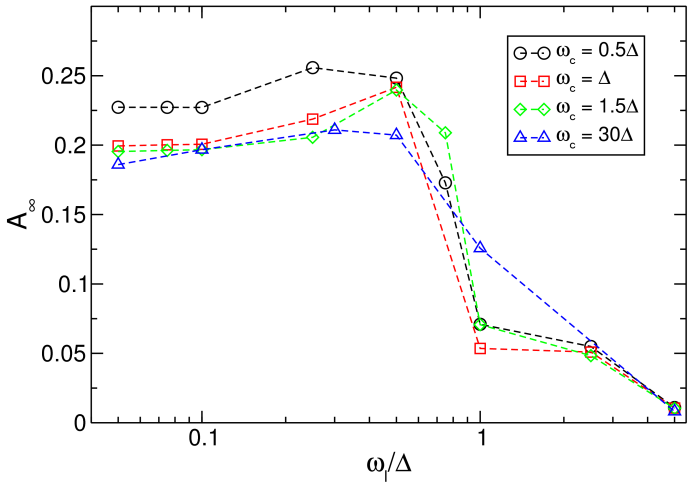

Figure 4.10: Amplitude of the forced oscillations in the stationary limit A_∞ as a function of the driving frequency ω_l for $A = \Delta$ with $\alpha = 0.1$ and different cut-off frequencies ω_c.

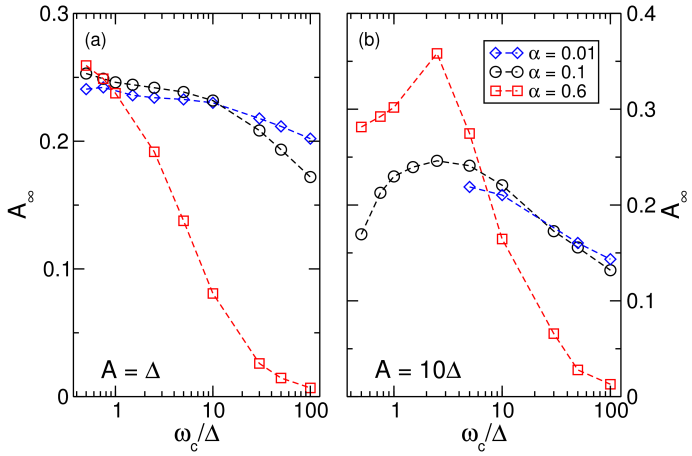

Figure 4.11: Amplitude of the stationary limit A_∞ as a function of the cut-off frequency ω_c for $\alpha = 0.6$, $A = \Delta$ and a temperature $T = 0.1\Delta$.

This constitutes another example where a non-Markovian bath helps in protecting coherence in a quantum system over a finite time interval, see also chapter 5.

In contrast, a Markovian environment in the scaling limit, $\Delta \ll \omega_c$, largely suppresses forced oscillations via its destructive influence on coherence. This finding is most pronounced in the incoherent strong coupling case, $\alpha = 0.6$. The dependence of A_∞ on ω_c is again qualitatively understandable via the reorganization energy E_r in the case of weak driving. It explains the reduction of the response for weaker damping ($\alpha = 0.1$ and $\alpha = 0.01$), compared to the strong damping case $\alpha = 0.6$ (fig. 4.11 (a)). However, for stronger driving, $A = 10\Delta$, the resonance effect is more pronounced for a strong coupling situation, $\alpha = 0.6$ which cannot be explained in

terms of a growing reorganization energy E_r.

4.2.4 Coherent destruction of tunneling

When an isolated symmetric quantum TLS is driven with large frequencies $\omega_l \gg \Delta$, the bare tunneling matrix element effectively becomes renormalized by the zero-th Bessel function $J_0(x)$ as $\Delta \to J_0(A/\omega_l)\Delta \equiv \Delta_{\text{eff}}$ [12, 123]. The population of the state $|1\rangle$ with an initial preparation $P_1 = 1$ follows as

$$P_1(t) = \cos^2\left(J_0(a/\omega_l)\Delta t/2\right) . \tag{4.16}$$

This implies that for particular choices of the driving parameters, the Bessel function term can be fixed to zero. The first zero then corresponds to $A/\omega_l = 2.40482...$, and then, $P_L(t)$ equals unity, since the effective tunnel splitting vanishes. This phenomenon is known as coherent destruction of tunneling (CDT); see [12] and references therein for further details.

Naturally, the phenomenon of CDT is influenced when the TLS is coupled to an Ohmic environment. A complete standstill of the dynamics will not occur any longer, due to the relaxation processes induced by the bath. For an Ohmic environment in the scaling limit under the assumption of weak damping, this question has been addressed in [124]. Here, we extend these studies to the case of finite ω_c and choose a driving frequency $\omega_l = 20\Delta$.

For weak coupling, $\alpha = 0.01$, the CDT is only weakly influenced by the environment, as expected, and it turns out that the dependence on the cut-off frequency of the bath ω_c is also weak, as shown in fig. 4.12 (left). Nevertheless, we find that the unavoidable decay of $P(t)$ occurs the slowest when $\omega_c \sim \Delta$. For stronger coupling $\alpha = 0.1$, as shown in fig. 4.12 (right), CDT is more strongly influenced. We observe, again, that a slow bath helps to preserve coherence and the decay of $P(t)$ is slow.

In the regime of strong damping, the situation is different. In fact, we find an opposite qualitative behavior which goes beyond the above given explanation in terms of E_r. In fig. 4.13, the corresponding results for $\alpha = 0.6$ are shown. As one can see, the decay of $P(t)$ is in fact the fastest when $\omega_c \simeq \Delta$. This stems from the fact that for the case $\omega_c \sim \Delta$, non-Markovian effects are not negligible, since the time-scales of system and environment are of the same order, which is reflected in the fact that the spectral density $J(\omega)$ has a maximum around Δ. In this resonant situation, the bath modes around the characteristic time scale $1/\Delta$ of the TLS are most important and consequently the decay under the CDT conditions is most pronounced. In turn, in the scaling limit, the decay under CDT conditions is slow. Interestingly, in both cases of strong coupling ($\alpha = 0.1; 0.6$) the population difference is almost maintained without decay by the slow bath $\omega_c \sim 0.1\Delta$, and the decay of $P(t)$ is the slowest.

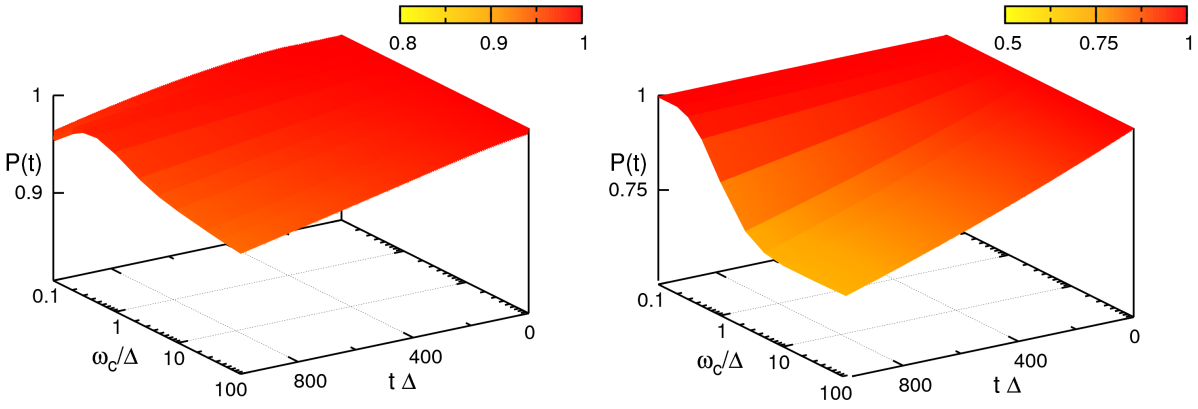

Figure 4.12: Population difference $P(t)$ for the driven TLS in the regime of coherent destruction of tunneling ($\omega_l = 20\Delta$). The temperature is $T = 0.1\Delta$ and the damping parameter is (left) $\alpha = 0.01$ and (right) $\alpha = 0.1$. .

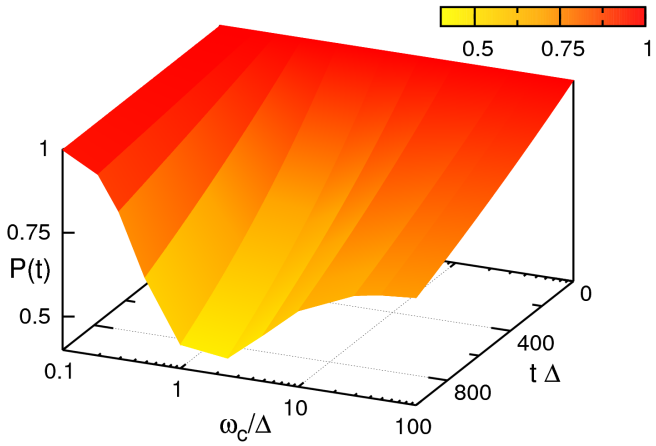

Figure 4.13: Same as 4.12, but for a strong coupling situation, $\alpha = 0.6$.

4.3 Conclusion

We have investigated the dynamics of the driven spin-boson system in the presence of an Ohmic bath. The focus is put on the role of the cut-off frequency ω_c. Based on the numerical exact QUAPI approach, non-Markovian effects are shown to be relevant when $\omega_c \sim \Delta$. This effect is more pronounced for strong damping, as expected, and as can be seen from the relaxation rate γ_r shown in fig. 4.4. The validity of the QUAPI method in the regime $\omega_c \sim \Delta$ is confirmed by the perfect agreement with published results of real time Quantum Monte Carlo simulations [69].

For the unbiased case and for strong coupling, we show that damped coherent oscillations exist in the population difference $P(t)$ if the bath has a cut-off frequency away from the scaling limit, where the decay is known to be incoherent in nature,

as shown in fig. 4.7. By comparison with relevant experimental data, we were able to show that our results are directly applicable to biomolecular systems, namely to the light harvesting complex LH-II of the bacteria chlorophyll molecule. We have shown that a sub-unit of such a biomolecular system can effectively be described by means of the spin-boson model and have demonstrated that the non-Markovian features of the protein-solvent environment help to sustain the quantum coherence mechanisms exhibited within the LH-II complex. Moreover, since our results are based on a model of general character, we expect them to apply also for a variety of artificially designed nanostructures with the specific bath properties reported here.

Regarding the coherent control of the effective TLS, we found that a strong external driving amplitude in combination with a slow driving laser frequency produce a population difference with square wave oscillations in the stationary limit, in agreement with the experimental results reported in [14]. These square-wave like oscillations stem from the fact that the TLS experiences a large quasistatic bias. Moreover, it was shown that the amplitude A_∞ of the forced oscillation in the stationary limit depends strongly on the frequency of the driving field. A slow driving field with $\omega_l \lesssim \Delta$ protects the forced oscillations against the influence of the dissipative environment, whereas in the case of a faster driving, these oscillations are strongly suppressed. This is valid for the weak-coupling as well as for the strong coupling case. For larger driving frequencies, the forced stationary oscillations are considerably reduced. The stationary amplitude of the forced oscillations also strongly depends on the time-scale of the environment determined by ω_c. For strong driving, we find that the stationary amplitude shows resonant features, illustrating that the non-Markovian environment plays a constructive role.

Finally, we investigated the phenomenon of coherent destruction of tunneling under the bath influence. Away from the scaling limit, the influence of the environment is weaker and the CDT survives on a significantly longer time scale. For very strong coupling, i.e., deep in the incoherent regime, the situation is completely different. Here, the CDT is most quickly destroyed when the time scales of the TLS and the environment are in resonance. In such a strong coupling scenario, the preservation of coherence survives longer in the scaling limit; moreover, the CDT is actually helped by the effect of a slow bath (e.g., $\omega_c \sim 0.1\Delta$), where the decay of $P(t)$ is the slowest.

Chapter 5

Enhanced quantum entanglement in the non-Markovian dynamics of biomolecular excitons

In the previous chapter we have investigated the quantum dynamics of a driven TLS subjected to an Ohmic environment being non-Markovian in nature. In this chapter we extend the model in the sense that we now investigate the entanglement dynamics of two coupled TLS subjected to a common bath. In what follows we show that quantum coherence of biomolecular excitons can be sustained over exceedingly long times due to the constructive role of their non-Markovian protein-solvent environment, in contrast to a Markovian environment. We consider the full crossover from a fast to a slow non-Markovian bath and from weak to strong system-bath coupling and show that a slow bath can even generate robust entanglement. This entanglement persists to surprisingly high temperatures, even higher than the excitonic gap. Such a fully quantum mechanical feature is not found for a Markovian bath.

5.1 Model for the chromophore

A single chromophore can be modeled as a quantum two level system and since the system's total number of excitations is a constant of motion, the two-chromophore system can be effectively reduced to a single spin-boson model of one chromophore, see chapter 4 for details. The protein-solvent environment is formalized as a bath of harmonic oscillators with a bilinear system-bath coupling yielding the standard spin-boson Hamiltonian for each chromophore [22]. The effective basis for a chromophore pair is given by $\{|\uparrow\rangle = |e_1 g_2\rangle, |\downarrow\rangle = |g_1 e_2\rangle\}$.

The spectral density of the environment [11] follows from a microscopic derivation [108], see chapter 4 for further details. Different forms of a Debye dielectric can be assumed, but in any case, lead to an Ohmic spectral density $G(\omega) = 2\pi\alpha\omega e^{-\omega/\omega_c}$. The dimensionless damping constant α of the protein-solvent can be related to the parameters of the dielectric model [108]. One finds for the order of magnitude of

$\alpha \sim 0.01 - 0.1$ [22, 108]. We use an exponential form of the cut-off at frequency ω_c. This sets the time-scale on which the dynamics of the bath evolves and is related to the reorganization energy $E_r \sim 2\alpha\hbar\omega_c$. If $\Delta \ll \omega_c$, the bath evolves fast compared to the system and loses its memory quickly, rendering a Markovian approximation and the standard Bloch-Redfield description [18] suitable. However, for the considered biomolecular environment, the energy scales of system and environment are the same, and non-Markovian effects become dominant. Coherent oscillations in a strongly damped two-state system with $\alpha > 1$ and $\Delta \gtrsim \omega_c$ have been found using numerically exact quantum Monte Carlo simulations [109, 69] and by applying the numerical renormalization group [125].

5.2 Excurs on entanglement

Since the main focus in this chapter is on the entanglement of excitons in biomolecular systems, we give a brief introduction on entanglement here, following [28]. For bipartite systems, like the chromophore pair we are concerned with here, entanglement is well understood and described in quantum information theory. Rather considering entanglement as a mystery like in the early days of quantum mechanics, it is nowadays viewed as an important resource in quantum information processing and quantum cryptography to perform certain tasks faster and in a more secure way [28]. The Shor algorithm constitutes a prominent example for that [29].

For pure states the definition of entanglement is simple: a pure state $|\psi\rangle$ is called separable if it can be written as $|\psi\rangle = |a\rangle \otimes |b\rangle$, otherwise it is entangled. An example for a pure separable state is $|\psi\rangle = |00\rangle$ and examples for pure entangled states are the Bell states

$$|\Phi^{\pm}\rangle = \frac{1}{\sqrt{2}}(|00\rangle \pm |11\rangle) \qquad \text{and} \qquad |\Psi^{\pm}\rangle = \frac{1}{\sqrt{2}}(|01\rangle \pm |10\rangle)\,. \tag{5.1}$$

A density matrix ρ for a mixed state can contain classical correlations and it is called separable if it can be written as [126]

$$\rho = \sum_i p_i |a_i\rangle\langle a_i| \otimes |b_i\rangle\langle b_i|\,, \tag{5.2}$$

otherwise it is entangled. Here, the coefficients p_i are probabilities, i.e. $0 \leq p_i \leq 1$ and $\sum_i p_i = 1$. Finding such a decomposition for a given density matrix is a non-trivial task and has only been solved for a few cases.

Therefore other criteria are in demand and one important criterion is the Peres-Horodecki criterion [30, 31]. For this it is required that the density matrix can be written as a direct product of the density matrices of the two subsystems a and b as

$$\rho = \sum_a w_a \rho_a \otimes \rho_b\,, \tag{5.3}$$

where the positive weights w_a satisfy $\sum_a w_a = 1$. Rewriting eq. (5.3) as

$$\rho_{m\mu,n\nu} = \sum_a w_a (\rho_a)_{mn} (\rho_b)_{\mu\nu} \tag{5.4}$$

the Peres-Horodecki criterion can be given. It states that a density matrix describes a separable state if its partial transpose has only non-negative eigenvalues which is a necessary condition. The partial transpose of the composed density matrix is defined as the transpose with respect to one of the subsystem, e.g.

$$\rho^{T_a}_{m\mu,n\nu} = \rho_{n\mu,m\nu} \tag{5.5}$$

where the density matrix has been transposed with respect to subsystem a (the latin indices). Based on this criterion various entanglement measures can be defined, as for instance the concurrence or the negativity [30,31,127]. To quantify the two-pair quantum correlations, we study in what follows the entanglement is measured along the negativity $N(t) = \max\{0, -2\zeta_{\min}(t)\}$ [30,31], where $\zeta_{\min}(t)$ denotes the smallest eigenvalue of the partially transposed reduced density operator. A separable state has $N = 0$, while for a maximally entangled state, $N = 1$.

5.3 Results

Here, we use the QUAPI method, introduced in detail in chapter 3 [21,9] to calculate the time-dependent reduced density matrix of the system. To be specific, we address entanglement between two chromophore pairs under the influence of a slow bath. We consider two equal pairs described by $\sigma_{x/z,i}$, coupled by an interpair Förster interaction J and coupled to a harmonic bath. The total Hamiltonian reads

$$\begin{aligned} H_2 &= \sum_{i=1,2} \frac{\hbar\Delta}{2}\sigma_{x,i} + \hbar J(\sigma_{x,1}\sigma_{x,2} + \sigma_{y,1}\sigma_{y,2}) \\ &\quad + \frac{\hbar}{2}(\sigma_{z,1} + \sigma_{z,2}) \sum_\kappa \tilde{c}_\kappa (b^\dagger_\kappa + b_\kappa) + \sum_\kappa \hbar\omega_\kappa b^\dagger_\kappa b_\kappa, \end{aligned} \tag{5.6}$$

whose basis refers to the states $\{|\uparrow_1\rangle = |e_1 g_2\rangle, |\downarrow_1\rangle = |g_1 e_2\rangle, |\uparrow_2\rangle = |e_3 g_4\rangle, |\downarrow_2\rangle = |g_3 e_4\rangle\}$. As before, the bath spectral density follows from a Debye dielectric model, again yielding the Ohmic form. The time-dependent reduced density matrix $\rho(t)$ is computed using an adapted QUAPI scheme. Fig. 5.1 shows the time-evolution of the populations $p_{\uparrow\uparrow}(t) = p_{\downarrow\downarrow}(t)$ and $p_{\uparrow\downarrow}(t) = p_{\downarrow\uparrow}(t)$ of the four basis states for different values of ω_c for the initial preparation $|\psi_0\rangle = (|\uparrow_1\downarrow_2\rangle + |\downarrow_1\uparrow_2\rangle)/\sqrt{2}$. After a transient oscillatory behavior, the stationary equilibrium values are reached. The corresponding decay occurs on shorter times for large ω_c, i.e., fast baths, compared to the rather slow decay for small ω_c.

Fig. 5.2(a) shows the time evolution of $N(t)$ for two different values $\omega_c = \Delta$, and $\omega_c = 50\Delta$, for the maximally entangled initial state $|\psi_0\rangle$. Starting from $N(0) = 1$

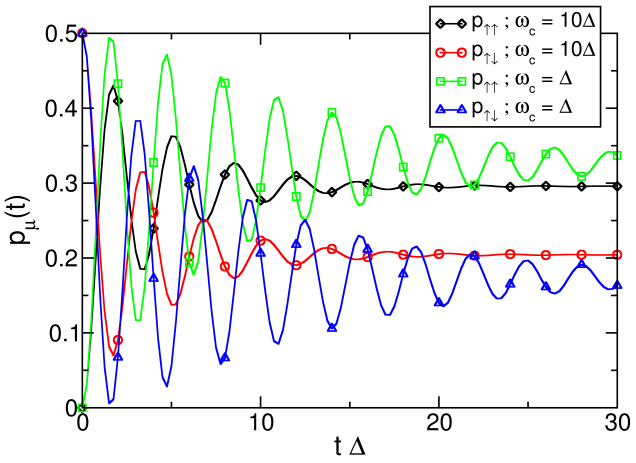

Figure 5.1: Time evolution of the populations $p_\mu(t)$ for two coupled chromophore pairs. This illustrates the action of a slow ($\omega_c = \Delta$) and a fast ($\omega_c = 10\Delta$) bath, for $k_BT = 0.1\hbar\Delta$, $\alpha = 0.1$, and for interpair Förster coupling $J = 0.1\Delta$.

we observe a decay to zero with small oscillations superimposed. For the Markovian bath $\omega_c = 50\Delta$, the decay occurs faster than for the non-Markovian bath $\omega_c = \Delta$ indicating that entanglement survives on a longer time scale for the slow bath as compared to the fast bath. For a larger interpair coupling $J = \Delta$, the superimposed oscillations are more pronounced (fig. 5.2(a) inset) which is due to constructive interference of the involved transitions within the chromophore system. For a quantitative picture, we fit an exponential $N(t) = N_0 \exp(-\Gamma t) + N_1$ with a decay constant Γ which contains the influence of the bath. Fig. 5.2(b) shows the dependence of Γ on ω_c. Clearly, Γ strongly decreases for small ω_c, while for large ω_c, the rate constant saturates. The dependence of Γ on ω_c is more pronounced for larger values of α. This nicely illustrates that entanglement is much more robust in biomolecular systems compared to other macroscopic condensed-matter devices [110] which display quantum coherent behavior.

To study the cross-over between fast and slow baths, we show $N(t)$ for varying ω_c in fig. 5.3 for the initial state $|\psi_1\rangle = |\uparrow_1\uparrow_2\rangle$. Fig. 5.3(a) shows the result for $J = 0.1\Delta$. The entanglement is rather quickly destroyed in the regime $\omega_c \gg \Delta$. On the other hand, we find a regular oscillatory decay for $0.1\Delta \lesssim \omega_c \lesssim \Delta$. In this regime, complete entanglement disappearance and revivals alternate. The time scale of the entanglement oscillations is given by $2\pi/J$. The constructive role of a sluggish bath is further illustrated in the inset of fig. 5.3(a), where $N(t)$ is shown for $J = 0$. In fact, in the regime $\omega_c < \Delta$, we find that entanglement between the two pairs is generated by their common interaction with a sluggish bath. Most interestingly, for $\omega_c = 0.1\Delta$, $N(t)$ steadily grows even over rather long times up to $t\Delta = 500$.

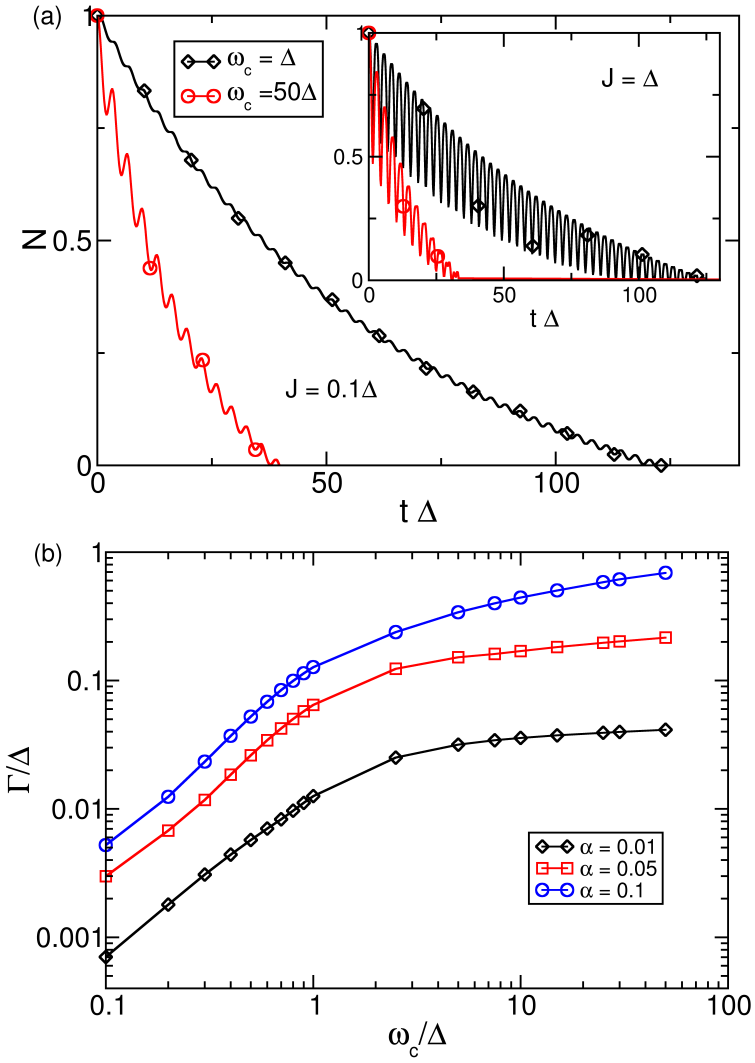

Figure 5.2: (a) Time evolution of the negativity $N(t)$ for the cut-off frequencies $\omega_c = \Delta$ (black) and $\omega_c = 50\Delta$ (red) for the interpair Förster coupling $J = 0.1\Delta$ (main) and $J = \Delta$ (inset). Moreover, $k_BT = 0.1\hbar\Delta$. (b) Decay constant Γ as a function of the cut-off frequency ω_c for different values of α for $k_BT = 0.1\hbar\Delta$, $J = 0.1\Delta$.

In view of the single-pair results described above, this seems counterintuitive since for small ω_c, a reduced influence of the bath modes would be expected. However, in this regime, the bath is rather efficient in generating entanglement. This feature survives even for larger values of α, see fig. 5.3(b). The oscillatory behavior of the entanglement generation still occurs for $J = 0.1\Delta$, where $N(t)$ assumes all values between zero and one. The bath-induced destruction happens here earlier due to the large α. Entanglement is also produced when $J = 0$, see inset of fig. 5.3(b), for $0.1\Delta \lesssim \omega_c \lesssim \Delta$. Also here, $N(t)$ can even reach the maximal value at intermediate times.

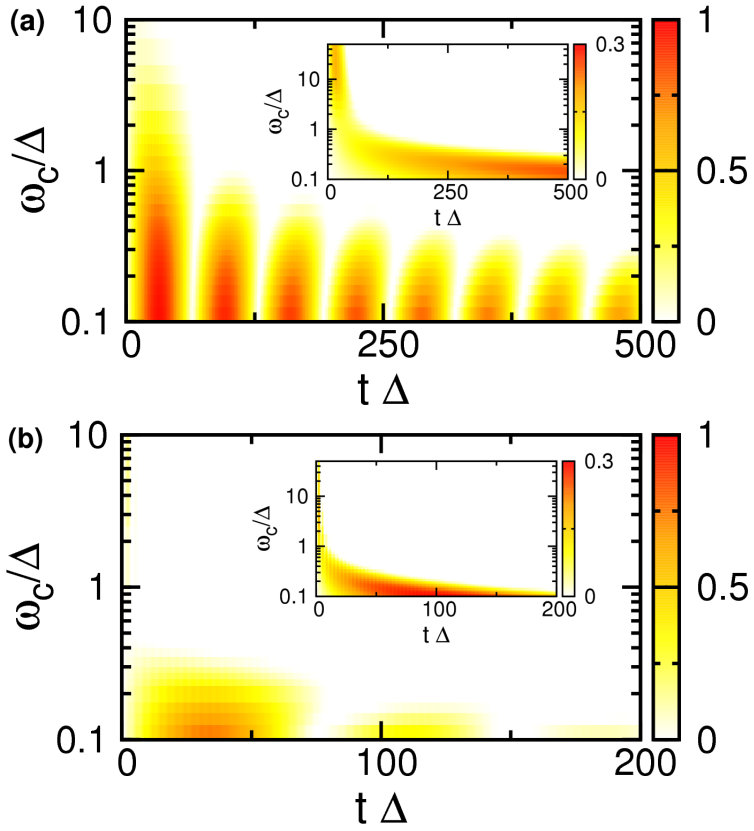

Figure 5.3: (a) Negativity $N(t)$ as a function of ω_c for $J = 0.1\Delta$ (main) and $J = 0$ (inset), for $\alpha = 0.01$ and $k_BT = 0.1\hbar\Delta$. (b) Same as in (a), but for the strong coupling case $\alpha = 0.1$.

So far, we have studied not so high temperatures, similar to the experimental conditions in refs. [23, 24]. However, in fig. 5.4(a) (main) we plot $N(t)$ for varying ω_c, for $k_BT = \hbar\Delta$, for the initial state $|\psi_1\rangle$. We still find large entanglement oscillations at short to intermediate times, for $0.1\Delta \lesssim \omega_c \lesssim \Delta$ despite the rather large temperature: this is an outstanding hardware feature that could provide a useful resource for the artificial design of controlled, robust, and efficient biomolecular nanostructures for quantum information processing [128, 129, 32, 6].

Furthermore, we have varied the initial preparation to the state $|\psi_2\rangle = a|\uparrow_1\downarrow_2\rangle + b|\downarrow_1\uparrow_2\rangle$ with $a^2 + b^2 = 1$. The inset of fig. 5.4(a) shows $N(t)$ for varying a^2 and $J = 0.1\Delta$. $|\psi_2\rangle$ is maximally entangled for $a^2 = 1/2$, for which $N(t)$ decays monotonously with time, while away from this region the negativity again shows collapses and revivals. For the borders $a^2 \to 0, 1$, $|\psi_2\rangle$ is a separable state, but entanglement is rather quickly generated with time before it finally dies out. Robust entanglement thus depends on the initial preparation and is favored by the choice of initially separable (or weakly entangled) states.

Finally, we analyze the dependence on the interpair coupling J. The negativity $N(t)$ is shown in fig. 5.4(b) for varying J for the respective ground state as the initial

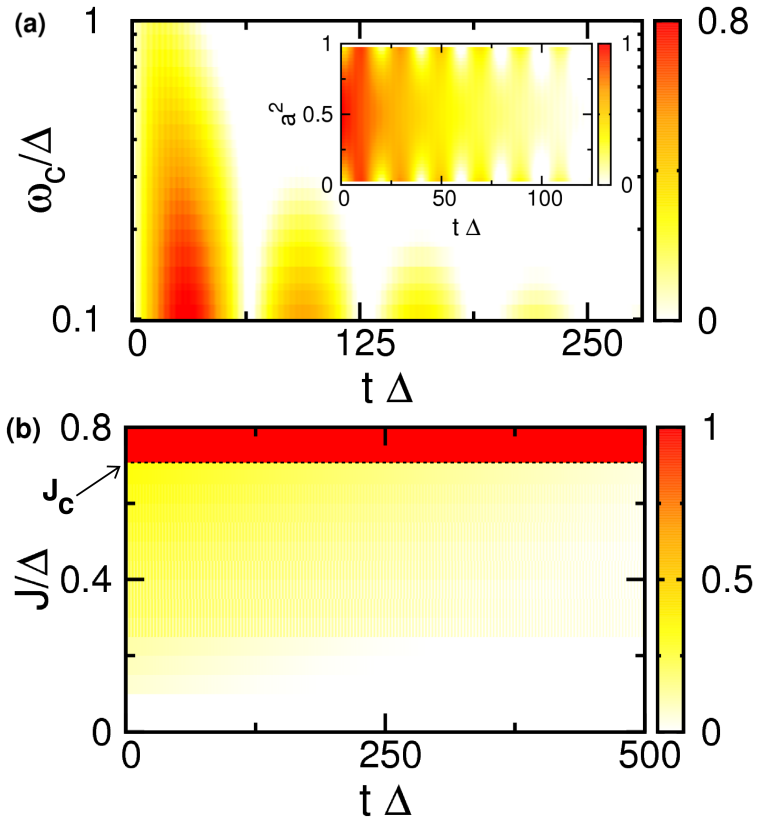

Figure 5.4: Excitonic entanglement robustness: (a) Negativity $N(t)$ for varying ω_c; $J = 0.1\Delta, \alpha = 0.01$ and $k_BT = \hbar\Delta$ (Main). Inset: $N(t)$ for different weights in the initial preparation $|\psi_2\rangle = a|\uparrow_1\downarrow_2\rangle + b|\downarrow_1\uparrow_2\rangle$, for $J = 0.1\Delta, \alpha = 0.01, k_BT = 0.1\hbar\Delta$, and $\omega_c = \Delta$. (b) $N(t)$ for varying J; $\alpha = 0.01, k_BT = 0.1\hbar\Delta, \omega_c = 0.1\Delta$. The horizontal line marks the critical value $J_c = 1/\sqrt{2}$ above which the initially prepared ground state belongs to a DFS.

preparation. From eq. (5.6) it follows that a critical value $J_c = 1/\sqrt{2}$ exists such that for $J \geq J_c$, the state $|\psi_g\rangle = (|\uparrow_1\downarrow_2\rangle - |\downarrow_1\uparrow_2\rangle)/\sqrt{2}$ is the two-pair groundstate, which, however, belongs to a decoherence-free subspace (DFS) of H_2 [27]. Hence, $N(t)$ remains constantly maximal. For $J < J_c$, the ground state has some weight outside of the DFS and hence suffers from decoherence.

The general nature of our results demonstrate that pure quantum mechanical effects provide the conditions for efficient light harvesting and therefore that the evolutionary process has led to a robust, ultrafast yet efficient quantum rule for photosynthetic processing. The results reported here are of direct relevance to quantum dot and molecular architectures [130, 131]. They could prove crucial in the design of artificial efficient light harvesters for robust multipartite biomolecular entanglement, with enhanced energy transfer rates [132] for the control and conditional dynamics [32, 6] of quantum bits.

Chapter 6

Iterative real-time path integral approach to nonequilibrium quantum transport

With the previous chapter we end with the investigations of the real-time dynamics of quantum system subjected to a bosonic environment. In the remainder of the thesis we aim for addressing the real-time dynamics of a quantum system subjected to a fermionic environment. In the preceding chapters the QUAPI scheme has turned out to be a most successful method for including non-Markovian features within the bosonic real-time dynamics of open quantum systems up to a certain memory time. This feature was the motivation to develop a new scheme for the real-time dynamics of fermionic quantum systems, which is rooted upon the fact that for finite temperatures the time non-local correlations decay exponentially in time, which is a common feature for bosonic *and* fermionic quantum systems. Since we are now concerned with a fermionic environment there are clearly conceptual differences which are the reason for the main difference between the QUAPI scheme and our newly developed scheme. These differences will be discussed in detail in the sequel.

We have developed a numerical approach to compute real-time path integral expressions for quantum transport problems out of equilibrium. The scheme is based on a deterministic iterative summation of the path integral (ISPI) for the generating function of the nonequilibrium current. Self-energies due to the leads, being non-local in time, are fully taken into account within a finite memory time, thereby including non-Markovian effects, and numerical results are extrapolated both to vanishing (Trotter) time discretization and to infinite memory time. This extrapolation scheme converges except at very low temperatures, and the results are then numerically exact. The method is applied to nonequilibrium transport through an Anderson dot. Throughout this chapter, we set $\hbar = k_B = 1$.

6.1 Model

We consider the Anderson model [76] given by the Hamiltonian

$$\begin{aligned}\mathcal{H} &= H_{dot} + H_{leads} + H_T \\ &= \sum_\sigma E_{0\sigma}\hat{n}_\sigma + U\hat{n}_\uparrow\hat{n}_\downarrow + \sum_{kp\sigma}(\epsilon_{kp}-\mu_p)c^\dagger_{kp\sigma}c_{kp\sigma} \\ &\quad -\sum_{kp\sigma}\left[t_p c^\dagger_{kp\sigma}d_\sigma + h.c.\right]. \end{aligned} \tag{6.1}$$

Here, $E_{0\sigma} = E_0 + \sigma B$ with $\sigma = \uparrow, \downarrow = \pm$ is the energy of a single electron with spin σ on the isolated dot, which can be varied by tuning a back gate voltage or a Zeeman magnetic field term $\propto B$. The latter is assumed not to affect the electron dispersion in the leads. The corresponding dot electron annihilation/creation operator is $d_\sigma/d^\dagger_\sigma$, with $\hat{n}_\sigma \equiv d^\dagger_\sigma d_\sigma$ with eigenvalues $n_\sigma = 0, 1$, and U denotes the on-dot interaction. For later purpose, it is convenient to use the operator identity $\hat{n}_\uparrow\hat{n}_\downarrow = \frac{1}{2}(\hat{n}_\uparrow + \hat{n}_\downarrow) - \frac{1}{2}(\hat{n}_\uparrow - \hat{n}_\downarrow)^2$, thereby introducing the shifted single-particle energies $\epsilon_{0\sigma} \equiv E_{0\sigma} + U/2$, which yields the equivalent dot Hamiltonian

$$H_{dot} = H_{dot,0} + H_U = \sum_\sigma \epsilon_{0\sigma}\hat{n}_\sigma - \frac{U}{2}(\hat{n}_\uparrow - \hat{n}_\downarrow)^2. \tag{6.2}$$

In eq. (6.1), ϵ_{kp} denotes the energies of the noninteracting electrons (operators $c_{kp\sigma}$) in lead $p = L/R = \pm$, with chemical potential $\mu_p = peV/2$. Dot and leads are connected by the tunnel couplings t_p. The observable of interest is the (symmetrized) tunneling current $I = (I_L - I_R)/2$,

$$I(t) = -\frac{ie}{2}\sum_{kp\sigma}\left[pt_p\langle c^\dagger_{kp\sigma}d_\sigma\rangle_t - pt^*_p\langle d^\dagger_\sigma c_{kp\sigma}\rangle_t\right], \tag{6.3}$$

where $I_p(t) = -e\dot{N}_p(t)$ with $N_p(t) = \langle\sum_{k\sigma} c^\dagger_{kp\sigma}c_{kp\sigma}\rangle_t$. The stationary steady-state dc current follows as the asymptotic long-time limit, $I = \lim_{t\to\infty} I(t)$. We have explicitly confirmed that current conservation, $I_L + I_R = 0$, is numerically fulfilled for the ISPI scheme.

6.1.1 Keldysh technique

In the presence of a finite bias voltage, $V \neq 0$, the Keldysh technique [133, 134, 135, 136] which will be outlined shortly in the sequel, provides a way to study nonequilibrium transport. In nonequilibrium one is concerned with the fact that starting from an arbitrary nonequilibrium state and then switching on and off interactions the system will evolve to some unpredictable state. In general, the latter depends on the peculiarities of the switching procedure. Thus it is desired to build up a formalism that avoids references to the state at $t = \infty$. The main idea of the Keldysh/Schwinger technique is to take the final state to be exactly the same as

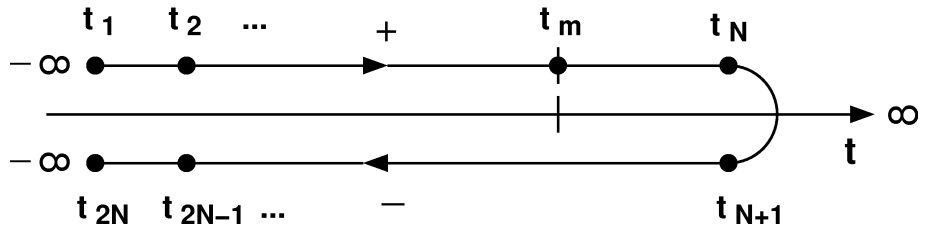

Figure 6.1: Keldysh contour: every physical time has two contour representatives on the branches $\pm$. The measurement time t_m only has a single representative on the upper branch.

the initial state. The crucial point is to let the quantum system evolve from some initial state at $t = -\infty$ and switch on the interaction. Then the system evolves in the forward time direction and evolves back in the opposite direction. To realize this idea, the time axis is extended to a contour with $\alpha = \pm$ branches, see fig. 6.1. Consequently, the evolution operator $U_{t,t'} \equiv \exp[-iH(t-t')]$ along such a closed contour is always unity

$$U_C \equiv 1\,. \tag{6.4}$$

This is directly related to what has been mentioned within the introduction to the QUAPI method in section 3.3. There, the $q^{\pm}$ correspond to fields residing on the upper and lower part of the Keldysh contour respectively, see fig. 3.4. Note that there is no switching of interactions in the future. Both switching procedures take place in the past: switching on of the interactions at the forward branch and switching off the interactions at the backward branch of the contour respectively. In that sense, interactions are treated adiabatically along this time evolution. At every moment of time one has to specify a field residing on both time branches of the contour which goes along with an effective doubling of fields. The Keldysh GF is

$$G_{ij}^{\alpha\beta}(t_\alpha, t'_\beta) = -i\langle \mathcal{T}_C[\psi_i(t_\alpha)\psi_j^\dagger(t'_\beta)]\rangle\,, \tag{6.5}$$

where $\mathcal{T}_C$ denotes the contour ordering of times along the Keldysh contour, and $i, j = L, R, 0$ correspond to the fields of the problem of interest. In the case of the Anderson model studied in the following, they represent lead or dot fermions, respectively. We omit the spin indices here, remembering that for the remainder of this chapter each entry still is a diagonal 2×2 matrix in spin space. The explicit form of the four Keldysh components is given by [137]:

1. $t = t_+$ and $t' = t_+$

$$G_{i,j}^{++}(t,t') = -i\langle \mathcal{T}_C[\psi_i(t)\psi_j^\dagger(t')]\rangle = -i\langle \mathcal{T}[\psi_i(t)\psi_j^\dagger(t')]\rangle\,, \tag{6.6}$$

where $\mathcal{T}$ is the time ordering operator on the physical time axis. Both time arguments reside on the upper branch of the Keldysh contour, and G^{++} is just the conventional causal Green's function along the physical time axis.

2. $t = t_+ \quad \text{and} \quad t' = t_-$

$$G^{+-}_{i,j}(t,t') = i\langle[\psi^\dagger_j(t')\psi_i(t)]\rangle\,. \tag{6.7}$$

Here, one has to take into account that a time in the lower branch has to be considered as intrinsically in the future towards one in the upper branch. This Green's function plays a central role in non-equilibrium theory because at equal time arguments it is related to the electronic distribution function out of equilibrium.

3. $t = t_- \quad \text{and} \quad t' = t_+$

$$G^{-+}_{i,j}(t,t') = -i\langle[\psi_i(t)\psi^\dagger_j(t')]\rangle\,. \tag{6.8}$$

This function is clearly closely related to the function G^{+-}.

4. $t = t_- \quad \text{and} \quad t' = t_-$

$$G^{--}_{i,j}(t,t') = -i\langle\overline{\mathcal{T}}[\psi_i(t)\psi^\dagger_j(t')]\rangle\,. \tag{6.9}$$

In this last case both times are in the lower branch, but since the contour ordering operator $\mathcal{T}_C$ orders the times in the opposite sense one finds the standard Greenś function but with the time arguments ordered in reverse order (anti-causal ordering).

Usually the four Keldysh components are expressed in matrix form

$$G = \begin{pmatrix} G^{++} & G^{+-} \\ G^{-+} & G^{--} \end{pmatrix} \tag{6.10}$$

and in general, the four components are linearly dependent, such that $G^{++} + G^{--} = G^{+-} + G^{-+}$. However, the commonly used Keldysh rotation [136,135] seems to offer no advantages here, and is not employed in what follows.

6.1.2 Fermionic coherent state path integral

The ISPI scheme is build on an evaluation of a fermionic coherent state path integral which we will introduce in the sequel, following [87].

For a general many-particle Hamiltonian in second quantized normal ordered form the functional integral representation for the many-body evolution operator may be obtained using a coherent state representation rather than the position and momentum eigenstates for the Feynman path integral [87]. Since the eigenvalue of Fermions anticommute one has to introduce anticommuting variables called Grassmann variables. A Grassmann algebra $\mathcal{G}$ is defined by associating a generator ξ_α with each annihilation operator a_α and a generator ξ^*_α with each creation operator $a^\dagger_\alpha$. These generators anticommute

$$\xi_\alpha\xi_\beta + \xi_\beta\xi_\alpha = 0 \tag{6.11}$$

and consequently $\xi_\alpha^2 = 0$ (α and β are any quantum numbers). For details of the differentiation and integration rules of Grassmann variables, see [87]. Note that the fermionic coherent states belong to a generalized Fock space, but any physical Fermion state of an ordinary Fock space can be expanded in terms of these coherent states. In order to deal with expressions containing combinations of Grassmann variables and creation and destruction operators, it is necessary to augment the definition of Grassmann variables to specify the commutation relations between the ξ and the a and the adjoints of mixed expressions. Therefore it is required that [87]

$$[\tilde{\xi}, \tilde{a}]_+ = 0 \qquad \text{and} \qquad (\tilde{\xi}\tilde{a})^\dagger = \tilde{a}^\dagger \xi^* \,, \tag{6.12}$$

where $\tilde{\xi}$ denotes any Grassmann variable in $\{\xi_\alpha, \xi_\alpha^*\}$ and $\tilde{a}$ is any operator in $\{a_\alpha^\dagger, a_\alpha\}$. A Fermion coherent state $|\xi\rangle$ is defined according to

$$|\xi\rangle = e^{-\sum_\alpha \xi_\alpha a_\alpha^\dagger}|0\rangle = \prod_\alpha (1 - \xi_\alpha a_\alpha^\dagger)|0\rangle \tag{6.13}$$

and since the combination $\xi_\alpha a_\alpha^\dagger$ commutes with $\xi_\beta a_\beta^\dagger$ each non-vanishing term of the exponential is reproduced.

To derive the coherent state path integral the time interval of propagation from the initial time t_i to the final time t_f is broken into M steps of size $\epsilon = \frac{t_f - t_i}{M}$ and the closure relation

$$\int \prod_\alpha d\xi_{\alpha,k}^* d\xi_{\alpha,k} e^{-\sum_\alpha \xi_{\alpha,k}^* \xi_{\alpha,k}} |\xi_{\alpha,k}\rangle\langle\xi_{\alpha,k}| = \mathbb{1} \tag{6.14}$$

is inserted at the k^{th} time step, where the end points are denoted as $\xi_{\alpha,0} \equiv \xi_{\alpha,i}$ and $\xi_{\alpha,M} \equiv \xi_{\alpha,f}$. Assuming that the Hamiltonian is written in normal ordered form and with use of

$$\langle\xi|A(a_\alpha^\dagger, a_\alpha)|\xi'\rangle = e^{\sum_\alpha \xi_\alpha^* \xi_\alpha'} A(\xi_\alpha^*, \xi_\alpha') \tag{6.15}$$

for the matrix element of a normal ordered operator between two coherent states, the matrix elements of the time evolution operator may be written as [87]

$$\begin{aligned} U(\xi_{\alpha,f}^* t_f; \xi_{\alpha,i} t_i) &= \lim_{M\to\infty} \langle\xi_f| e^{-\frac{i}{\hbar} H(t_f - t_i)} |\xi_i\rangle \\ &= \lim_{M\to\infty} \int \prod_{k=1}^{M-1} \prod_\alpha d\xi_{\alpha,k}^* d\xi_{\alpha,k} e^{-\sum_\alpha \sum_{k=1}^{M-1} \xi_{\alpha,k}^* \xi_{\alpha,k}} \\ &\quad \times e^{\sum_{k=1}^{M} \left(\sum_\alpha \xi_{\alpha,k}^*, \xi_{\alpha,k-1} - \frac{i\epsilon}{\hbar} H(\xi_{\alpha,k}^*, \xi_{\alpha,k-1}) \right)} \,. \end{aligned} \tag{6.16}$$

For reason of comparison with the Feynman path integral from section 2.5 we explicitly include $\hbar$ here. In the case of a Fermions all the integrals are bound since there is no metric in the Grassmann algebra. It is convenient to introduce the so-called trajectory notation

$$\xi_{\alpha,k}^* \frac{\xi_{\alpha,k} - \xi_{\alpha,k-1}}{\epsilon} \equiv \xi_\alpha^*(t) \frac{\partial}{\partial t} \xi_\alpha(t) \tag{6.17}$$

and

$$H(\xi^*_{\alpha,k}, \xi_{\alpha,k-1}) \equiv H(\xi^*_\alpha(t), \xi_\alpha(t))\,, \tag{6.18}$$

where the trajectory $\xi_\alpha(t)$ represents the set $\{\xi_{\alpha,1}, \xi_{\alpha,2}, \cdots, \xi_{\alpha,M}\}$. Hence, the time evolution operator is rewritten as

$$\begin{aligned} U(\xi^*_{\alpha,f} t_f; \xi_{\alpha,i} t_i) \;\; = \;\; & \int_{\xi_\alpha(t_i)=\xi_{\alpha,i}}^{\xi^*_\alpha(t_f)=\xi^*_{\alpha,f}} \mathcal{D}[\xi^*_\alpha(t)\xi_\alpha(t)] e^{\sum_\alpha \xi^*_\alpha(t_f)\xi_\alpha(t_f)} \\ & \times e^{\frac{i}{\hbar}\int_{t_i}^{t_f} dt \left[\sum_\alpha i\hbar \xi^*_\alpha(t) \frac{\partial \xi_\alpha(t)}{\partial t} - H(\xi^*_\alpha(t), \xi_\alpha(t))\right]}\,, \end{aligned} \tag{6.19}$$

with

$$\int_{\xi_\alpha(t_i)}^{\xi^*_\alpha(t_f)} \mathcal{D}[\xi^*_\alpha(t)\xi_\alpha(t)] = \lim_{M\to\infty} \int \prod_{k=1}^{M-1} \prod_\alpha d\xi^*_{\alpha,k} d\xi_{\alpha,k}\,. \tag{6.20}$$

Note that one significant difference between the coherent state functional integral (6.19) and the Feynman path integral introduced in eq. (2.31) is the dependence upon $\hbar$. In the Feynman case, eq. (2.31), $\frac{1}{\hbar}$ appears as a constant multiplying the entire exponent, so that the stationary phase expansion immediately yields the classical limit, see section 2.5. In the present case, the action contains $\hbar$ within the Lagrangian (the second exponent in eq. (6.19)) as well as a multiplicative factor, so that the stationary phase method yields a result quite distinct from the classical limit [87].

Using the expression for the trace of an operator A

$$\mathrm{tr}\, A = \int \prod_\alpha d\xi^*_\alpha d\xi_\alpha e^{-\sum_\alpha \xi^*_\alpha \xi_\alpha} \langle -\xi | A | \xi \rangle \tag{6.21}$$

and units such that again $\hbar = 1$ the grand-canonical partition function maybe written as

$$Z = \mathrm{tr}\, e^{-\beta(H-\mu N)} = \int \prod_\alpha d\xi^*_\alpha d\xi_\alpha e^{-\sum_\alpha \xi^*_\alpha \xi_\alpha} \langle -\xi | e^{-\beta(H-\mu N)} | \xi \rangle \tag{6.22}$$

which yields with antiperiodic boundary conditions [87]

$$Z = \int \mathcal{D}[\xi^*(t); \xi(t)] e^{iS(\xi^*, \xi)} \tag{6.23}$$

with S being the action corresponding to the Hamiltonian H.

To elucidate further the connection of the Keldysh technique described in the previous subsection and the fermionic coherent state path integral the ISPI scheme is based on, we give the example of the free Fermion Keldysh action, following ref. [136]. Therefore, consider a single quantum state with energy ϵ_0, populated by spinless Fermions. The Hamiltonian of such a system is the Hamiltonian (6.1) with $U = 0$ and $t_p = 0$, thus

$$H = \epsilon_0 d^\dagger d\,. \tag{6.24}$$

The partition function is defined as

$$Z = \frac{\operatorname{tr} \rho U_C}{\operatorname{tr} \rho} \tag{6.25}$$

with the time evolution operator (6.4) along the Keldysh contour C. The trace of the equilibrium density matrix is $\operatorname{tr} \rho = 1 + \rho(\epsilon_0)$, where the two terms stand for the empty and the singly occupied state. Now, one divides the Keldysh contour into $2N-2$ time steps of length δt and introduced the closure relation (6.14) in the $2N$ points along the contour yields

$$Z = \frac{1}{\operatorname{tr} \rho} \int \int \prod_{j=1}^{2N} [d\xi_j^*; d\xi_j] e^{i \sum_{j,j'}^{2N} \xi_j^* G^{-1}_{j,j'} \xi_{j'}} \,. \tag{6.26}$$

The $2N \times 2N$ matrix $G^{-1}_{j,j'}$ is given by

$$i\, G^{-1}_{jj'} \equiv \left(\begin{array}{ccc|ccc} -1 & & & & & -\rho(\epsilon_0) \\ 1-h & -1 & & & & \\ & 1-h & -1 & & & \\ \hline & & 1 & -1 & & \\ & & & 1+h & -1 & \\ & & & & 1+h & -1 \end{array} \right) , \tag{6.27}$$

and $h \equiv i\epsilon_0 \delta t$. Note that the upper right element of the matrix is crucial to maintain the correct normalization $Z = 1$. Using the fact that the fermionic Gaussian integral is given by its determinant of the correlation matrix one finds

$$Z = \frac{\det\left(i\, G^{-1}\right)}{\operatorname{tr}(\rho)} = 1 \tag{6.28}$$

as expected. Taking now the continuous limit $N \to \infty$ and using the trajectory notation one arrives at

$$Z = \int \mathcal{D}[\xi^*(t); \xi(t)] e^{i \int_C dt\, \xi^*(t) G^{-1} \xi(t)} = \int \mathcal{D}[\xi^*(t); \xi(t)] e^{iS(\xi^*(t), \xi(t))} \tag{6.29}$$

which is equivalent to eq. (6.23) including in addition the full Keldysh structure.

6.2 Generating function

Let us then discuss the generating function, which contains all relevant information about the physics of the system. First, we want to integrate out the lead fermion fields, and, in addition, perform a discrete Hubbard-Stratonovich transformation. This allows to integrate out the dot fields as well, and we are then left with a

discrete path summation. We start with the fermionic path-integral representation of the generating function,

$$Z[\eta] = \int \mathcal{D}\left[\prod_{\sigma} \bar{d}_\sigma, d_\sigma, \bar{c}_{kp\sigma}, c_{kp\sigma}\right] e^{iS[\bar{d}_\sigma, d_\sigma, \bar{c}_{kp\sigma}, c_{kp\sigma}]}, \tag{6.30}$$

with Grassmann fields $(\bar{d}, d, \bar{c}, c)$ (Note that we use the same symbols for fermion operators and Grassmann fields throughout the paper for better readability). We introduce an external source term S_η (defined below in eq. (6.32)), which allows to compute the current at measurement time t_m,

$$I(t_m) = i\frac{\partial}{\partial \eta} \ln Z[\eta]\Big|_{\eta=0}. \tag{6.31}$$

We note in passing that it is also possible to evaluate other observables, e.g., the zero-frequency noise, by introducing appropriate source terms and performing the corresponding derivatives. The action is $S = S_{dot} + S_{leads} + S_T + S_\eta$, where

$$\begin{aligned}
S_{dot} &= S_{dot,0} + S_U \\
&= \int_C dt \left[\sum_\sigma \bar{d}_\sigma \left(i\partial_t - \epsilon_{0\sigma}\right) d_\sigma + \frac{U}{2}(n_\uparrow - n_\downarrow)^2\right], \\
S_{leads} &= \int_C dt \sum_{kp\sigma} \bar{c}_{kp\sigma}(i\partial_t - \epsilon_{kp} + \mu_p) c_{kp\sigma}, \\
S_T &= \int_C dt \sum_{kp\sigma} t_p \bar{c}_{kp\sigma} d_\sigma + h.c., \\
S_\eta &= \frac{ie\eta}{2} \sum_{kp\sigma} p(t_p \bar{c}_{kp\sigma} d_\sigma - t_p^* \bar{d}_\sigma c_{kp\sigma})(t_m).
\end{aligned} \tag{6.32}$$

The interaction term S_U in eq. (6.32) does not allow to directly perform the functional integration. Apart from this, all other terms are quadratic in the Grassmann fields and thus define the 'noninteracting' (quadratic) part. Note that the level shift $+U/2$ is here included in the noninteracting sector.

6.2.1 Noninteracting part

Before turning to the interacting problem, we briefly discuss the Keldysh GF of the noninteracting problem. Let us first integrate out the lead degrees of freedom. We remain with an effective action for the dot, which is non-local in time due to the presence of the leads. In particular, after Gaussian integration, the generating function reads

$$Z_{ni}[\eta] = \int \mathcal{D}\left[\prod_\sigma \bar{d}_\sigma, d_\sigma\right] e^{i(S_{dot,0} + S_{env})} \tag{6.33}$$

with

$$\begin{aligned} S_{env} &= \int_C dt \int_C dt' \sum_\sigma \bar{d}_\sigma(t) \Big\{ \gamma_L(t,t') + \gamma_R(t,t') \\ &+ \frac{ie\eta}{2}[\gamma_L(t,t') - \gamma_R(t,t')] \\ &\times [\delta(t-t_m) + \delta(t'-t_m)] \Big\} d_\sigma(t'). \end{aligned} \tag{6.34}$$

For the source term, the physical measurement time t_m can be taken at one branch of the contour, see fig. 6.1. As we fix t_m on the upper $(+)$ branch, the $(--)$ Keldysh element of the source term self-energy vanishes, see the time-discretized version below. The γ_p in eq. (6.34) represent the leads, and their Fourier transforms are explicitly given as 2×2 Keldysh matrices,

$$\gamma_p(\omega) = i\Gamma_p \begin{pmatrix} 2f(\omega-\mu_p) - 1 & -2f(\omega-\mu_p) \\ 2 - 2f(\omega-\mu_p) & 2f(\omega-\mu_p) - 1 \end{pmatrix}. \tag{6.35}$$

Here, we have used the fact that the leads are in thermal equilibrium, $f(\omega) = 1/(e^{\omega/T}+1)$. Moreover, we take the standard wide-band limit, with a constant density of states per spin channel around the Fermi energy, $\rho(\epsilon_F)$, yielding the hybridization $\Gamma_p = \pi\rho(\epsilon_F)|t_p|^2$ of the dot level with lead p. For the sake of clarity, we assume from now on symmetric contacts, $\Gamma_L = \Gamma_R \equiv \Gamma/2$. The generalization to asymmetric contacts is straightforward. In the next step, still for $U = 0$, we may also integrate over the dot degrees of freedom. We obtain the noninteracting generating function

$$Z_{ni}[\eta] = \prod_\sigma \det\left[-iG_{0\sigma}^{-1}(t,t') + \eta\Sigma^J(t,t')\right], \tag{6.36}$$

where $G_{0\sigma}^{-1}(t,t')$ follows from

$$\begin{aligned} G_{0\sigma}(\omega) &= [(\omega-\epsilon_{0\sigma})\tau_z - \gamma_L(\omega) - \gamma_R(\omega)]^{-1} \\ &= \frac{1}{\Gamma^2 + (\omega-\epsilon_{0\sigma})^2} \\ &\times \begin{pmatrix} \omega - \epsilon_{0\sigma} + i\Gamma(F-1) & i\Gamma F \\ i\Gamma(F-2) & -\omega + \epsilon_{0\sigma} + i\Gamma(F-1) \end{pmatrix} \end{aligned} \tag{6.37}$$

where τ_z is the standard Pauli matrix in Keldysh space, and $F = f(\omega + eV/2) + f(\omega - eV/2)$. Moreover, the self-energy for the source term is obtained as

$$\begin{aligned} \Sigma^J(t,t') &= \frac{e}{2}[\gamma_L(t,t') - \gamma_R(t,t')] \\ &\times [\delta(t-t_m) + \delta(t'-t_m)]. \end{aligned} \tag{6.38}$$

Up to this point, we have discussed the noninteracting case. In order to treat interactions, we now perform a Hubbard-Stratonovich transformation.

6.2.2 Hubbard-Stratonovich transformation

Let us therefore turn back to the real-time action S_{dot} of the dot in the presence of interactions, $U \neq 0$, see eq. (6.32). For later numerical purpose, it is beneficial to proceed with the discussion in the time-discretized representation of the path integral [87]. In order to decouple the quartic term, we discretize the full time interval, $t = N\delta_t$, with the time increment δ_t. On each time slice, we perform a Trotter breakup of the dot propagator according to $e^{i\delta_t(H_0+H_T)} = e^{i\delta_t H_T/2} e^{i\delta_t H_0} e^{i\delta_t H_T/2} + O(\delta_t^2)$, where $H_0 = H_{dot} + H_{leads}$. By this, we introduce a Trotter error [138, 139, 10] which, however, will be eliminated in the same spirit as within the QUAPI method, see section 3.3, from the results in a systematic way [103], see below. Next, we use a discrete Hubbard-Stratonovich (HS) transformation [139,140,141] for the interacting part, which introduces Ising-like discrete spin fields $s_n^{\pm} = (s_n^+, s_n^-)$ on the $\alpha = \pm$ branches of the Keldysh contour (with $s_n^\alpha = \pm 1$) on the n-th Trotter slice. For a given Trotter slice, we now use

$$e^{\pm i\delta_t U(\hat{n}_\uparrow - \hat{n}_\downarrow)^2/2} = \frac{1}{2} \sum_{s^\pm = \pm} e^{-\delta_t \lambda_\pm s^\pm (\hat{n}_\uparrow - \hat{n}_\downarrow)}. \tag{6.39}$$

For $U > 0$, noting that $n_\uparrow - n_\downarrow = 0, \pm 1$, the sum can be carried out and gives the condition

$$\cosh(\delta_t \lambda_\pm) = \cos(\delta_t U/2) \pm i \sin(\delta_t U/2).$$

The solution is $\lambda_\pm = \lambda' \pm i\lambda''$ with

$$\delta_t \lambda' = \sinh^{-1} \sqrt{\sin(\delta_t U/2)}, \;\; \delta_t \lambda'' = \sin^{-1} \sqrt{\sin(\delta_t U/2)}. \tag{6.40}$$

Note that the overall sign of $\lambda_\pm$ is chosen arbitrarily, but does not influence the physical result. Uniqueness of this HS transformation requires $U\delta_t < \pi$. To ensure sufficiently small time discretizations, in all calculations one should then obey the condition $\max(U, e|V|, |\epsilon_0|, T) \lesssim 1/\delta_t$.

6.2.3 Total GF and generating function

After the HS transformation, the remaining fermionic Grassmann variables $(\bar{d}_\sigma, d_\sigma)$ can be integrated out at the cost of the path summation over the HS Ising spins $\{s\}$,

$$Z[\eta] = \sum_{\{s\}} \prod_\sigma \det G_\sigma^{-1}[\{s\}, \eta], \tag{6.41}$$

with the total Keldysh GF written in time-discretized ($1 \leq k, l \leq N$) form as

$$\left(G_\sigma^{-1}\right)_{kl}^{\alpha\beta}[\{s\}, \eta] = \left(G_{0\sigma}^{-1}\right)_{kl}^{\alpha\beta} + i\eta \Sigma_{kl}^{J,\alpha\beta} - i\delta_t \delta_{kl} \lambda_\alpha s_k^\alpha \delta_{\alpha\beta}, \tag{6.42}$$

where $\alpha, \beta = \pm$ labels the Keldysh branches, and the noninteracting GF is

$$G_{0\sigma,kl} = \int_{-\infty}^{\infty} \frac{d\omega}{2\pi} e^{i\delta_t(k-l)\omega} G_{0\sigma}(\omega). \tag{6.43}$$

Note that $G_{0\sigma}(t,t')$ depends only on time differences due to time-translational invariance of the noninteracting part. Moreover, the self-energy kernel stemming from the external source term follows as

$$\Sigma_{kl}^{J,\alpha\beta} = \frac{e}{2}\left[\gamma_{L,kl}^{\alpha\beta} - \gamma_{R,kl}^{\alpha\beta}\right]\left[\delta_{mk}\delta_{\alpha,+} + \delta_{ml}\delta_{\beta,+}\right], \tag{6.44}$$

where $\gamma_{p,kl} = \gamma_p(t_k - t_l)$ and the measurement time is $t_m = m\delta_t$.

Moreover we want to point out that the interacting part in the total Green's function (6.42) is diagonal in the time domain. Following [138] after the HS transformation the resulting fields first reside in the off-diagonal of the corresponding inverse Green's function (similar to the example of a free fermion, see eq. (6.27))

$$\widetilde{G}_\sigma^{-1}[\{s\}] = \begin{pmatrix} 1 & 0 & 0 & \cdots & e^{-\delta t K} e^{V_N^\sigma} \\ -e^{-\delta t K} e^{V_1^\sigma} & 1 & 0 & \cdots & 0 \\ 0 & -e^{-\delta t K} e^{V_2^\sigma} & 1 & 0 & \vdots \\ \vdots & \ddots & & \ddots & \end{pmatrix}. \tag{6.45}$$

Here, K includes the non-interacting parts of the Hamiltonian (6.1) and

$$V_n^\sigma = \lambda\sigma s_n^\pm\,. \tag{6.46}$$

Given now two arbitrary Ising configurations giving rise to V^σ and V'^σ the Green's function obeys the Dyson equation [138]

$$\widetilde{G}'_\sigma = \widetilde{G}_\sigma + (\widetilde{G}_\sigma - \mathbb{1})(e^{V^\sigma - V'^\sigma} - \mathbb{1})\widetilde{G}'_\sigma \tag{6.47}$$

and its transpose

$$\widetilde{G}'_\sigma = \widetilde{G}_\sigma + (\widetilde{G}'_\sigma - \mathbb{1})(\mathbb{1} - e^{-V'^\sigma + V^\sigma})\widetilde{G}_\sigma\,. \tag{6.48}$$

Eqs. (6.47) and (6.48) are most easily established by first solving the Dyson equation for [138]

$$G_\sigma = e^{V^\sigma}\widetilde{G}_\sigma\,, \tag{6.49}$$

i.e.

$$G_\sigma[\{s\}] = \begin{pmatrix} e^{-V_1} & 0 & & \\ -e^{-\delta t K} & e^{-V_2} & 0 & \\ & \ddots & \ddots & \end{pmatrix}^{-1}, \tag{6.50}$$

which is of the form we use in eq. (6.42) with the interaction part residing now on the diagonal. Note that the product of the determinants in eq. (6.41) remains invariant under this transformation, since $\det(G_\sigma) = \det(e^V)\det(\widetilde{G}_\sigma)$ and V changes sign for spin up and down and thus $\det(e^V)\det(e^{-V}) = \mathbb{1}$.

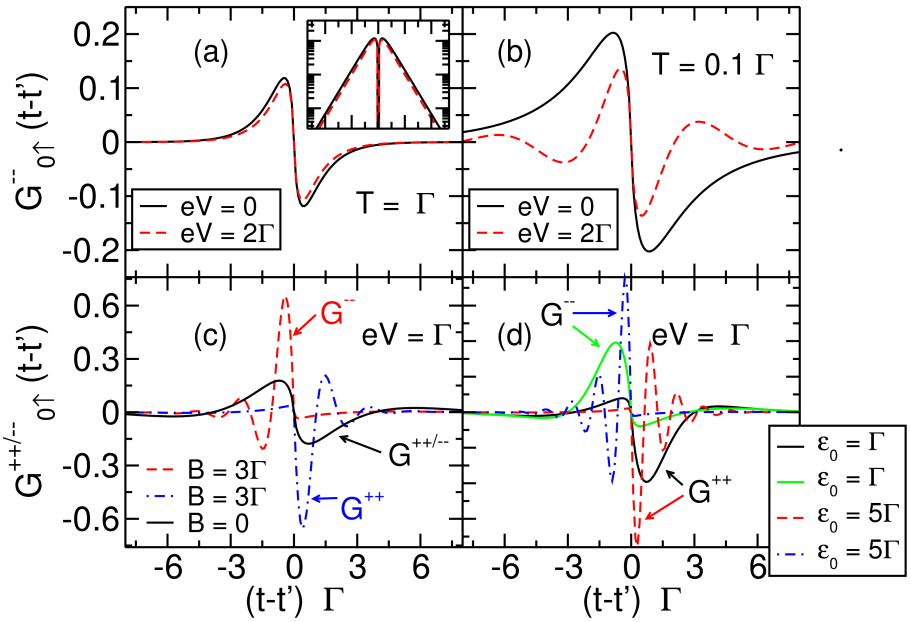

Figure 6.2: Real part of the Keldysh GF component $G^{--}_{0\uparrow}(t-t')$ for (a) $\epsilon_0 = 0, B = 0, T = \Gamma$, (b) $\epsilon_0 = 0, B = 0, T = 0.1\Gamma$, (c) $\epsilon_0 = 0, T = 0.1\Gamma, eV = \Gamma, B = 0$ and $B = 3\Gamma$, (d) $B = 0, T = 0.1\Gamma, eV = \Gamma, \epsilon_0 = \Gamma$ and $\epsilon_0 = 5\Gamma$. The inset in (a) shows the absolute values of the same data in log-linear representation, highlighting the exponential decrease.

6.3 The iterative path-integral scheme

Let us now exploit the property (see, e.g., ref. [11]) that each Keldysh component of $G_{0\sigma,kl}$ decays exponentially at long time differences ($|k-l| \to \infty$) for finite T, see eq. (6.43). We denote the corresponding time scale (correlation or memory time) by τ_c. In fig. 6.2 we show typical examples of $\mathrm{Re}\, G^{--}_{0\uparrow,kl}$ for different bias voltages V. The exponential decrease with time is illustrated in the inset of fig. 6.2(a) where the absolute value $|\mathrm{Re}\, G^{--}_{0\uparrow,kl}|$ is again plotted for the same parameters, but in a log-linear representation. For large bias voltages and low enough temperatures, e.g., at $V \gtrsim \Gamma$ and $T \leq 0.2\Gamma$, the decay is superposed by an oscillatory behavior, see fig. 6.2. Since the lead-induced correlation function decays as $\sim \cos[eV(t-t')/2]/\sinh[\pi T(t-t')]$, the respective correlations decay on a time scale given by $\tau_c^{-1} \sim \max(k_B T, eV)$. (The correlation function also has an additional ϵ_0-dependence of the decay characteristics.) Thus, the exponential decay suggests to neglect lead-induced correlations beyond the correlation time τ_c. This motivates an iterative scheme which exactly takes into account the correlations within τ_c, but neglects them outside. The exponential decay has to be contrasted to the case $T = V = 0$, where correlations die out only algebraically, and our approach is not applicable.

Let us then face the remaining path sum in eq. (6.41). In the discrete time representation, we denote with $t_0 = 0 < t_N = N\delta_t$ the initial and final time, and

$t_k = k\delta_t$, see fig. 6.1. The discretized GF and self-energy kernels for given spin σ are then represented as matrices of dimension $2N \times 2N$. For explicit calculations, we arrange the matrix elements related to Keldysh space (characterized by the Pauli matrices τ) and to physical times (t_k, t_l) as $\tau \otimes (k, l)$. In particular, the ordering of the matrix elements from left to right (and from top to bottom) represent increasing times. The lead-induced correlations thus decrease exponentially with growing distance from the diagonal of the matrix. For numerical convenience, we evaluate the generating function in the equivalent form

$$Z[\eta] = \mathcal{N} \sum_{\{s\}} \prod_{\sigma} \det D_\sigma[\{s\}, \eta], \tag{6.51}$$

with $D_\sigma = G_\sigma^{-1} G_{0\sigma}$. Explicitly, this reads

$$D^{\alpha\beta}_{\sigma,kl}[\{s\}, \eta] = \delta_{\alpha\beta}\delta_{kl} + i\delta_t \lambda_\alpha G^{\alpha\beta}_{0\sigma,kl} s^\alpha_k - i\eta \sum_{j,\alpha'} G^{\alpha\alpha'}_{0\sigma,kj} \Sigma^{J,\alpha'\beta}_{jl} \tag{6.52}$$

The normalization prefactor $\mathcal{N}$ does not affect physical observables, and is put to unity. The time local nature of the on-dot interaction is now present only in disguise, since the matrix product lets Ising spins appear line-wise. By construction, we have to sum over $2N$ auxiliary Ising spins, and the total number of possible spin configurations is 2^{2N}.

Next, we exploit the above-mentioned truncation of the GF by setting $D_{kl} \equiv 0$ for $|k - l|\delta_t > \tau_c$, where

$$\tau_c \equiv K\delta_t \tag{6.53}$$

is the memory time, with K the respective number of Trotter time slices. The GF matrices then have a K-band structure. Note that in the continuum limit, where $K = N, \delta_t \to 0$ and $N \to \infty$, the approach is exact.

To prepare the basis for the iterative scheme, we now transform the GF matrix to Schur's form, which then allows to calculate the determinant in a straightforward way. In general, a quadratic block matrix D given as

$$D = \begin{pmatrix} a & b \\ c & d \end{pmatrix}, \tag{6.54}$$

with a being invertible, can be represented in its Schur form, i.e., after one step of Gaussian elimination. Hence, by multiplying from the left with a lower triangular matrix,

$$\tilde{D} = LD = \begin{pmatrix} I_n & 0 \\ ca^{-1} & I_m \end{pmatrix} \begin{pmatrix} a & b \\ c & d \end{pmatrix} = \begin{pmatrix} a & b \\ 0 & d - ca^{-1}b \end{pmatrix}, \tag{6.55}$$

where $I_{n(m)}$ represent unit matrices of dimension $n = \dim a$ ($m = \dim d$), and b, c do not have to be quadratic themselves. Clearly, the determinant is invariant under this transformation. The $(2, 2)$ element in this block notation is often referred to as the Schur complement of the matrix D. This representation thus allows to write the

determinant as $\det(D) = \det(a)\det(d - ca^{-1}b)$. We can now establish the iterative scheme as follows. We start from the full GF in the matrix representation as defined in eq. (6.52). After the memory truncation, the $N \times N-$matrix (in time space) assumes a band structure represented as

$$D \equiv D_{(1,N_K)} = \begin{pmatrix} D^{11} & D^{12} & 0 & 0 & \dots & 0 \\ D^{21} & D^{22} & D^{23} & 0 & \dots & \vdots \\ 0 & D^{32} & D^{33} & D^{34} & \dots & \vdots \\ 0 & 0 & D^{43} & D^{44} & \dots & 0 \\ \vdots & \vdots & \vdots & \vdots & \ddots & D^{N_K-1N_K} \\ 0 & \dots & \dots & 0 & D^{N_KN_K-1} & D^{N_KN_K} \end{pmatrix} \tag{6.56}$$

where the single blocks are $K \times K-$block matrices defined as $(l, l' = 1, \dots, N_K)$

$$D^{ll'} = \begin{pmatrix} D_{(l-1)K+1,(l'-1)K+1} & \dots & D_{(l-1)K+1,l'K} \\ \vdots & \ddots & \vdots \\ D_{lK,(l'-1)K+1} & \dots & D_{lK,l'K} \end{pmatrix}. \tag{6.57}$$

The number N of Trotter slices is always chosen such that $N_K \equiv N/K$ is integer. The elements D_{kl} are given in eq. (6.52), with their dependence on the Ising spins $s_k^{\pm}$ kept implicit. Each D_{kl} still has a $2 \times 2-$Keldysh structure, and a 2×2 spin structure. Then, we rewrite the generating function (6.51) as

$$\begin{aligned} Z[\eta] = \sum_{s_1^{\pm},\dots,s_N^{\pm}} & \det\left\{D^{11}[s_1^{\pm},\dots,s_K^{\pm}]\right\} \det\left\{D_{(2,N_K)}[s_{K+1}^{\pm},\dots,s_N^{\pm}]\right. \\ & \left. - D^{21}[s_{K+1}^{\pm},\dots,s_{2K}^{\pm}]\left[D^{11}[s_1^{\pm},\dots,s_K^{\pm}]\right]^{-1} D^{12}[s_1^{\pm},\dots,s_K^{\pm}]\right\}, \end{aligned} \tag{6.58}$$

where the $N_K - 1 \times N_K - 1-$matrix $D_{(2,N_K)}$ is obtained from $D_{(1,N_K)}$ by removing the first line and the first column.

In order to set up an iterative scheme, we use the following observation: to be consistent with the truncation of the correlations after a memory time $K\delta_t$, we have to neglect terms that directly couple Ising spins at time differences larger than the memory time. This is achieved by setting

$$D^{l+2,l+1}\left[D^{l+1,l+1}\right]^{-1} D^{l+1,l}\left[D^{l,l}\right]^{-1} D^{l,l+1}\left[D^{l+1,l+1}\right]^{-1} D^{l+1,l+2} \to 0 \tag{6.59}$$

within the Schur complement in each further iteration step. Note that we do not neglect the full Schur complement but only those parts which are generated in the

second-next iteration step. With this, we rewrite the generating function as

$$Z[\eta] = \sum_{s_1^\pm,\ldots,s_N^\pm} \det\left\{D^{11}[s_1^\pm,\ldots,s_K^\pm]\right\} \prod_{l=1}^{N_K-1} \det\Big\{D^{l+1,l+1}[s_{lK+1}^\pm,\ldots,s_{(l+1)K}^\pm] \tag{6.60}$$
$$- D^{l+1,l}[s_{lK+1}^\pm,\ldots,s_{(l+1)K}^\pm]\left[D^{l,l}[s_{(l-1)K+1}^\pm,\ldots,s_{lK}^\pm]\right]^{-1} D^{l,l+1}[s_{(l-1)K+1}^\pm,\ldots,s_{lK}^\pm]\Big\}\,.$$

Then, one can exchange the sum and the product, and by reordering the sum over all Ising spins, one obtains

$$Z[\eta] = \sum_{s_{N-K+1}^\pm,\ldots,s_N^\pm} Z_{N_K}[s_{N-K+1}^\pm,\ldots,s_N^\pm]\,, \tag{6.61}$$

where Z_{N_K} is the last element obtained from the iterative procedure defined by $(l = 1,\ldots,N_K-1)$

$$\begin{aligned} Z_{l+1}[s_{lK+1}^\pm,\ldots,s_{(l+1)K}^\pm] &= \sum_{s_{(l-1)K+1}^\pm,\ldots,s_{lK}^\pm} \Lambda_l[s_{(l-1)K+1}^\pm,\ldots,s_{lK}^\pm, s_{lK+1}^\pm,\ldots,s_{(l+1)K}^\pm] \\ &\times\ Z_l[s_{(l-1)K+1}^\pm,\ldots,s_{lK}^\pm]\,. \end{aligned} \tag{6.62}$$

The *propagating tensor* Λ_l can be read off from eq. (6.60) as

$$\Lambda_l = \det\Big\{D^{l+1,l+1}[s_{lK+1}^\pm,\ldots,s_{(l+1)K}^\pm] \tag{6.63}$$
$$- D^{l+1,l}[s_{lK+1}^\pm,\ldots,s_{(l+1)K}^\pm]\left[D^{l,l}[s_{(l-1)K+1}^\pm,\ldots,s_{lK}^\pm]\right]^{-1} D^{l,l+1}[s_{(l-1)K+1}^\pm,\ldots,s_{lK}^\pm]\Big\}\,.$$

Note that we use here the notion of *tensor* in the sense of a multi-dimensional array and not in the strict mathematical sense defined by the transformation properties of this object, see also ref. [8]. The iteration starts with $Z_1[s_1^\pm,\ldots,s_K^\pm] = \det\left\{D^{11}[s_1^\pm,\ldots,s_K^\pm]\right\}$.

The current is numerically obtained by evaluating eq. (6.31) for a small but fixed value of η; we have taken $\eta = 0.001$ for all results shown below. By this, we obtain the full time-dependent current $I(t_m)$ as a function of the measurement time t_m $(0 \le t_m \le N\delta_t)$. At short times, this shows a transient oscillatory or relaxation behavior, which then reaches a plateau value from which we read off the steady-state current I.

At this point we would like to note that this chapter was also part of the PhD thesis [94]. We have implemented an independent version of the ISPI scheme and have carefully validated that both implementations yield the same results. Besides some syntactical differences our implementation differs mainly in:

1. The matrix elements in the blocks $D^{l,l+1}$ and $D^{l+1,l}$ beyond the characteristic memory time τ_c are set to zero, resulting in real lower/upper triangular matrices, respectively.

2. Within each iteration step, the summation over Ising-spins $s^{\pm}$ is divided into an inner an an outer loop. To be specific for each fixed spin configuration of the spins $s^{\pm}_{lK+1}, \ldots, s_{(l+1)K}$ (within the outer loop) we compute the sum of *all* spin configurations depending on $s^{\pm}_{(l-1)K+1}, \ldots, s^{\pm}_{lK}$ within an inner loop. A the end this yields the propagating tensor Λ_l needed for the next iteration step, stored in an array of dimension 2^{2K}. Within the next iteration step the values of the adequate spin configuration of Λ_l are called within the inner loop of the spin summation.

However, the main ideas on which the ISPI scheme is bulid on, as e.g. the structure and ordering of the iteration blocks D, the summation over $s^{\pm}$ and the computation of the Fourier-transformation of the Green's function are the results of fruitful discussions and collaborations with the author of [94]. The ISPI results shown in the figs. 6.2-6.4, 6.6-6.10 and 6.16 were obtained within our version of the code.

6.4 Convergence and extrapolation procedure

In order to render the scheme exact, we have to eliminate the two systematic errors which are still present up to this point, namely, (i) the Trotter error due to finite time discretization $\delta_t = t/N$, and (ii) the memory error due to a finite memory time $\tau_c = K\delta_t$. The scheme becomes exact by construction in the limit $K \to \infty$ and $\delta_t \to 0$. To perform this limit in a straightforward way is not possible due to the exponential dependence of the array sizes on K. However, unless temperature is very low, we can eliminate both errors from the numerical data in the following systematic way: (i) We choose a fixed time discretization δ_t and a memory time τ_c. A reasonable estimate for τ_c is the minimum of $1/|eV|$ and $1/T$ (see above). With that, we calculate the current $I(\delta_t, \tau_c)$, and, if desired, the differential conductance $dI(\delta_t, \tau_c)/dV$ (the derivative is performed numerically for a small $\Delta V = 0.01\Gamma$). The calculation is then repeated for different choices of δ_t and τ_c.

(ii) Next, the Trotter error can be eliminated by exploiting the fact that it vanishes quadratically for $\delta_t \to 0$ [138, 139, 10]. For a fixed memory time τ_c, we can thus extrapolate and obtain $dI(\tau_c)/dV = dI(\delta_t \to 0, \tau_c)/dV$, which still depends on the finite memory time τ_c. The quadratic dependence on δ_t is illustrated in fig. 6.3 for different values of U. Note that each line corresponds to the same fixed memory time $\tau_c = 0.5/\Gamma$. (iii) In a last step, we eliminate the memory error by extrapolating for $1/\tau_c \to 0$, and obtain the final numerically exact value $dI/dV = dI(\tau_c \to \infty)/dV$. For the dependence on $1/\tau_c$, we empirically find a regular and systematic behavior as shown in fig. 6.4. The $\tau_c \to \infty$ value is approached with corrections of the order of $1/\tau_c$, see fig. 6.4. However, it should be stressed that temperature and voltage affect the convergence properties in different ways, as is already clear from fig. 6.2. Importantly enough, when T and V are such that the extrapolation scheme described above converges, numerical exactness is warranted. We have implemented the iterative scheme together with the convergence procedure on standard Xeon 2GHz machines. Computations are then only possible for $K \leq 7$ due to the limited

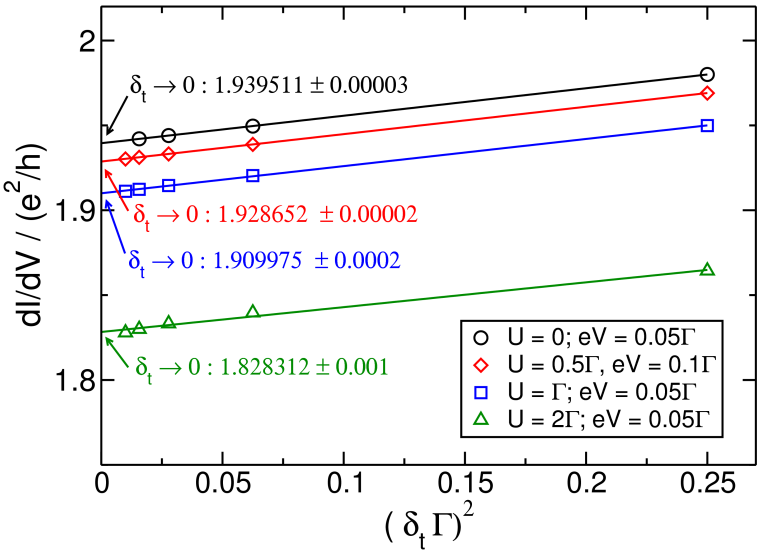

Figure 6.3: Quadratic dependence of the Trotter error as obtained in the convergence procedure for $\delta t \to 0$ for a fixed memory time $\tau_c = 0.5/\Gamma$. Parameters are $\epsilon_0 = 0, B = 0, T = 0.1\Gamma$. The extrapolated values are given in the figure.

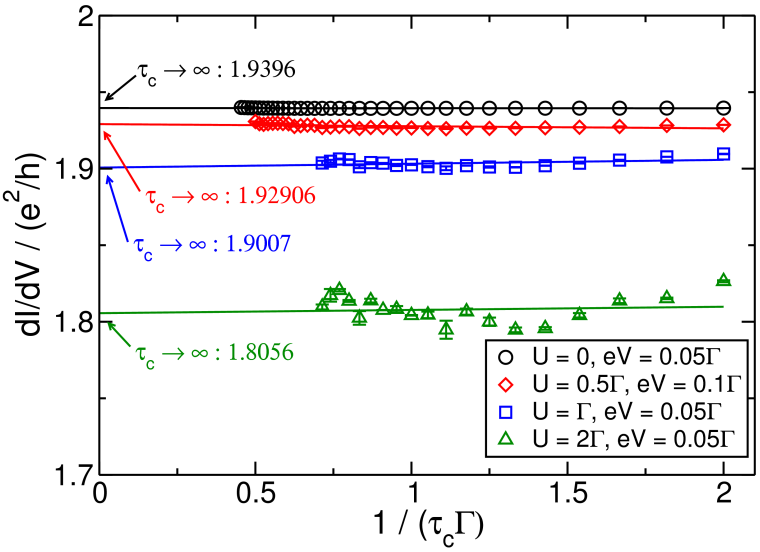

Figure 6.4: Dependence of the differential conductance $dI(\tau_c)/dV$ on the inverse memory time $1/\tau_c$ for different values of U after the Trotter error has been eliminated. Parameters are $\epsilon_0 = B = 0, T = 0.1\Gamma$. Solid lines correspond to a linear fit. The extrapolated values for $dI/dV = dI(1/\tau_c \to 0)/dV$ are given in the figure.

memory (RAM) resources available. Typical running times for the shown simulation data are approximately 15 hours for $K = 5$. With a second, parallelized version of the code, we have been able to take into account up to 2^{14} summands in eq. (6.62), corresponding to $K = 7$, within passable running times of a few days.

The empirically found behavior on $1/\tau_c$ when $\tau_c \to \infty$ is under active discussions. For large U this approach seems to fail and other possibilities to achieve convergence are in demand. From fig. 6.4 one can already notice that for $U = 2\Gamma$ the extrapolation becomes less accurate, but here the accuracy is still sufficient. A way to overcome these problems is for instance the principle of least dependence which has successfully been used within the QUAPI method, see chapter 3 and further work will be assigned to that topic. Moreover there are promising concepts to optimize the implementations of the ISPI scheme such that $K = 10$ seems to be achievable within passable runtimes.

6.5 Results

Next, we discuss the results obtained by the application of the iterative procedure to the Anderson model. As pointed out before, see sec. 6.2.1, we consider the symmetric case, $\Gamma_R = \Gamma_L = \Gamma/2$, with $\mu_{L/R} = \pm eV/2$. In what follows, we measure energies in units of Γ. Unless noted otherwise, all error bars for the shown data points, which are due to the Trotter and memory extrapolation scheme, are of the order of the symbol sizes in the figures. Our scheme yields the full time-dependent current $I(t)$, including transients as well as the asymptotic steady-state value. Fig. 6.5 shows typical results for the current $I(t)$, for two parameter sets, namely (1) $U = 4\Gamma, eV = 2\Gamma, T = 0.1\Gamma$ (black circles), and (2) $U = 0.5\Gamma, eV = 0.6\Gamma, T = \Gamma$ (red squares). The first set is of interest in the context of the nonequilibrium Kondo effect, where the Kondo temperature (for $\epsilon_0 = 0$) is $T_K = \sqrt{\Gamma U/2}\exp(-\pi U/8\Gamma)$; for parameter set (1), this yields $T_K = 0.29\Gamma$. For $eV \gg T_K$, analytical results for the steady-state current are available [45, 142], shown as solid line in fig. 6.5. This indicates that the ISPI method is capable of approaching the nonequilibrium Kondo problem. For both parameter sets, and for many others not shown here, we observe that after a transient relaxation behavior, $I(t)$ settles at a plateau value, which then defines the stationary current discussed in the following.

6.5.1 Validation of the algorithm: comparison with exact and perturbative results

As a simple warm-up check, let us briefly compare our numerical results to the exact result for $U = 0$. Fig. 6.6(a) shows the stationary current (obtained already at $t_m = 10/\Gamma$) as a function of ϵ_0 for $T = 10\Gamma$ and $eV = 0.1\Gamma$. The I-V characteristics is shown in fig. 6.6(b) for $T = 10\Gamma$ and $\epsilon_0 = 0$. Both cases illustrate that the numerical result coincides with the exact one. Other parameter sets have been checked as well, and agree with the well-known $U = 0$ analytical solution.

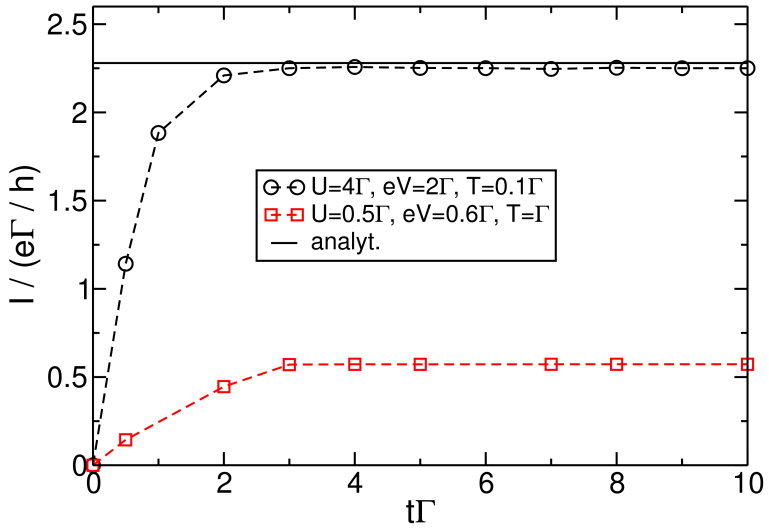

Figure 6.5: Time-dependent current $I(t)$ for two representative parameter sets: (1) $U = 4\Gamma, eV = 2\Gamma, T = 0.1\Gamma$ (black circles) and (2) $U = 0.5\Gamma, eV = 0.6\Gamma, T = \Gamma$ (red squares). Solid line: analytical result for stationary I from nonequilibrium Kondo theory applied to parameter set (1) [45, 142]. Symbols are ISPI results, dashed lines are guides to the eye only, and $\epsilon_0 = B = 0$.

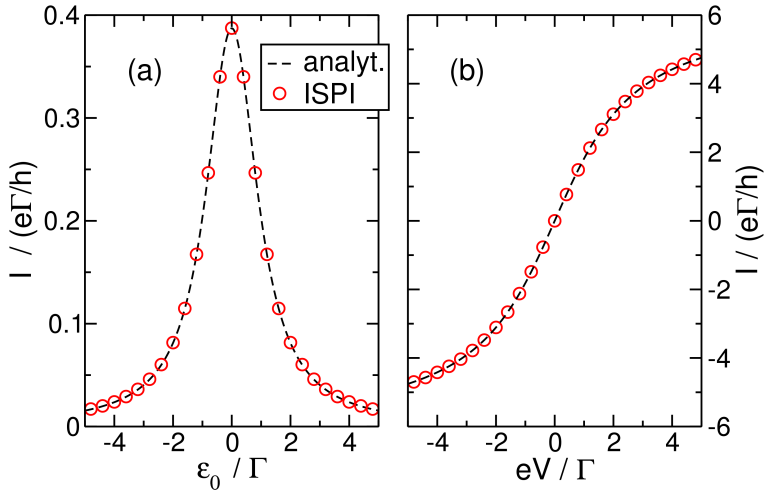

Figure 6.6: Stationary current as a function of ϵ_0 (a) and of the bias voltage eV (b) for the noninteracting case $U = 0$. Shown are the numerical (circles) and the exact analytical (dashed curve) results for (a) $T = 10\Gamma, eV = 0.1\Gamma$, and (b) $\epsilon_0 = 0, T = 10\Gamma$. In both cases, $B = 0$.

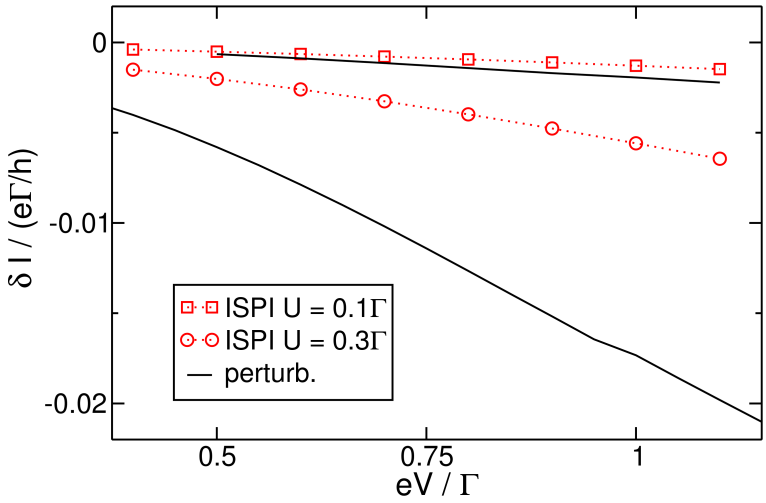

Figure 6.7: Interaction corrections $\delta I(V) = I(U) - I(U = 0)$ from the numerical ISPI approach (red symbols) and from a second-order perturbative calculation (black solid lines), for $U = 0.1\Gamma$ (squares) and $U = 0.3\Gamma$ (circles). Parameters are $\epsilon_0 = B = 0, T = 0.1\Gamma$, and dotted lines are guides to the eye only.

Second, in order to validate the reliability of our code for finite U, we compare the numerical results to a perturbative calculation, where the interaction self-energy is computed up to second order in U [143]. In order to respect current conservation, this calculation is possible only at the electron-hole symmetric point, $\epsilon_0 = B = 0$ [51]. First-order terms give then no contribution, and the self-energy corresponds to just one diagram [143]. For a detailed comparison, we plot mostly the *interaction corrections*, $\delta A \equiv A(U) - A(U = 0)$, with A being the current I, the linear conductance G, or the nonlinear conductance dI/dV, respectively. Fig. 6.7 shows the results for δI as a function of the bias voltage for $U = 0.1\Gamma$ and $U = 0.3\Gamma$. For $U = 0.1\Gamma$, we perfectly recover the perturbative results, which confirms the reliability of our code even in the regime of nonlinear transport. Clearly, the corrections are small and negative, which can be rationalized in terms of Coulomb blockade physics, as transport is suppressed by a finite interaction on the dot.

For $U = 0.3\Gamma$, the current decreases even more, and the deviations between the ISPI and perturbative results are also larger. The relative deviation for $U = 0.3\Gamma$ is already $\approx 30 - 35\%$, illustrating that perturbation theory is already of limited accuracy in this regime. Although it well reproduces the overall tendency, there is significant quantitative disagreement. The differences are even more pronounced for $U = \Gamma$, as shown in fig. 6.8 for δI (main) and for $\delta(dI/dV)$ (inset). Here, second-order perturbation theory does not even reproduce qualitative features.

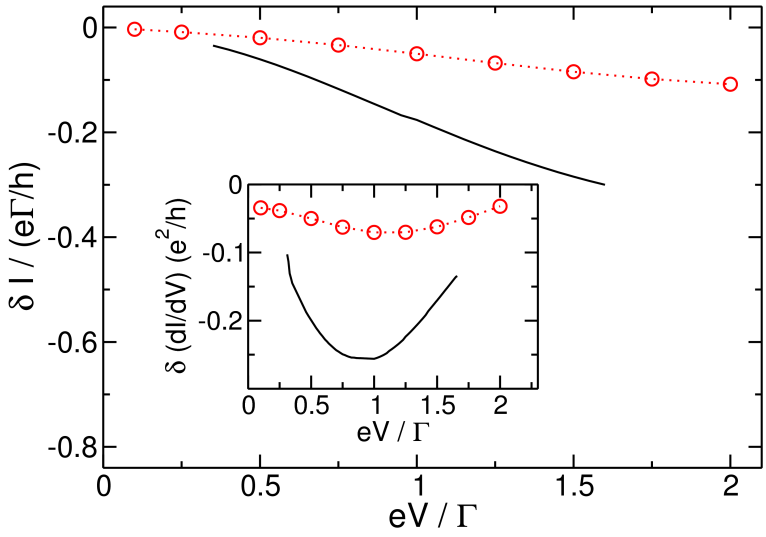

Figure 6.8: Interaction correction δI for the nonlinear current for $U = \Gamma$, comparing ISPI (red symbols) and U^2 perturbation theory (black solid curve). The inset shows the corresponding interaction corrections $\delta(dI/dV)$ to the differential conductance. Other parameters are as in fig. 6.7. Dashed lines are guides to the eye only.

6.5.2 Comparison with master equation approach

Next, we compare our numerical approach with the outcome of a standard master equation calculation [77]. The master equation is expected to yield reliable results in the incoherent (sequential) tunneling regime, $T \gg \Gamma$, where a description in terms of occupation probabilities for the isolated many-body dot states is appropriate. The transport dynamics is then described by a rate equation for the populations, where the time-dependent rates are obtained from lowest-order perturbation theory in Γ [77]. The results are shown for $U = \Gamma$ in fig. 6.9, both for the nonlinear and the linear differential conductance interaction corrections. As temperature is lowered, interaction effects become more important, as seen from the exact ISPI results. This corresponds to the emergence of coherence effects for $T < \Gamma$, which are clearly not captured by the master equation in the sequential tunneling approximation. However, for $T \gtrsim 4\Gamma$, interaction corrections are washed out, and the master equation becomes essentially exact, cf. fig. 6.9. Similarly, from our ISPI results, we observe that interaction corrections are suppressed by an increasing bias voltage as well. To give numbers, for $T = 1.25\Gamma$, we find in the linear regime $\delta G = -0.073e^2/h$, whereas $\delta(dI/dV) = -0.062e^2/h$ for $eV = 3\Gamma$.

6.5.3 Small bias: $eV \ll \Gamma$

For sufficiently small bias voltage, the current is linear in V, and we can focus on the linear conductance and its interaction correction δG. Fig. 6.10 shows δG as

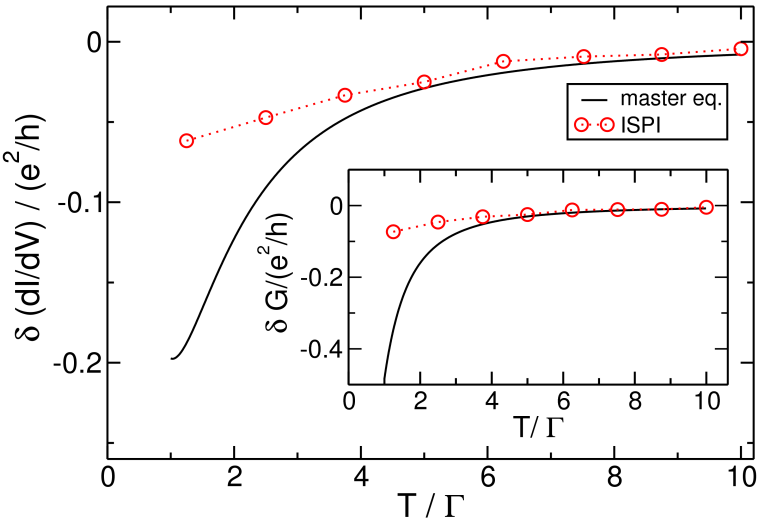

Figure 6.9: Comparison of the ISPI method (red symbols) and the master equation approach (solid lines) for $U = \Gamma$. Main: Corrections $\delta(dI/dV)$ of the nonlinear conductance as a function of temperature for $eV = 3\Gamma$. Inset: Same for the linear conductance δG. For the remaining parameters, see fig. 6.7.

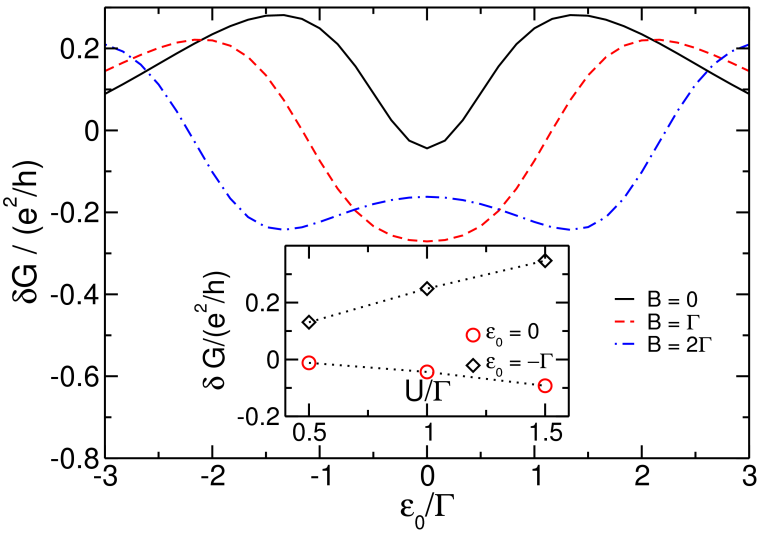

Figure 6.10: Interaction correction δG as a function of ϵ_0, for $U = \Gamma$, different B, and $T = 0.1\Gamma$. Inset: Dependence of δG on U for $B = 0$, on resonance ($\epsilon_0 = 0$, red circles) and away from resonance ($\epsilon_0 = -\Gamma$, black diamonds).

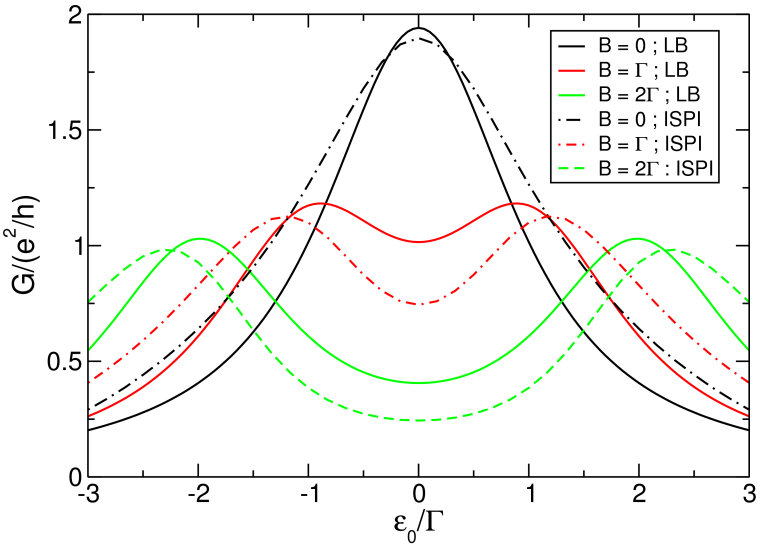

Figure 6.11: Linear conductance G as a function of ϵ_0, corresponding to Fig. 6.10 together with the exact $U = 0$ results (LB).

a function of ϵ_0 for different magnetic fields B, taking $U = \Gamma$ and $T = 0.1$ (to be specific, we have chosen $eV = 0.05\Gamma$). For $B = 0$, two spin-degenerate transport channels contribute, and a single resonant-tunneling peak at $\epsilon_0 = 0$ results which is lowered by U. Moreover, peaks at $\pm U/2$ evolve, where U lifts the spin degeneracy leading to positive interaction corrections δG. These peaks are superimposed by the central peak at $\epsilon_0 = 0$ since the level splitting is not large enough at $U = \Gamma$. For $B \neq 0$, the spin-dependent channels are split by $\Delta\epsilon = 2B + u$. The spin-resolved levels are now positioned at $\pm(B + U/2)$ due to the Zeeman splitting and the splitting according to U, as can be seen from fig. 6.11. Note that the peaks are slightly shifted away from $\pm(B + U/2)$ due the superposition with the small but finite central peak. We have also calculated this behavior within the Master equation approach, see fig. 6.12, yielding the correct peak positions. For $B = 0$ we find evidence for an interaction-induced broadening of the resonant-tunneling peak compared to the noninteracting case. The width of the Lorentzian peak profile for $B = 0$ is determined by Γ at sufficiently low T, and broadens as T increases.

In order to illustrate the role of the interaction U, we show the dependence of δG on U at $\epsilon_0 = 0$ in the inset of fig. 6.10. For $U = 0$, both levels contribute e^2/h to the conductance at low temperatures, while for finite U these contributions are reduced since the resonant peak is lowered by U. The reduction increases with growing U, qualitatively consistent with previous results. Away from resonance, $\epsilon = -\Gamma$, see inset of fig. 6.10, we find positive interaction corrections steming from the broadening of the central peak due to the development of peaks at $\pm U/2$. Clearly, these interaction corrections grow with increasing U. Note that the interaction corrections are more pronounced away from resonance.

Next, we address the temperature dependence of the linear conductance (numer-

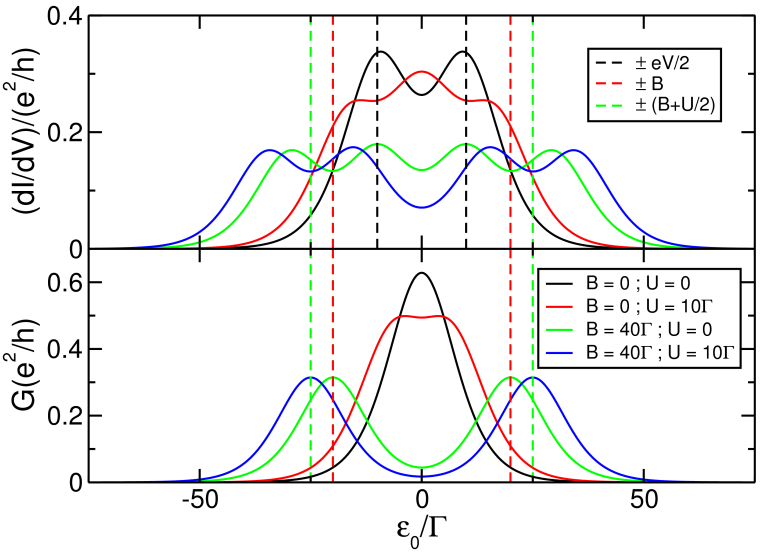

Figure 6.12: Differential and linear conductance as a function of gate voltage obtained from a master equation approach. The temperature is $T = 5\Gamma$ and $eV = 20\Gamma$ for the differential conductance.

ically evaluated for $eV = 0.05\Gamma$). In fig. 6.13, we show $G(T)$ for different values of U (up to $U = 4\Gamma$) at $\epsilon = B = 0$. For $U = 1.2\Gamma$, the deviation from the $U = 0$-result is small in the considered temperature range. For larger U, deviations become more pronounced at low temperatures where interaction becomes increasingly relevant. Up to present, we have obtained converged results in the regime of *small* bias voltages for interaction strengths $U \leq 4\Gamma$ for temperatures above or close to the Kondo temperature, $T \gtrsim T_K$. The corresponding Kondo temperatures are (see above) $T_K = 0.38\Gamma$ for $U = 3\Gamma$ and $T_K = 0.293\Gamma$ for $U = 4\Gamma$. In the regime $T_K \lesssim T \lesssim 10T_K$, we can compare our results to the result of Hamann [144, 145],

$$G(T) = \frac{e^2}{h}\left(1 - \frac{\ln(T/T_{KH})}{[\ln^2(T/T_{KH}) + 3\pi^2/4]^{1/2}}\right), \tag{6.64}$$

for the linear conductance, where $T_{KH} = T_K/1.2$, see fig. 6.13 (solid lines).

In ref. [144], it has been shown that the results of the numerical RG coincide with those of eq. (6.64) in this regime. Fig. 6.13 illustrates that the agreement between the two approaches is satisfactory and shows that the ISPI provides reliable results in the linear regime above or close to the Kondo temperature. As already mentioned, convergence is problematic in the *linear* regime for temperatures lower than the Kondo temperature for larger values of U. This implies that the equilibrium Kondo regime is difficult to explore using the ISPI approach. However, the situation is more favorable for large bias voltages, where short to intermediate memory times are sufficient, and we have achieved convergence up to $U = 4\Gamma$, see fig. 6.5 and the next subsection.

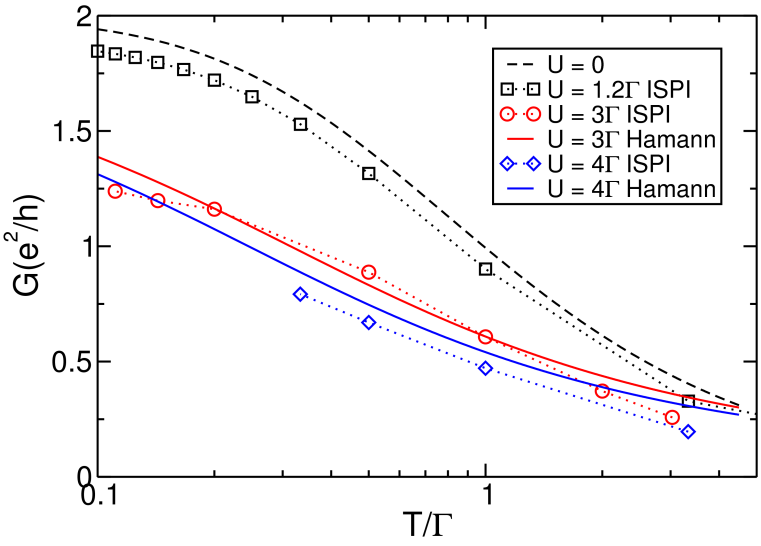

Figure 6.13: Linear conductance G vs temperature T, for $U = 0$ (dashed line) and $U = 1.2, 3, 4\Gamma$ ($\epsilon_0 = B = 0$). Symbols denote the ISPI results while the solid lines are those of eq. (6.64).

6.5.4 Large bias: $eV \geq \Gamma$

Let us then turn to nonequilibrium transport at voltages $eV \gtrsim \Gamma$. Here, the transport window is $\sim eV$, and a double-peak structure for dI/dV emerges even for $B = 0$, with distance eV between the peaks for the non-interacting case, see fig. 6.14. A finite magnetic field splits the main peak to positions $\pm B$ where the voltage induced splitting with distance eV remains for each peak, see fig. 6.15. The effect of turning on the on dot interaction U can be seen from the master equation approach in fig. 6.12. The peaks are lowered and shifted to positions $\pm(B + U/2)$. Moreover there is still the voltage induced splitting with distance eV leading to an overall four-peak structure. For a finite magnetic field this effect is not fully developed for the choice of parameters within our simulations since the peaks are superimposed, see fig. 6.14. For e.g. $B = \Gamma$ and the shown values of U, the two innermost peaks (closest to $\epsilon_0 = 0$) overlap so strongly that they effectively form a single peak at $\epsilon_0 = 0$ again.

As interaction corrections to the nonlinear conductance are largest when a dot level is in resonance with one of the chemical potentials of the leads, the double-peak structure is again transferred to $\delta(dI/dV)$. This can be observed in fig. 6.16, for the case $B = 0$, where we show results for $eV = 3\Gamma$ but otherwise the same parameters as in fig. 6.10. Since the applied magnetic field is too small to obtain well separated Zeeman-peaks this effect is washed out for a finite B, due to the superposition of the four-peak structure.

Increasing the on-dot interaction U leads to a reduction of the differential conductance peaks compared to the noninteracting case, i.e., the interaction corrections

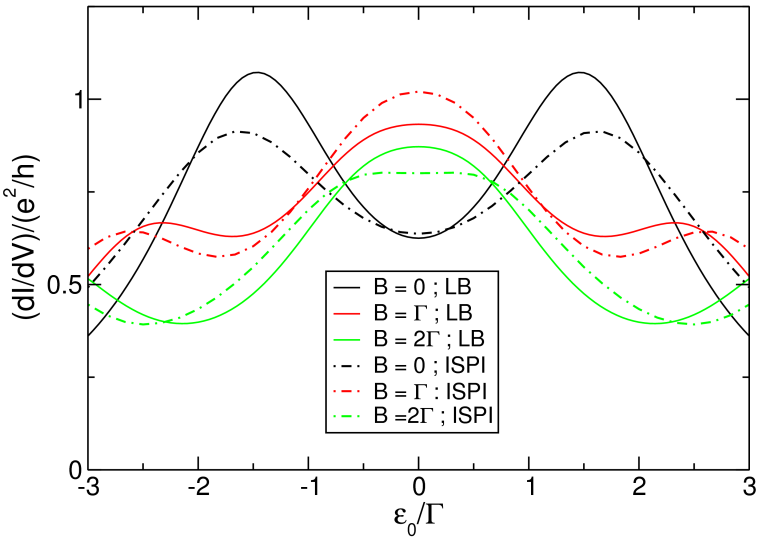

Figure 6.14: Same as fig. 6.11 but for the nonlinear conductance, taken at $eV = 3\Gamma$.

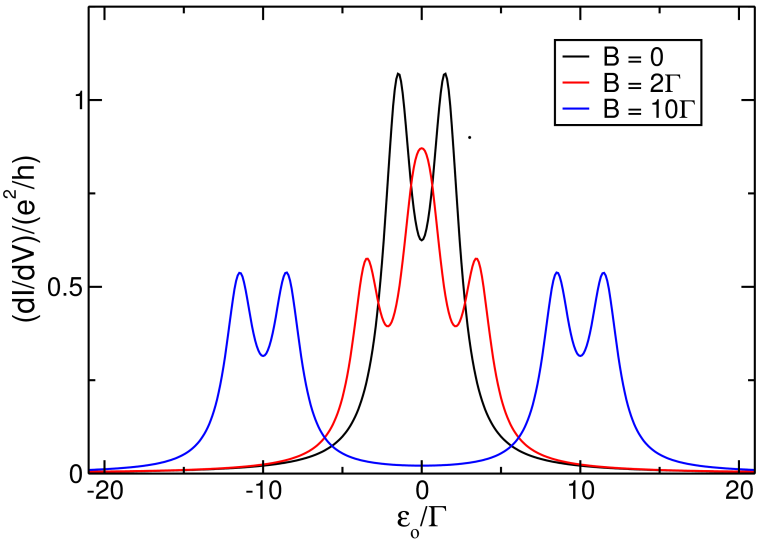

Figure 6.15: Nonlinear conductance for the non-interacting case taken at $eV = 3\Gamma$.

are again largest when the level energy matches the chemical potential in the leads. This is observed in the inset of fig. 6.16, for $B = 0$ and $\epsilon_0 = -\Gamma$, which is close to the peak maximum. Away from resonance, the interaction corrections are reduced.

In the regime $eV \gg T_K$, we can compare our results to the perturbative RG result [45, 142]

$$I(V) = \frac{3\pi^2 e^2 V}{8h} \ln^{-2}(eV/\tilde{T}_K)\,,$$

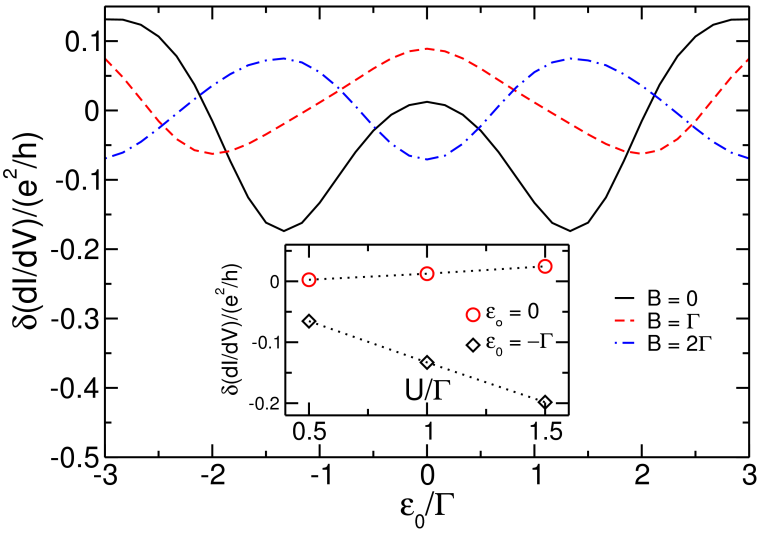

Figure 6.16: Same as fig. 6.10 but for the nonlinear conductance, taken at $eV = 3\Gamma$.

with $\tilde{T}_K = 2T_K/\sqrt{\pi}$. Fig. 6.5 shows the result for the stationary current for $U = 4\Gamma$ (where $T_K = 0.29\Gamma$) for $eV = 2\Gamma$. The perturbative current amounts to $I_\infty = 2.28e\Gamma/h$, while the ISPI value is $I_{ISPI} = 2.25e\Gamma/h$. The quite satisfactory agreement suggests that ISPI is indeed a reliable new method that holds promise for reaching the nonequilibrium Kondo regime. A detailed study of the nonequilibrium Kondo effect using ISPI will be given elsewhere.

Finally, we address the temperature dependence of the nonlinear conductance dI/dV. ISPI results for $eV = 2\Gamma, \epsilon_0 = B = 0$ are shown in fig. 6.17. Again, as in the linear regime, the conductance increases with lower temperatures, and finally saturates, e.g., at $dI/dV = e^2/h$ for $U = 0$ and $eV = 2\Gamma$. Clearly the conductance decreases when the bias voltage is raised. Increasing U renders this suppression yet more pronounced, see also inset of fig. 6.17 for the corresponding corrections. At high temperatures, thermal fluctuations wash out the interaction effects, and the interaction corrections die out.

6.6 Discussion and conclusions

In summary, we have introduced a scheme for the iterative summation of real-time path integrals (ISPI), and applied it to a prototypical problem of quantum transport through an interacting quantum dot coupled to metallic leads held at different chemical potentials. After integrating out the leads, a time-nonlocal Keldysh self-energy arises. Exploiting the exponential decay of the time correlations at finite temperature allows to introduce a memory time τ_c beyond which the correlations can be truncated. Within τ_c, correlations are fully taken into account in the corre-

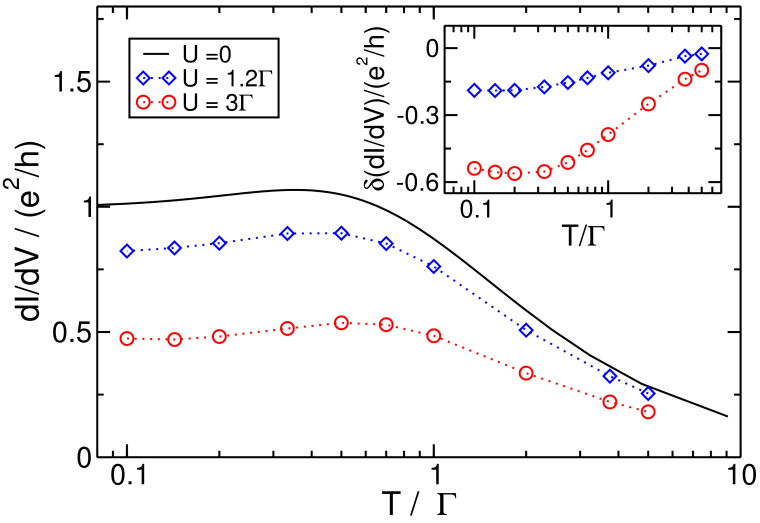

Figure 6.17: Nonlinear differential conductance dI/dV vs temperature T, for $eV = 2\Gamma, \epsilon_0 = B = 0$, and $U = 0, 1.2, 3\Gamma$. Inset: corresponding interaction corrections $\delta(dI/dV)$. (The Kondo temperature for $U = 3\Gamma$ is $T_K = 0.38\Gamma$.)

sponding path integral for the current generating function. Then, through a discrete Hubbard-Stratonovich transformation, interactions can be transferred to an auxiliary quasi-spin field, and an iterative summation scheme has been constructed to calculate the transport current. The remaining systematic errors due to the finite time discretization and the finite memory time τ_c are then eliminated by a refined Hirsch-Fye-type extrapolation scheme, rendering the ISPI numerically exact. From this construction, it is clear that the calculation is reliable for temperatures above a certain interaction-dependent temperature scale. The latter depends also on the computational power available, and vanishes in the absence of interactions.

The general scheme has been applied to the canonical example of an Anderson dot with interaction U, for which many features of the transport characteristics are well understood. This allows to carefully and systematically check the algorithm. In the regime of linear transport, we have recovered results from second-order perturbation theory in U in the limit of very small interaction strength, but found significant deviations already for small-to-intermediate values of U. In the incoherent sequential regime, we recover results from a master equation approach. Taking $U/\Gamma = 4$, we have furthermore reproduced the behavior of the linear conductance above the Kondo temperature and found satisfactory agreement with numerical RG results. In addition, we have investigated the regime of correlated nonlinear transport, where, in our opinion, the presented method is most valuable. We have checked that for large voltage, known results on the nonequilibrium Kondo effect are reproduced as well.

Up to now, we have achieved converged results for small-to-intermediate U even at rather low temperatures and small bias voltages. However, the strong-coupling

regime of the Kondo effect has not yet been fully captured, as the required memory times become quite large, and, at the same time, small δ_t are necessary because of the large U. This combined requirement makes it difficult to reach convergence. Nevertheless, the *nonequilibrium* Kondo regime, representing an intermediate-to-weak coupling situation, seems tractable by the ISPI scheme. The applicability and accuracy of ISPI has been demonstrated for bias voltages larger than the Kondo temperature. We will present a detailed study of this interesting regime elsewhere.

Our approach is, in fact, similar in spirit to the well-established concept of the QUAPI scheme, introduced in detail in chapter 3 and originally introduced by Makri and Makarov [8] in its iterative version. This method has been developed to describe the dynamics of a quantum system coupled to a bath of harmonic oscillators held at equilibrium, in order to obtain exact results for quantum decoherence and dissipation, see also ref. [9] and the previous chapters 3-5, where we have made use of the QUAPI method. For a dipole-type system-bath coupling, as it occurs, e.g., in the spin-boson model [11], the bath-induced correlations are encoded in the Feynman-Vernon influence functional [86], which is solely a functional of a single *system* operator, say $\hat{x}$, which couples the system to the bath, see chapter 2 for a detailed introduction. The very existence of this functional allows to perform a basis rotation to the eigenbasis of $\hat{x}$ (called the discrete variable representation, DVR). Then, the influence functional can be evaluated at the eigenvalues of $\hat{x}$ during the numerical calculation of the real-time path integral over $\hat{x}(t)$. Moreover, within the QUAPI scheme, the influence functional also generates correlations which are non-local in time, but which also decay exponentially. This allows to truncate them beyond a memory-time τ_{mem}, which coincides conceptually with our correlation time τ_c. Then, in practice, numerical convergence has to be achieved with respect to the memory time and afterwards, the only remaining Trotter error can be completely eliminated by extrapolation, see chapter 3 . In the present case of nonequilibrium transport, several fundamental differences occur, and, in fact, only the strategy of memory truncation can be taken over. The major difference is that there exists no simple Feynman-Vernon influence functional. While the lead fermions can be integrated out, see eq. (6.34), the corresponding Grassmann variables for the dot cannot be transferred to a practical computational scheme along the lines of the QUAPI method. Instead, here we integrate out *all* fermions, at the expense of introducing auxiliary Ising spins via the HS transformation. Then, ISPI performs a summation over these Ising spins. Another difference is the form of the tunnel coupling in the Hamiltonian. As two non-commuting system operators d_σ and $d_\sigma^\dagger$ occur, no analogue of DVR can be established here.

Finally, we note that we have chosen the Anderson model as a simple but non-trivial toy model for quantum transport in order to establish and test the numerical algorithm. We believe that this approach, or modifications thereof, will be of importance in numerical calculations of quantum transport properties. Compared to other approaches, it has several advantages (e.g., numerical exactness, direct nonequilibrium formulation, no sign problem), but is, on the other hand, also computationally more costly than most other techniques, especially for strong correlations and/or low

energy scales (temperature, voltage). In any case, it goes without saying that other interesting models for quantum transport exist, and future work will be devoted to apply ISPI to those.

Chapter 7

Summary

To summarize, in the present thesis we have presented studies concerning non-Markovian, time non-local correlations in open quantum systems.

In chapter 3 we have investigated the real-time dynamics of a donor based charge qubit. Here, the charge qubit is coupled to a bosonic environment of phonons which tailors a superohmic spectral density. The numerically exact QUAPI method, which we have improved at one important step, allows for including all non-Markovian effects. By comparison with a Born-Markov approximation it was possible to show that non-Markovian effects lead to small but quantitative important correction for observables of interest, as for instance the quality factor. Our results indicate that phonons are not the main source for dissipation and decoherence within the donor based charge qubit, but represent an upper limit for decoherence which is hard to overcome.

Chapter 4 dealt with an externally driven two-level system coupled to an Ohmic environment. Since this is a realistic model for light-harvesting biomolecules we have concentrated on the influence of the cut-off frequency of the environment. For the biomolecular structures we were interested in, this frequency is of the order of characteristic system energies which renders the dissipative dynamics highly non-Markovian and again the QUAPI method was the ideal method of our choice. Our results have provided evidence for the fact that a driving field which is slow compared to relevant system energies in combination with a non-Markovian environment plays a constructive role in preserving forced oscillations of the population difference of the TLS in the long-time limit. In addition we have identified a resonant behavior of the amplitude of the forced oscillations in the long-time limit, when the characteristic time scale of the TLS and the Ohmic environment coincide. Due to this coincidence the resonant behavior is clearly a highly non-Markovian effect. Moreover we have investigated the regime of coherent destruction of tunneling in the coherent and incoherent regime and identified rich and new features for the decay of the population difference of the TLS in dependence of the characteristic time-scale of the environment.

In chapter 5 we have extended the model used in chapter 4 in the sense that we have investigated the dynamics of two Förster coupled TLS coupled to a common Ohmic environment. Since these two coupled TLS form a bipartite system we have

investigated the dissipative entanglement dynamics of such a system, closely related to biomolecular systems. Indeed, it has been shown within our investigations that an initially entangled state of the two coupled TLS is more robust when subjected to a slow environment. Moreover it turned out that a non-Markovian environment is most successfully and even plays a constructive role in generating entanglement in such biomolecular structures. This hold up to temperatures well beyond the excitonic gap.

Within chapter 6 we have analyzed the non-equilibrium transport properties of an Anderson quantum dot attached to metallic leads. Here, we have developed a novel numerical scheme in order to compute the underlying real-time fermionic path integral in an ab-initio deterministic way. By means of the Keldysh generating functional we are able to compute observables of interest. In the same spirit as the QUAPI method the ISPI scheme is rooted upon the fact that the time non-local correlation functions decay exponentially in time for a finite temperature and can be truncated after a certain memory time. Thus we are again able to account for non-Markovian features. The ISPI scheme has been constructed such that it is numerically exact, since we eliminate the two errors made within the scheme systematically. To be specific we Trotter-extrapolate to a vanishing time increment and are able to extrapolate to an infinite memory time. To check the validity of our novel scheme we have compared our results with known results in different parameter regimes. For the sequential tunneling regime as well as for small on-dot interaction we find good agreement with the outcome of approximate approaches being reliable for the parameters we have chosen. For the nonequilibrium case we reproduce the correct positions of the resonances within the magnetoconductance and find agreement with perturbative results for small on-dot interaction. Since the ISPI scheme is numerically costly it remains a challenge to optimize the scheme to make it accessible for different physical systems, like e.g. the non-equilibrium Kondo regime with a sizeable on-dot interaction or a quantum dot attached to metallic leads which is in addition coupled to a phonon. Future work will address these topics.

To conclude, the results of this thesis as a whole show that time non-local, i.e., non-Markovian correlations are most relevant for the real-time dynamics of open quantum systems. By means of the well established QUAPI scheme we have pointed out this relevance for biomolecular systems and have found features as, e.g., the protection of quantum coherent dynamics over a finite time interval in chapter 4 and the entanglement generation of two biomolecular TLS coupled to a common environment in chapter 5. Both phenomena are rooted upon the very non-Markovian nature of the environment and in that sense an environment where time non-local correlations are present and not negligible may play a constructive role in protecting or even generating pure quantum phenomena. In the same spirit one can understand the results we have obtained within the newly developed ISPI scheme in chapter 6. Although we have been concerned with a fermionic environment here, as in the bosonic case non-Markovian features are most evident for the real-time transport properties of the Anderson dot, as we could show by comparison with approximate methods.

Bibliography

[1] For a review, see the Focus Issue on Solid State Quantum Information, ed. R. Fazio, New J. Phys. **7** (2005).

[2] B. E. Kane, *A silicon-based nuclear spin quantum computer*, Nature **393**, 133 (1998).

[3] S. D. Barrett and G. J. Milburn, *Measuring the decoherence rate in a semiconductor charge qubit*, Phys. Rev. B **68**, 155307 (2003).

[4] L. C. L. Hollenberg, A. S. Dzurak, C. Wellard, A. R. Hamilton, D. J. Reilly, G. J. Milburn and R. G. Clark, *Charge-based quantum computing using single donors in semiconductors*, Phys. Rev. B **69**, 113301 (2004).

[5] D. R. McCamey, H. Huebl, M. S. Brandt, W. D. Hutchison, J. C. McCallum, R. G. Clark and A. R. Hamilton, *Electrically-detected magnetic resonance in ion-implanted Si:P nanostructures*, App. Phys. Lett. **89**, 182115 (2006).

[6] M. Thorwart and P. Hänggi, *Decoherence and dissipation during a quantum XOR gate operation*, Phys. Rev. A **65**, 012309 (2002).

[7] B. Koiller, X. Hu and S. Das Sarma, *Electric-field driven donor-based charge qubits in semiconductors* Phys. Rev. B **73**, 045319 (2006); X. Hu, B. Koiller and S. Das Sarma, *Charge qubits in semiconductor quantum computer architecture: Tunnel coupling and decoherence*, Phys. Rev. B **71**, 235332 (2005).

[8] D.E. Makarov and N. Makri, *Path integrals for dissipative systems by tensor multiplication. Condensed phase quantum dynamics for arbitrarily long time*, Chem. Phys. Lett. **221**, 482 (1994); N. Makri and D.E. Makarov, *Tensor propagator for iterative quantum time evolution of reduced density matrices. I. Theory*, J. Chem. Phys. **102**, 4600 (1995); N. Makri and D.E. Makarov, *Tensor propagator for iterative quantum time evolution of reduced density matrices. II. Numerical methodology* , J. Chem. Phys. **102**, 4611 (1995); N. Makri, *Numerical path integral techniques for long time dynamics of quantum dissipative systems*, J. Math. Phys. **36**, 2430 (1995).

[9] M. Thorwart and P. Jung, *Dynamical Hysteresis in Bistable Quantum Systems*, Phys. Rev. Lett. **78**, 2503 (1997); M. Thorwart, P. Reimann, P. Jung

and R.F. Fox, *Quantum hysteresis and resonant tunneling in bistable systems* Chem. Phys. **235**, 61 (1998); M. Thorwart, P. Reimann, P. Jung and R.F. Fox, *Quantum steps in hysteresis loops*, Phys. Lett. A **239**, 233 (1998); M. Thorwart, P. Reimann and P. Hänggi, *Iterative algorithm versus analytic solutions of the parametrically driven dissipative quantum harmonic oscillator* Phys. Rev. E **62**, 5808 (2000); M. Thorwart, E. Paladino and M. Grifoni, *Dynamics of the spin-boson model with a structured environment*, Chem. Phys. **296**, 333 (2004); M.C. Goorden, M. Thorwart and M. Grifoni, *Entanglement Spectroscopy of a Driven Solid-State Qubit and Its Detector*, Phys. Rev. Lett. **93**, 267005 (2004).

[10] R.M. Fye, *New results on Trotter-like approximations*, Phys. Rev. B **33**, 6271 (1986).

[11] U. Weiss, *Quantum Dissipative Systems*, (3rd ed., World Scientific, Singapore, 2008).

[12] M. Grifoni and P. Hänggi., *Driven quantum tunneling*, Phys. Rep. **304**, 229 (1998).

[13] S. Chu, *Nobel Lecture: The manipulation of neutral particles*, Rev. Mod. Phys. **70**, 685 (1998); C. N. Cohen-Tanoudji, *Nobel Lecture: Manipulating atoms with photons*, *ibid.* 707; W. D. Phillips, *Nobel Lecture: Laser cooling and trapping of neutral atoms*, *ibid.* 721.

[14] M. W. Noel, W. M. Griffith and T. F. Gallagher, *Frequency-modulated excitation of a two-level atom*, Phys. Rev. A **58**, 2265 (1998).

[15] F. Grossmann, T. Dittrich, P. Jung and P. Hänggi, *Coherent destruction of tunneling*, Phys. Rev. Lett. **67**, 516 (1991).

[16] I. Chiorescu, P. Bertet, Y. Nakamura, C. P. M. Harmans and J. E. Mooij, *Coherent dynamics of a flux qubit coupled to a harmonic oscillator*, Nature **431**, 159 (2004).

[17] M. Thorwart, J. Eckel and E. R. Mucciolo, *Non-Markovian dynamics of double quantum dot charge qubits due to acoustic phonons*, Phys. Rev. B **72**, 235320 (2005).

[18] V. May and O. Kühn, *Charge and energy transfer dynamics in molecular systems* (Wiley, Berlin, 2001).

[19] T. Brixner, J. Stenger, H.M. Vaswani, M. Cho, R.E. Blankenship and G.R. Fleming, *Two-dimensional spectroscopy of electronic couplings in photosynthesis*, Nature **434**, 625 (2005).

[20] J. L. Herek, W. Wohlleben, R. J. Cogdell, D. Zeidler and M. Motzkus, *Quantum control of energy flow in light harvesting*, Nature **417**, 533 (2002).

[21] N. Makri, E. Sim, D. Makarov and M. Topaler, *Long-time quantum simulation of the primary charge separation in bacterial photosynthesis* Proc. Natl. Acad. Sci. USA **93**, 3926 (1996).

[22] J. B. Gilmore and R. H. McKenzie, *Criteria for quantum coherent transfer of excitations between chromophores in a polar solvent*, Chem. Phys. Lett. **421**, 266 (2006).

[23] G. S. Engel, T. R. Calhoun, E. L. Read, T.-K. Ahn, T. Mancal, Y.-C. Cheng, R. E. Blankenship and G. R. Fleming, *Evidence for wavelike energy transfer through quantum coherence in photosynthetic systems*, Nature **446**, 782 (2007).

[24] H. Lee, Y.-C. Cheng and G. R. Fleming, *Coherence dynamics in photosynthesis: Protein protection of excitonic coherence*, Science **316**, 1462 (2007).

[25] J. H. Reina, L. Quiroga and N. F. Johnson, *Quantum entanglement and information processing via excitons in optically-driven quantum dots* Phys. Rev. A **62**, 012305 (2000); J.H. Reina, L. Quiroga and N. F. Johnson, *NMR-based nanostructure switch for quantum logic*, Phys. Rev. B **62**, R2267 (2000); B. Lovett, J. H. Reina, A. Nazir and A. Briggs, *Optical schemes for quantum computation in quantum dot molecules*, Phys. Rev. B **68**, 205319 (2003).

[26] A. Ardavan, M. Austwick and S. C. Benjamin, *Nanoscale solid-state quantum computing*, Phil. Trans. R. Soc. London A **361**, 1473 (2003).

[27] J. H. Reina, L. Quiroga and N. F. Johnson, *Decoherence of quantum registers*, Phys. Rev. A **65**, 032326 (2002).

[28] D. Bruß, *Characterizing Entanglement*, J. Math. Phys. **43**, 4237 (2002).

[29] P. Shor, *Polynomial-Time Algorithms for Prime Factorization and Discrete Logarithms on a Quantum Computer*, SIAM J. Sci. Statist. Comput. **26**, 1484 (1997); see also `arXiv:quant-ph/9508027v2`.

[30] A. Peres, *Separability criterion for density matrices*, Phys. Rev. Lett. **77**, 1413 (1996).

[31] M. Horodecki, P. Horodecki and R. Horodecki, *Separability of mixed states: necessary and sufficient conditions* Phys. Lett. A **223**, 1 (1996).

[32] C. H. Bennett and D. P. DiVincenzo, *Quantum information and computation*, Nature **404**, 247 (2000).

[33] B. Bellomo, R. Lo Franco and G. Compagno, *Non-Markovian effects on the dynamics of entanglement*, Phys. Rev. Lett. **99**, 160502 (2007).

[34] T. Heinzel, *Mesoscopic Electronics in Solid State Nanostructures*, 2nd ed. (VCH-Wiley, Berlin, 2006).

[35] G. Cuniberti, G. Fagas, K. Richter (eds.), *Introducing Molecular Electronics*, Lecture Notes in Physics, (Springer, Heidelberg, 2005).

[36] M. Galperin, M.A. Ratner and A. Nitzan, *Molecular transport junctions: vibrational effects*, J. Phys. Cond. Matt. **19**, 103201 (2007).

[37] J. Reichert, R. Ochs, D. Beckmann, H. B. Weber, M. Mayor and H. v. Löhneysen, *Driving Current through Single Organic Molecules*, Phys. Rev. Lett. **88**, 176804 (2002).

[38] R. Smit, Y. Noat, C. Untiedt, N. D. Lang, M. C. van Hemert and J. M. Ruitenbeek, *Measurement of the conductance of a hydrogen molecule*, Nature **419**, 906 (2002).

[39] T. Böhler, J. Grebing, A. Mayer-Gindner, H. v. Löhneysen and E. Scheer, *Mechanically controllable break-junctions for use as electrodes for molecular electronics*, Nanotechnology **15**, S465 (2004).

[40] H. Park, J. Park, A.K.L. Kim, E.H. Anderson, A.P. Alivisatos and P.L. McEuen, *Nanomechanical oscillations in a single-C60 transistor*, Nature **407**, 57 (2000).

[41] J. König, J. Schmid, H. Schoeller and G. Schön, *Resonant tunneling through ultrasmall quantum dots: Zero-bias anomalies, magnetic-field dependence, and boson-assisted transport*, Phys. Rev. B **54**, 16820 (1996).

[42] Y. Meir and N.S. Wingreen, *Landauer formula for the current through an interacting electron region*, Phys. Rev. Lett. **68**, 2512 (1992).

[43] S. Hershfield, J.H. Davies and J.W. Wilkins, *Resonant tunneling through an Anderson impurity. I. Current in the symmetric model*, Phys. Rev. B **46**, 7046 (1992).

[44] D.A. Abanin and L.S. Levitov, *Fermi-Edge Resonance and Tunneling in Nonequilibrium Electron Gas*, Phys. Rev. Lett. **94**, 186803 (2005).

[45] A. Kaminski, Yu.V. Nazarov and L.I. Glazman, *Universality of the Kondo effect in a quantum dot out of equilibrium*, Phys. Rev. B **62**, 8154 (2000).

[46] A. Mitra and A.J. Millis, *Coulomb gas on the Keldysh contour: Anderson-Yuval-Hamann representation of the nonequilibrium two-level system*, Phys. Rev. B **76**, 085342 (2007).

[47] A. Oguri, *Fermi-liquid theory for the Anderson model out of equilibrium* , Phys. Rev. B **64**, 153305 (2001).

[48] A.A. Aligia, *Nonequilibrium magnetotransport through a quantum dot: An interpolative perturbative approach*, Phys. Rev. B **74**, 155125 (2006).

[49] R.M. Konik, H. Saleur and A. Ludwig, *Transport in quantum dots from the integrability of the Anderson model* Phys. Rev. B **66**, 125304 (2002).

[50] A. Rosch, J. Paaske, J. Kroha and P. Wölfle, *Nonequilibrium Transport through a Kondo Dot in a Magnetic Field: Perturbation Theory and Poor Man's Scaling*, Phys. Rev. Lett. **90**, 076804 (2003).

[51] T. Fujii and K. Ueda, *Perturbative approach to the nonequilibrium Kondo effect in a quantum dot*, Phys. Rev. B **68**, 155310 (2003); J. Phys. Soc. Jpn. **74**, 127 (2005).

[52] K.S. Thygesen and A. Rubio, *Conserving GW scheme for nonequilibrium quantum transport in molecular contacts*, Phys. Rev. B **77**, 115333 (2008).

[53] A. Komnik and A.O. Gogolin, *Resonant Tunneling between Luttinger Liquids: A Solvable Case*, Phys. Rev. Lett. **90**, 246403 (2003).

[54] B. Doyon and N. Andrei, *Universal aspects of nonequilibrium currents in a quantum dot*, Phys. Rev. B **73**, 245326 (2006).

[55] P. Mehta and N. Andrei, *Nonequilibrium Transport in Quantum Impurity Models: The Bethe Ansatz for Open Systems*, Phys. Rev. Lett. **96**, 216802 (2006).

[56] L. Borda, K. Vladar and A. Zawadowski, *Theory of a resonant level coupled to several conduction-electron channels in equilibrium and out of equilibrium*, Phys. Rev. B **75**, 125107 (2007).

[57] B. Doyon, *New Method for Studying Steady States in Quantum Impurity Problems: The Interacting Resonant Level Model*, Phys. Rev. Lett. **99**, 076806 (2007).

[58] E. Boulat and H. Saleur, *Exact low-temperature results for transport properties of the interacting resonant level model*, Phys. Rev. B **77**, 033409 (2008).

[59] A. Nishino and N. Hatano, *Resonance in an open quantum dot system with a Coulomb interaction: a Bethe-Ansatz approach* , J. Phys. Soc. Jap. **76**, 063002 (2007).

[60] H. Schoeller and J. König, *Real-Time Renormalization Group and Charge Fluctuations in Quantum Dots*, Phys. Rev. Lett. **84**, 3686 (2000).

[61] D. Bohr and P. Schmitteckert, *Strong enhancement of transport by interaction on contact links*, Phys. Rev. B **75**, 241103(R) (2007); P. Schmitteckert and F. Evers, *Exact Ground State Density-Functional Theory for Impurity Models Coupled to External Reservoirs and Transport Calculations*, Phys. Rev. Lett. **100**, 086401 (2008).

[62] A.J. Daley, C. Kollath, U. Schollwöck and G. Vidal, *Time-dependent density-matrix renormalization-group using adaptive effective Hilbert spaces* , J. Stat. Mech.: Theor. Exp. P04005 (2004).

[63] S.G. Jakobs, V. Meden and H. Schoeller, *Nonequilibrium Functional Renormalization Group for Interacting Quantum Systems*, Phys. Rev. Lett. **99**, 150603 (2007).

[64] T.A. Costi, *Renormalization-group approach to nonequilibrium Green functions in correlated impurity systems* , Phys. Rev. B **55**, 3003 (1997).

[65] Very recent progress on the application of the numerical renormalization group method out of equilibrium has been reported by F.B. Anders and A. Schiller, *Spin precession and real-time dynamics in the Kondo model: Time-dependent numerical renormalization-group study*, Phys. Rev. B **74**, 245113 (2006); F.B. Anders, *On steady-state currents through nano-devices: a scattering-states numerical renormalization group approach to open quantum systems*, Phys. Rev. Lett. **101**, 066804 (2008).

[66] A. Oguri, H. Ishii and T. Saso, *Kondo resonance in tunneling phenomena through a single quantum level*, Phys. Rev. B **51**, 4715 (1995).

[67] X. Wang, C.D. Spataru, M.S. Hybertsen and A.J. Millis, *Electronic correlation in nanoscale junctions: Comparison of the GW approximation to a numerically exact solution of the single-impurity Anderson model*, Phys. Rev. B **77**, 045119 (2008).

[68] C.H. Mak and R. Egger, *A multilevel blocking approach to the sign problem in real-time quantum Monte Carlo simulations*, J. Chem. Phys. **110**, 12 (1999); R. Egger, L. Mühlbacher and C.H. Mak, *Path-integral Monte Carlo simulations without the sign problem: Multilevel blocking approach for effective actions*, Phys. Rev. E **61**, 5961 (2000).

[69] L. Mühlbacher and R. Egger, *Crossover from nonadiabatic to adiabatic electron transfer reactions: Multilevel blocking Monte Carlo simulations*, J. Chem. Phys. **118**, 179 (2003).

[70] L. Mühlbacher and E. Rabani, *Real-time path integral approach to nonequilibrium many-body quantum systems*, Phys. Rev. Lett. **100**, 176403 (2008).

[71] T. L. Schmidt, P. Werner, L. Mühlbacher and A. Komnik, *Transient dynamics of the Anderson impurity model out of equilibrium*, Phys. Rev. B **78**, 235110 (2008).

[72] P. Werner, T. Oka and A. J. Millis, *Diagrammatic Monte Carlo simulation of non-equilibrium systems*, Phys. Rev. B **79**, 035320 (2009).

[73] M. Schirò and M. Fabrizio, *Real-time diagrammatic Monte Carlo for nonequilibrium quantum transport*, Phys. Rev. B **79**, 153302 (2009).

[74] S. Kehrein, *Scaling and Decoherence in the Nonequilibrium Kondo Model*, Phys. Rev. Lett. **95**, 056602 (2005).

[75] J.E. Han and R.J. Heary, *Imaginary-Time Formulation of Steady-State Nonequilibrium: Application to Strongly Correlated Transport*, Phys. Rev. Lett. **99**, 236808 (2007).

[76] P.W. Anderson, *Localized Magnetic States in Metals*, Phys. Rev. **124**, 41 (1961).

[77] H. Bruus and K. Flensberg, *Many-Body Quantum Theory in Condensed Matter Physics*, (Oxford UP, Oxford, 2004).

[78] A. M. Tsvelik and P. B. Wiegmann, *Exact results in the theory of magnetic alloys*, Adv. Phys. **32**, 453 (1983).

[79] A. Schiller and S. Hershfield, *Exactly solvable nonequilibrium Kondo problem*, Phys. Rev. B **51**, 12896 (1995).

[80] B. Horváth, B. Lazarovits, O. Sauret and G. Zaránd, *Failure of the mean-field approach in the out-of-equilibrium Anderson model*, Phys. Rev. B **77**, 113108 (2008).

[81] D. Giulini *et al.* (ed.), *Decoherence and the Appearance of a Classical World in Quantum Theory*, (Springer, Berlin, 1996).

[82] T. Dittrich, P. Hänggi, G.-L. Ingold, B. Kramer, G. Schön and W. Zwerger, *Quantum Transport and Dissipation*, (Wiley-VCH, Weinheim, 1998).

[83] A. J. Leggett, S. Chakravarty, A . T. Dorsey, M. P. A. Fisher, A. Garg and W. Zwerger, *Dynamics of the dissipative two-state system*, Rev. Mod. Phys. **59**, 1 (1987).

[84] L. E. Reichl, *The transition of Chaos: In Conservative Classical Systems: Quantum Manifestation*, Institute for Nonlinear Science, vol. 2, Springer (New York, 1992)

[85] F. Hund, *Zur Deutung der Molekelspektren*, Z. Physik **43**, 805 (1927).

[86] R. Feynman and F.L. Vernon, *The theory of a general quantum system interacting with a linear dissipative system*, Ann. Phys. (N.Y.) **24**, 118 (1963).

[87] J.W. Negele and H. Orland, *Quantum Many-Particle Systems* (Addison-Wesley, Redwood City, 1988).

[88] H. Grabert, P. Schramm and G.-L. Ingold, *Quantum Brownian motion: The functional integral approach*, Phys. Rep. **168**, 115 (1988); P. Schramm and H. Grabert, *Low-temperature and long-time anomalies of a damped quantum particle*, J. Stat. Phys. **49**, 767 (1987).

[89] A. Stern, Y. Aharonov and Y. Imry, *Phase uncertainty and loss of interference: A general picture*, Phys. Rev. A **41**, 3436 (1990).

[90] D. Loss and K. Mullen, *Dephasing by a dynamic asymmetric environment*, Phys. Rev. B **43**, 13252 (1991).

[91] M. Schlosshauer, *Decoherence and the quantum-to-classical transition*, (Springer, Berlin, 2007).

[92] J. Kondo, *Resistance Minimum in Dilute Magnetic Alloys*, Prog. Theor. Phys. **32**, 37 (1964).

[93] K. P. Schotte, *Tomonaga's model and the Kondo problem*, Z. Phys. A **230**, 99 (1970).

[94] S. Weiß, *Nonequilibrium quantum transport and confinement effects in interacting nanoscale conductors* (Shaker Verlag, Aachen, 2008); Universität Düsseldorf, Dissertation (2008).

[95] C. J. Wellard and L. C. L. Hollenberg, *Donor electron wave functions for phosphorus in silicon: Beyond effective-mass theory*, Phys. Rev. B **72**, 085202 (2005)

[96] J. C. Slater, *Quantum Theory of Molecules and Solids*, Vol. 1 (McGraw-Hill, New York, 1963).

[97] T. H. Ning and C. T. Sah, *Multivalley Effective-Mass Approximation for Donor States in Silicon. I. Shallow-Level Group-V Impurities*, Phys. Rev. B **4**, 3468 (1971).

[98] G. D. Mahan, *Many-particle physics*, (Plenum Press, New York, 1981).

[99] T. Brandes and B. Kramer, *Spontaneous Emission of Phonons by Coupled Quantum Dots* , Phys. Rev. Lett. **83**, 3021 (1999); T. Brandes and T. Vorrath, *Adiabatic transfer of electrons in coupled quantum dots* , Phys. Rev. B **66**, 075341 (2002).

[100] S. Vorojtsov, E. R. Mucciolo and H. U. Baranger, *Phonon decoherence of a double quantum dot charge qubit*, Phys. Rev. B **71**, 205322 (2005)

[101] MSM archive at http://www.ioffe.rssi.ru/SVA/NSM/

[102] M. Friedel, M. S. Hybertsen and M. Schlüter, *Local empirical pseudopotential approach to the optical properties of Si/Ge superlattices* Phys. Rev. B **39**, 7974 (1989)

[103] H. De Raedt, and B. De Raedt, *Applications of the generalized Trotter formula* , Phys. Rev. A **28**, 3575 (1983).

[104] M. Thorwart, *Tunneling and vibrational relaxation in driven multilevel systems*, (Shaker Verlag, Aachen, 2000); Universität Augsburg, Dissertation (2000).

[105] S. Weiss and R. Egger, *Path-integral Monte Carlo simulations for interacting few-electron quantum dots with spin-orbit coupling*, Phys. Rev. B **72**, 245301 (2005)

[106] D. P. DiVincenzo, *The Physical Implementation of Quantum Computation*, Fortschr. Phys. **48**, 771 (2000)

[107] J. H. Reina, L. Quiroga and N. F. Johnson, *Quantum entanglement and information processing via excitons in optically-driven quantum dots*, Phys. Rev. A **62**, 012305 (2000).

[108] J. Gilmore and R. McKenzie, *Quantum dynamics of electronic excitations in biomolecular chromophores: role of the protein environment and solvent*, J. Phys. Chem. A **112**, 2162 (2008).

[109] R. Egger and C. H. Mak, *Low-temperature dynamical simulation of spin-boson systems*, Phys. Rev. B **50**, 210 (1994).

[110] Y. Makhlin, G. Schön and A. Shnirman, *Quantum-state engineering with Josephson-junction devices*, Rev. Mod. Phys. **73**, 357 (2001).

[111] J. Gilmore and R. H. McKenzie, *Spin boson models for quantum decoherence of electronic exciations of biomolecules and quantum dots in asolvent*, J. Phys.: Cond. Matt. **17**, 1735 (2005).

[112] L. Onsager, *Electronic moments molecules in liquids*, J. Am. Chem. Soc. **58**, 1486 (1936).

[113] N. A. Nemkovich *et al.*, *Topics in Fluorescence Spectroscopy*, Vol. 2 (Plenum, New York, 1991).

[114] T. Simonson, *Macromolecular electrostatics: continuum model and their growing pains*, Curr. Opin. Struct. Biol. **73**, 357 (2001).

[115] S. Höfinger and T. Simonson, *Dielectric relaxation in proteins: a continuum electrostatics model incorporating dielectric heterogeneity of the protein and time-dependent charges*, J. Comput. Chem. **22**, 290 (2001).

[116] C. Bottcher, *Theory of Electric Polarization*, Vol. 1 (Elsevier, Amsterdam, 1973).

[117] G. Rickayzen, *Green's function in Condensed Matter*, (Academc, London, 1980).

[118] R. Kubo, *The fluctuation-dissipation theorem*, Rep. Prog. Phys. I **29**, 255 (1966).

[119] C. P. Hsu, H. Song and R. A. Marcus, *Time-dependent Stokes shift and its calculation from solvent dielectric dispersion data*, J. Chem. Phys. B **101**, 2546 (1997).

[120] X. Song and R. A. Marcus, *Quantum correction for electron transfer rates. Comparison of polarizable versus nonnonpolarizable description of solvent*, J, Chem. Phys. **99**, 7768 1993.

[121] L. Hartmann, I. Goychuk, M. Grifoni and P. Hänggi, *Driven tunneling dynamics: Bloch-Redfield theory versus path-integral approach*, Phys. Rev. E **61**, R4687 (2000).

[122] R. Egger, H. Grabert and U. Weiss, *Crossover from coherent to incoherent dynamics in damped quantum systems* ,Phys. Rev. E **55**, R3809 (1997).

[123] J. H. Shirley, *Solution of the Schrödinger Equation with a Hamiltonian Periodic in Time*, Phys. Rev. **138**, B979 (1965).

[124] M. Thorwart, L. Hartmann, I. Goychuk and P. Hänggi, *Controlling decoherence of a two-level atom in a lossy cavity*, J. Mod. Opt. **47**, 2905 (2000).

[125] R. Bulla, H.-J. Lee, N.-H. Tong and M. Vojta, *Numerical renormalization group for quantum impurities in a bosonic bath*, Phys. Rev. B **71**, 045122 (2005).

[126] R. Werner, *Quantum states with Einstein-Podolsky-Rosen correlations admitting a hidden-variable model*, Phys. Rev. A **40**, 4277 (1989).

[127] F. Verstraete, K. Audenaert, J. Dehaene and B. De Moor, *A comparison of the entanglement measures negativity and concurrence*, J. Phys. A: Math. Gen. **34**, 10327 (2001).

[128] M. Kroutvar, Y. Ducommun, D. Heiss, M. Bichler, D. Schuh, G. Abstreiter and J. Finley, *Optically programmable electron spin memory using semiconductor quantum dots* Nature **432**, 81 (2004).

[129] P. Rabl, D. DeMille, J. Doyle, M. Lukin, R. Schoelkopf and P. Zoller, *Hybrid quantum processors: Molecular ensembles as quantum memory for solid state circuits*, Phys. Rev. Lett. **97**, 033003 (2006).

[130] S. A. Crooker, J. A. Hollingsworth, S. Tretiak and V. I. Klimov, *Spectrally resolved dynamics of energy transfer in quantum-dot assemblies: Towards engineered energy flows in artificial materials* , Phys. Rev. Lett. **89**, 186802 (2002).

[131] J. H. Reina, R. G. Beausoleil, T. P. Spiller and W. J. Munro, *Radiative corrections and quantum gates in molecular systems*, Phys. Rev. Lett. **93**, 250501 (2004).

[132] K. Becker, J. M. Lupton, J. Müller, A. Rogach, D. V. Talapin, H. Weller and J. Feldmann *Electrical control of Förster energy transfer*, Nature Mater. **5**, 777 (2006).

[133] L.V. Keldysh, *Diagram technique for nonequilibrium processes*, Zh. Eksp. Teor. Fiz., **47**, 1515 (1964) [Sov. Phys. JETP **20**, 1018 (1961)].

[134] J. Schwinger, *Brownian Motion of a Quantum Oscillator*, J. Math. Phys. **2**, 407 (1961).

[135] J. Rammer and H. Smith, *Quantum field-theoretical methods in transport theory of metals* , Rev. Mod. Phys. **58**, 323 (1986).

[136] A. Kamenev, in *Nanophysics: Coherence and Transport*, Les Houches session LXXXI, ed. H. Bouchiat, Y. Gefen, S. Guéron, G. Montambaux, and J. Dalibard (Elsevier, New York, 2005).

[137] A. M. Rodero, *Field Theoretical Methods for Non-equilibrium Transport Phenomena*, Lecture notes Miraflores School on Dynamics of Interacting Electrons in Quantum Wires (2003).

[138] J.E. Hirsch and R.M. Fye, *Monte Carlo Method for Magnetic Impurities in Metals*, Phys. Rev. Lett. **56**, 2521 (1986).

[139] J.E. Hirsch, *Discrete Hubbard-Stratonovich transformation for fermion lattice models*, Phys. Rev. B **28**, 4059 (1983).

[140] J. Hubbard, *Calculation of Partition Functions* , Phys. Rev. Lett. **3**, 77 (1959).

[141] F. Siano and R. Egger, *Josephson Current through a Nanoscale Magnetic Quantum Dot* , Phys. Rev. Lett. **93**, 047002 (2004).

[142] A. Rosch, J. Paaske, J. Kroha and P. Wölfle, *The Kondo effect in non-equilibrium quantum dots: Perturbative renormalization group* J. Phys. Soc. Jap. **74**, 118 (2005).

[143] L. Dell'Anna, A. Zazunov and R. Egger, *Superconducting nonequilibrium transport through a weakly interacting quantum dot*, Phys. Rev. B **77**, 104525 (2008).

[144] T.A. Costi, A.C. Hewson and V. Zlatic, *Transport coefficients of the Anderson model via the numerical renormalization group*, J. Phys.: Condens. Matter **6**, 2519 (1994).

[145] D.R. Hamann, *New Solution for Exchange Scattering in Dilute Alloys*, Phys. Rev. **158**, 570 (1967).

Danksagung/Acknowledgement

Auf diesem Weg möchte ich allen danken, die am Gelingen dieser Arbeit beteiligt waren.
Bei PD Dr. Michael Thorwart bedanke ich mich für die intensive Betreuung und sorgfältige Durchsicht dieser Arbeit. In vielen spannenden Diskussionen konnte ich viel über die zugrundeliegende Physik und die damit verbundenen Methoden lernen. Dies hat sowohl mein physikalisches Verständnis als auch meine persönlichen Erfahrungen enorm erweitert.
Herrn Prof. Dr. Egger danke ich für die hervorragenden Arbeitsbedingungen an seinem Institut und interessante physikalische Diskussionen sowie die Koreferenz dieser Arbeit.
Besonders danken möchte ich auch Stephan Weiß mit dem ich über zwei Jahre ein Büro geteilt habe und mit dem ich in vielen langen Diskussionen (nicht nur im Büro) zusammengearbeitet habe. Auch diese Arbeit ist zu einem nicht unwesentlichen Teil Ergebnis dieser Diskussionen.
Mein Dank gilt auch allen jetzigen und ehemaligen Mitarbeitern des Instituts für Theoretische Physik IV, Ahmad Omairat, Alessandro De Martino, Alex Zazunov, Andreas Schulz, Astrid Schattka, Christophe Mora, Luca Dell'Anna, Philip Ingenhoven, Roland Hützen, Vittorio Peano Cavasola, Wolfgang Häusler, Zelimir Marojevic und Frau Wildhagen, die bei allen administrativen Fragen immer sehr geholfen hat. Weiterhin danke ich den Administratoren des Institutsclusters Jens Bremer und Helmut Wenz sowie Stephan Raub vom ZIM für den reibungslosen Ablauf der vielen intensiven Rechnungen zu dieser Arbeit.
Allen Kollegen und Freunden mit denen ich in dieser Zeit musiziert habe möchte ich ebenfalls danken, da die immer ein höchstwillkommener und unverzichtbarer Ausgleich zur täglichen Arbeit war und ist.
Bei meiner Familie und meiner Freundin Kathi bedanke ich mich für die immerwährende Unterstützung während dieser Zeit.
Last but not least I want to thank Prof. John Henry Reina for the kind and warm welcome he gave me during my stay at the Universidad di Valle in Cali, Columbia. Parts of this these are the results of the enthusiastic discussion we had during my visit.

Erklärung

Die hier vorliegende Dissertationsschrift habe ich eigenständig und ohne unerlaubte Hilfe angefertigt. In der vorgelegten oder ähnlichen Form wurde diese Arbeit bei keiner anderen Institution eingereicht und ich habe keine erfolglosen Promotionsversuche unternommen.

Düsseldorf, 2. Juni 2009